Nucleation and Growth of Faujasite Zeolite Nanostructures

A Dissertation
SUBMITTED TO THE FACULTY OF THE
UNIVERSITY OF MINNESOTA
BY

Maryam Tariq Khaleel

IN PARTIAL FULFILLMENT OF THE REQUIREMENTS
FOR THE DEGREE OF
DOCTOR OF PHILOSOPHY

Professor Michael Tsapatsis, adviser

December 2015

Acknowledgements

I would like to extend my sincere appreciation to my adviser, Professor Michael Tsapatsis, for his continuous guidance and support throughout my graduate studies, and most importantly, for giving me the opportunity to work in his research group. His supervision helped me overcome challenging problems and succeed in the research projects. I would also like to thank the Tsapatsis group members for their help during my time in the lab. Special thanks go to Xueyi Zhang for helping me start my experimental work when I first joined the group. I am also very grateful to my preliminary and final examination committee members, Professors K. Andre Mkhoyan, Prodromos Daoutidis, Wayne Gladfelter and specially Professors Alon V. McCormick and Andreas Stein for their efforts in reviewing this dissertation. I would also like to thank all teachers who instructed me in undergraduate and graduate courses at the Petroleum Institute (Abu Dhabi, UAE) and the University of Minnesota, respectively. The knowledge that they helped me gain during my studies became an essential component in the fulfillment of this work. I also appreciate the useful discussions with the University of Minnesota Characterization Facility staff including Wei Zhang, Nick Seaton, Jason Myers and Fang Zhou. Finally, I want to express my gratitude to ADNOC (Abu Dhabi National Oil Company) for their scholarship and most importantly, to my family for their continuous and unconditional support throughout my graduate career.

Dedication

This dissertation is dedicated to my parents.

Abstract

Zeolites are porous materials with 3-dimensional crystalline frameworks made of silicon and aluminum atoms linked through oxygen atoms. Zeolite frameworks have cages or channels of molecular dimensions that give them superior properties in separation, adsorption, ion exchange, and catalytic applications. However, diffusion limitations of bulky molecules in the zeolite pores can lead to a reduction in activity, selectivity and catalyst lifetime. This can be alleviated by modifying the zeolite crystal morphology or size (reducing the diffusion path length) or by introducing larger pores to improve diffusion (hierarchical zeolites). However, most of the procedures reported to create hierarchical zeolites are not well understood, and so in many cases, the properties cannot be precisely controlled. Moreover, they mostly utilize expensive and unsafe additives and so cannot be commercialized.

This dissertation focuses on developing a better understanding of the growth of hierarchical Faujasite zeolite morphologies (one of the most widely used zeolites in industry). This may allow the design and engineering of hierarchical zeolites from inorganic routes. In chapter 2, a structural study using transmission electron microscopy imaging and diffraction of house-of-card-like nanosheet assembly of Faujasite sheets was undertaken, and it was demonstrated that there is a direct link between polytypism and the repetitive branching mechanism leading to hierarchical structures. In chapter 3, the effects of synthesis conditions on the FAU/EMT content and the size of nanocrystals, formed from inorganic aluminosilicate sols, were investigated using high resolution transmission electron microscopy imaging and comparison of experimental X-ray diffraction patterns with simulations. Findings demonstrated that it is possible to combine the effects of pre- and post-nucleation sol composition to steer crystal size and crystal structure, respectively. With a better understanding of the evolution of sol structure and the nucleation of zeolites at the early stages, it may be possible to control particle size and shape, and the intergrowth of zeolite polymorphs in crystals. In chapter 4, further insight was acquired by cryogenic transmission electron microscopy and small angle X-ray scattering studies on representative precursor sols (aged and crystallized at ambient

temperature). Results confirmed precursor nanoparticle evolution and aggregation, and emphasized the importance of solution phase composition at both pre- and post-nucleation stages of aggregative crystal growth.

Table of Contents

List of Tables

List of Figures

Chapter 1

Introduction: Diffusion Limitations in Zeolites

1.1 Zeolites

Porous solids are of technological interest because of their ability to interact with atoms, ions and molecules throughout the bulk of the material giving them many applications in industry, environmental protection, and medicine.[1] Traditionally, porous solids in catalysis and adsorption included alumina, silica, and activated carbon that have disordered pore structure. When making porous solids, the aim is to control the size, shape, and connectivity of the voids and channels built into solid frameworks with the objective of increasing the surface area per gram solid. The field of porous materials was revolutionized with the discovery of synthetic zeolites in the 1950s (zeolites also exist naturally as minerals). Zeolites[2] are crystalline aluminosilicates where silicon and aluminum atoms are linked through oxygen atoms in three dimensional open framework structures that have higher thermal and mechanical stabilities compared to other ordered porous solids like aluminophosphates[3] and metal–organic frameworks.[4] Zeolite frameworks have cages (Fig. 1-1a) or channels (Fig. 1-1b) of molecular dimensions (cages ~ 1.3 nm and channels ~ 0.8 nm) inside which cations, water or other small molecules reside. According to IUPAC (International Union of Pure and Applied Chemistry) classification, pores < 2 nm are called micropores, between 2 nm and 50 nm are called mesopores and > 50 nm are called macropores.

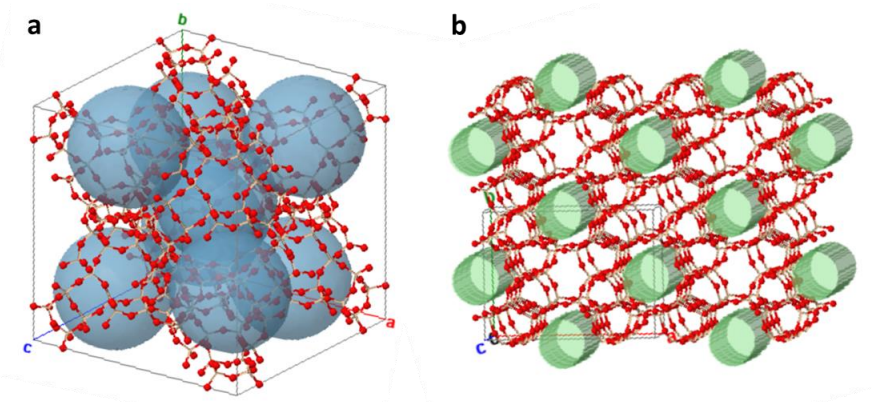

Figure 1-1: Zeolite framework structures (generated by ZEOMICS[5]) highlighting the a) cages in FAU framework and b) channels in FER framework (zeolites are given 3 letter framework codes by the Structure Commission of the International Zeolite Association[6]).

The ordered structures with molecular dimensions of the zeolite frameworks give them unique high surface area and molecular shape and size selectivity (i.e., they can separate molecules on the basis of their size by selectively adsorbing small molecules from a mixture containing molecules too large to enter their pores). An example is the isomerization of m-xylene to p-xylene in the petrochemical industry where the MFI zeolite framework allows p-xylene (kinetic diameter ~0.58 nm) to diffuse through but excludes o- and m-xylene (kinetic diameter ~0.68 nm).

A net unit negative charge is associated with each Al replacing Si in zeolite framework. This charge is counterbalanced by an inorganic or organic cation that can be ion-exchanged. The atoms constituting the framework and cations residing within the pores and channels determine the acidic properties of a zeolite.[7]

These properties allow zeolites to find applications in separation,[8–10] adsorption,[11] ion exchange,[12,13] and heterogeneous catalysis (including in the petroleum and petrochemical industries).[14–16] Several emerging applications of zeolites include chemical sensing,[17–19] optoelectronics,[20] and medicine.[21–25] A lot of progress has been made in the synthesis of new zeolite structures and today, 229 different frameworks have been reported.[26] The interest in zeolites stems from the ability to manipulate their bulk properties through variations in the atomic structure.

1. 2 Limitations of Microporous Zeolites

Activated diffusion mechanism in micropores[27] is slow but beneficial for applications requiring the shape selectivity of zeolites e.g. isomerization of m-xylene to p-xylene. In this case, operation under strongly diffusion limited conditions (large zeolite crystals with long diffusion path lengths and low acidity at the external surface) is beneficial in order to enhance the fraction of p-xylene in the isomer distribution.[28] However, there are cases when microporosity, which gives zeolites their powerful and unique features, can be a bottle neck limiting the catalytic performance of zeolites in applications involving bulky molecules due to restricted access to active sites and low intracrystalline diffusion coefficients.[29,30] This lowers the rate of processes[27] and results in low catalyst utilization.

The degree of catalyst utilization can be quantified by the effectiveness factor (η) and the relative reaction and diffusion rates can be described by the Thiele modulus (Φ). These two dimensionless numbers can be defined as follows for steady-state diffusion and reaction, slab model, first-order irreversible reaction, and isothermal conditions,

$$\eta = \frac{\text{rate of reaction observed}}{\text{intrinsic reaction rate}} = \frac{\tanh \Phi}{\Phi}$$

$$\Phi = \frac{\text{reaction rate}}{\text{diffusion rate}} = \sqrt{\frac{kL^2}{D}}$$

For applicability of classical definitions of Thiele modulus and effectiveness factor for zeolites refer to the work by Baur and Krishna.[31]

For applications that are limited by diffusion (large values of Φ and low η), a small outer volume of the catalyst is utilized as the reactants cannot reach the interior volume before reacting (Fig. 1-2). Full utilization of the catalyst particle ($\eta \rightarrow 1$) happens in the absence of diffusion constraints (observed reaction rate equals the intrinsic reaction rate). In this case, the reactant concentration is uniform in the catalyst. Zeolite under-utilization is a major drawback in industrial reactions hindered by diffusion limitations, as it impacts not

only the activity, but also the selectivity (generated molecules that are relatively large will have a limited diffusivity to reach the end of the pores and might get converted to smaller products) and stability of the catalyst (catalyst deactivation by pore blockage due to large molecules or coke formation).[32,33]

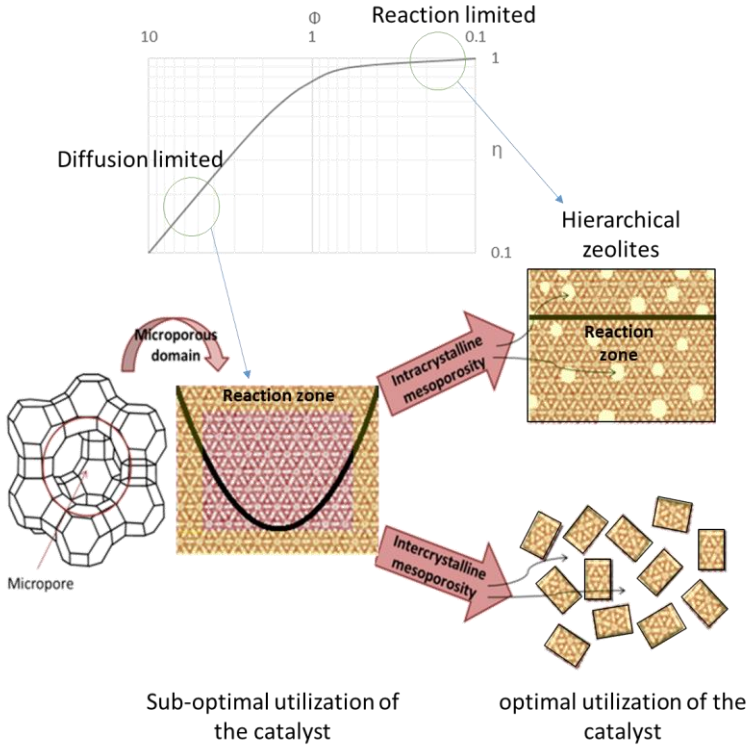

Figure 1-2: Plot showing the dependence of the effectiveness factor (η) on Thiele modulus (Φ). Regions in the plot are marked showing where microporous only zeolites suffering from diffusion limitations operate and where hierarchical zeolites with improved transport operate. The black traces in the zeolite crystal representations correspond to the reactant concentration profiles across the crystals.

1. 3 Synthesis of Hierarchical Zeolites

Ordered mesoporous aluminosilicates, with pore size between 2 and 50 nm, alleviate diffusion limitations of large molecules.[34–36] However, their amorphous structure results in low hydrothermal stability and low acidity, making these materials inferior to zeolites and limiting their practical application. For these reasons, research focused on developing ways to better utilize the zeolite micropore volume. To enhance diffusion at given operation conditions, the internal pore architecture of the catalyst needs to be changed (synthesize zeolites with larger micropores or insert larger mesopores into

the zeolite particles) or the crystal size or morphology (hence the diffusion path length) needs to be manipulated (Fig. 1-2). Smaller zeolite crystals also have the added advantage of higher surface area for bulky reactants that cannot enter the micropores and the formation of inter-crystalline mesoporosity resulting from the packing of the crystals. This approach is discussed in chapter 3 of this dissertation. It has already been discussed that creating extra-large micropores (1– 2 nm) does not help much.[29,30] These materials require using complex organic compounds as structure directing agents and germanium as framework atoms (high production cost), and suffer from low thermal and hydrothermal stability and low acidity.[1,37]

Lots of interest has been devoted to the development of zeolites that combine zeolitic micropores with meso- and/or macropores in interconnected network; hierarchical zeolites.[1,29,30,38–41] The mesopores ensure optimal accessibility and transport of reactants and products between the zeolite crystal surface and microporous volume while micropores provide the active sites. The area of hierarchical zeolite catalysts have been revolutionized by the great number of synthesis strategies that are developed for tailoring the pore architecture and these include direct hydrothermal synthesis ('bottom-up') methods, demetallation ('top-down') methods and a combination of both. Interest in hierarchical zeolites stems from the higher reaction rates,[42–45] improved selectivity,[44,46,47] resistance to deactivation,[46–49] and novel adsorption behavior[50] that they exhibit in comparison to the typical zeolites that have only micropores. Some of the reactions in which hierarchical zeolites have attained superior performance include alkylation, isomerization, and (hydro)cracking.[14,30,38,51,52]

1.3.1 Bottom-up Methods

Bottom-up methods are categorized into hard templating, soft templating and indirect templating routes (without using a mesopore template). The templates are encapsulated in the zeolite during the synthesis and removed afterwards by calcination to give rise to mesoporosity. Solid materials used as hard templates are mostly carbonaceous materials due to their chemical inertness, structural diversity and ease of

removal by combustion. These include carbon nanoparticles,[53,54] nanotubes,[55] nanofibers,[56] aerogels,[57,58] and ordered mesoporous carbons (resulting in ordered mesoporous zeolites).[59,60] Soft templating routes employ relatively flexible species such as surfactants and polymers acting as mesopore templates. The mesopore size can be controlled by changing the length of the surfactant or polymer that is used.

Fabricating hierarchical zeolites using mixtures of surfactants and zeolite micropore templates proved difficult as a result of the phase-segregation of zeolite crystals and mesoporous materials with amorphous pore walls.[61] This can be overcome by using templates such as organosilanes, silylane cationic polymers,[62] dual function polyquaternary ammonium surfactants,[49,63–65] and dual-function cationic polymers.[66] The presence of silanol groups in the template strengthens the interaction with the zeolite phase through the formation of covalent bonds. Dual-function polyquaternary ammonium surfactants can be used to simultaneously generate micropores and mesopores in hierarchical zeolites. The surfactant can be tailored by changing the number of ammonium groups, the length and structure of the linkage and the hydrophobic tails, leading to different meso- and microporous structures. Bolaform amphiphilic templates with bi-quaternary ammonium head groups and biphenyl groups were used to make house-of-card-like MFI nanosheet assembly that retains its structure and mesoporosity after calcination.[63] 3-(trimethoxysilyl) propyl hexadecyl dimethyl ammonium chloride (TPHAC) is an amphiphilic organosilane that was used to create mesoporosity in one-step synthesis for zeolites ZSM-5,[67] LTA,[68] SOD,[69] and Faujasite.[70] In contrast to the relatively compact morphology, with mesopores located inside the crystals, adopted by ZSM-5,[67] LTA,[68] and SOD,[69] hierarchical Faujasite developed house-of-card-like nanosheet assembly.[70] The drawback to mesopore templating methods is the utilization of expensive organic additives that need to be removed to open the mesopore network. Since the synthesis of conventional Faujasite does not require any organic templates, it is highly desirable to find a route to achieve this hierarchical assembly of Faujasite sheets without any organic additives. With a better understanding of the mechanism of branching, the design and engineering of a similar inorganic material, with control over

mesopore size, may become possible. Chapter 2 of this dissertation presents a transmission electron microscopy structural study of this material and a conceptual model for branching.

Hierarchical zeolites were also synthesized in the absence of organic additives by the intergrowth of zeolite crystallites. Reported synthesis routes include steam-assisted crystallization (mesoporous aggregate structure assembled from crystalline domains),[71] solid-phase crystallization (amorphous meso-macroporous gel crystallized while retaining its preformed macroporous structure),[72] nano-fusion (nanozeolite gel containing dissolved aluminosilicate species is dried leading to fusion into stable hierarchical zeolite aggregates),[73] and repetitive branching by rotational intergrowth.[43,70,74–76] These strategies require only zeolite micropore structure directing agents (if needed for the particular framework). Repetitive branching holds promise for industrial implementation due to its simplicity (one-step synthesis) and lower cost (simple structure-directing agents or additives) compared to hard and soft templating approaches.

1.3.2 Top-down Methods

Top-down methods include post synthetic dealumination and desilication, by which mesoporosity is created by the selective removal of framework aluminium or silicon atoms from pre-synthesized zeolite crystals. Meso/macro pores were first introduced into zeolite Y in the process of stabilizing it by increasing Si/Al ratio by steaming (hydrothermal treatment at temperatures above 500 °C) and subsequent acid leaching to extract framework Al and form ‘ultrastable’ Y (USY).[38,52,77–79] A mild acid treatment is needed to remove the amorphous debris formed after steaming that can block the meso- and micropores. Dealumination can also be performed by using concentrated acid solutions and by treatment with ammonium hexafluorosilicate, or silicon tetrachloride. Desilication involves treating zeolite crystals with base solution to selectively extract Si from the framework. Hierarchical USY zeolite can also be prepared by desilication.[80–82]

Depending on the zeolite framework Si/Al ratio, different post-synthetic treatments can be employed to effectively create meso-pore surfaces up to 500 m^2 g^{-1} and retain crystallinity. Mesopore formation by desilication is optimal when the zeolite Si/Al ratio is not too high, so as to preserve the intrinsic zeolite crystallinity, and not too low, so as not to render desilication ineffective in extracting framework silicon.[83,84] For instance, zeolite Y (Si/Al around 2.5) is almost inert to desilication by base leaching and so a mild dealumination is usually employed first to increase Si/Al to 4 or higher to facilitate subsequent efficient desilication. Moreover, Al-rich debris after treatment can be removed by a subsequent mild acid wash. On the other hand, Si-rich USY zeolites (Si/Al around 15) is extremely sensitive to alkaline treatment and using inorganic (such as $Al(OH)_4^-$ and $Ga(OH)_4^-$) or organic (such as tetrapropyl ammonium and tetrabutyl ammonium) additives during alkaline treatment is needed to protect the zeolite structures upon the introduction of mesoporosity preserving crystallinity and microporosity.[81,85] This allows desilication to be extended to high Si/Al zeolites. It is believed that the interaction of these additives with the zeolite surface provides protection against dissolution.[86] Partial de-templation followed by desilication can also be used to control the introduction of mesoporosity into zeolites that are synthesized using structure directing agents.[87] Secondary porosity in Al-rich zeolite X (Si/Al ≈ 1) cannot be generated by typical de-alumination procedures without invoking major structural loss. Recently this challenge was overcome by using weak acid to treat the ammonium form of zeolite X (NH_4X) creating meso-porosity while preserving the crystallinity and micropore volume for about 70%. This is due to the relatively higher reactivity of NH_4X compared to NaX in aqueous acid or base treatments.

Top-down strategies are the most widely employed techniques to introduce meso/macro-porosity for hierarchical zeolite Y and USY. This is the case because highly siliceous Faujasite cannot be directly hydrothermally synthesized. Though de-alumination and de-silication are affordable and scalable, there are several drawbacks associated with them and these include significant changes in framework acidity, deposition of amorphous material inside the pores, inability to precisely control the size of the secondary porosity,

and the local destruction of crystal structure (secondary porosity results from these defected regions). Ideally, the zeolite crystallinity and microporous volume should not be significantly compromised. Moreover, diffusion[88] and microscopy[89] studies showed that a large part of the secondary porosity generated by framework post-synthetic de-metallation can form isolated cavities in the crystals and therefore do not significantly contribute to improving access to the microporous volume. Only under special treatment conditions are the mesopores exclusively cylindrical, interconnected and accessible from the outside of the crystals.[89]

Zeolite recrystallization can also be used to introduce mesoporosity into zeolite crystals with the aid of surfactants during base leaching. Two types of mesopores are formed, those attributed to surfactant-induced micelle formation involving dissolved species and others resulting from the desilication process.[90] This process allows almost complete recovery of the zeolite material. The use of cetyltrimethylammonium bromide (CTABr) with the acid or base treatments was reported for USY to facilitate the reassembly of dissolved species during alkaline treatment.[85]

1. 4 Thesis Organization

Of the many hierarchical zeolites developed, a very important zeolite for industrial applications is hierarchical FAU which is classified as zeolite X or Y depending on the framework Si/Al ratio (Si/Al =1-1.5 for zeolite X and Si/Al > 1.5 for zeolite Y).[91] Zeolite X is used as ion exchanger, molecular sieve, and adsorbent (because of its large cation-exchange capacity) and zeolite Y is used as catalyst in petrochemical applications (such as (hydro)cracking) and biomass-related catalytic processes.[52] The work presented in this dissertation is focused on synthesizing and characterizing hierarchical Faujasite zeolites. Computational methods including electron diffraction, high resolution transmission electron microscopy image, and X-ray diffraction pattern simulations are used to understand the structures of the materials studied.

Economic, safety and environmental issues have thus far prevented the industrial implementation of bottom-up strategies for introducing mesoporosity into zeolites because of the organic additives that are used. The synthesis of house-of-card-like nanosheet assembly of Faujasite sheets reported by Inayat et al.[70] uses organic additives, whereas the synthesis of conventional Faujasite does not require any additives. It is therefore highly desirable to find a route to achieve this hierarchical assembly of Faujasite sheets without any organic additives. With a better understanding of the mechanism of branching, the design and engineering of a similar inorganic material, with control over mesopore size, may become possible. Chapter 2 of this dissertation presents a transmission electron microscopy structural study of house-of-card-like nanosheet assembly of Faujasite sheets reported by Inayat et al.[70] Accordingly, a conceptual model for branching is proposed, demonstrating a direct link between polytypism and the repetitive branching mechanism leading to hierarchical structures. A brief overview of the Faujasite structure, addressing faulting and intergrowth of FAU and EMT frameworks, which is needed for understanding the results, is given in chapter 2.

Another approach to creating hierarchical Faujasite is the synthesis of nano-sized crystals. The intergrowth of FAU and EMT in nano-crystals will affect their bulk properties because FAU and EMT frameworks have different pore connectivity. In a recent study, FAU/EMT materials performed better than pure FAU and pure EMT materials (synthesized using crown ether) in Fluid Catalytic Cracking gasoline hydro-upgrading where they exhibited a good balance between hydrodesurfurization efficiency and Octane Number preservation.[92] This implies that control of FAU/EMT content in conjunction with controlling particle size and shape is desirable. i) The effect of synthesis conditions of inorganic aluminosilicate sols on the intergrowth of FAU and EMT in nano-crystals, on crystal size, and on crystal interpenetration in particles, and ii) the synthesis of high content FAU nano-crystals from inorganic aluminosilicate sols by combining pre- and post-nucleation trajectories, are presented in chapter 3.

Understanding the events in the early stages of zeolite nucleation is important in determining the course of the subsequent crystallization, possibly allowing structural and

morphological control of zeolite crystals. However, very little is understood about this complex process due to the challenges involved in available sample preparation and characterization techniques. To get insight into the evolution of the precursor sols used in the synthesis of Faujasite nano-crystals, cryogenic transmission electron microscopy and small angle X-ray scattering studies were employed (chapter 4). Results confirmed precursor nanoparticle evolution and aggregation before nucleation, and emphasized the importance of solution phase composition at both pre- and post-nucleation stages of aggregative crystal growth. Concluding remarks are given at the end of the dissertation.

Chapter 2

On the Rotational Intergrowth of Hierarchical FAU/EMT Zeolites*

2.1 Introduction

2.1.1 Background

The application of zeolites as base catalysts in the manufacturing of fine chemicals involves the transformation of large molecules, such as fatty acids or sugars. Such applications would benefit from the improved transport in hierarchical zeolites, yet there are only a few reports on the application of hierarchical zeolites in base catalysis.[69,82] This is because limited basic strength is attainable by ion exchange,[93,94] and stronger basicity requires using more elaborate treatments, such as the deposition of intrazeolitic metal clusters[95] or oxides,[96] or high temperature treatment of acidic zeolites in gaseous NH_3 (nitridation).[97]

Zeolite X (Si/Al ≈ 1) is highly hydrophilic and is an important basic catalyst,[98] for example for transesterification reactions.[99] Secondary porosity in Al-rich zeolite X cannot be generated by typical de-alumination procedures without invoking major structural loss. Moreover, desilication is not effective for high Al content zeolites. Recently this challenge was overcome both by post synthetic treatment and templating. In post synthetic treatment, a weak acid can be used to treat the ammonium form of zeolite X (NH_4X) creating meso-porosity while preserving the crystallinity and micropore volume for about 70%.[82] This is due to the relatively higher reactivity of NH_4X compared to NaX in aqueous acid or base treatments. Given the drawbacks of top-down strategies for creating meso/macroporosity in zeolites, which include significant changes in framework acidity, deposition of amorphous material inside the pores, inability to precisely control the size of the secondary porosity, the local destruction of crystal structure, and the formation of isolated cavities in the crystals that cannot contribute to

---

*Results presented in this chapter are published in: Khaleel, M.; Wagner, A. J.; Mkhoyan, K. A.; Tsapatsis, M. *Angew. Chem. Int. Ed. Engl.* **2014**, *53* (36), 9456–9461 (© 2014 John Wiley and Sons Inc.)

improving access to the microporous volume,[88,89] it is highly desirable to be able to generate and tune mesopores during synthesis. Such reports for creating meso-porosity in FAU include the usage of hard[57,60] or soft[70] expensive organic additives that need to be thermally removed after the synthesis to open up the mesopore network. Economic, safety and environmental issues have thus far prevented the industrial implementation of these bottom-up strategies.

Hierarchical zeolite X grown as house-of-card-like assembly of Faujasite nanosheets have been reported by Inayat et al.[70] This material has three-fold hierarchical pore system combining the 0.74 nm FAU micropores with 7 nm mesopores within the sheets (sheet thickness of ~100–200 nm) and macroporous (ca. 200 nm) resulting from the voids between the sheets.[70] However, a plausible scenario for the process of branching was not presented so far. The reported hydrothermal synthesis uses 3-(trimethoxysilyl)propyl hexadecyl dimethyl ammonium chloride (TPHAC) as an additive.[70] Since the synthesis of conventional Faujasite does not require any additives, it is highly desirable to find an inorganic route to achieve this hierarchical assembly of Faujasite sheets. With a better understanding of the branching mechanism, the design and engineering of a similar inorganic material, with control over nanosheet thickness, branching frequency, and other structural characteristics, may become possible. The work presented in this chapter involves a structural study (using transmission electron microscopy imaging and diffraction) of the house-of-card-like nanosheet assembly of Faujasite sheets. Evidence is provided by comparison to simulations that this material is an intergrowth of FAU and EMT and a conceptual model is presented for the growth of the FAU material with a small fraction of EMT in an atypical morphology of assembled sheets with well-defined intersection angles of 70.5°. The small amount of EMT plays a crucial role in directing the growth of house-of-card Faujasite demonstrating that there is a direct link between polytypism and the repetitive branching mechanism leading to hierarchical structures. A brief overview of the Faujasite structure, addressing faulting and intergrowth of FAU and EMT frameworks, which is needed for understanding the results, is given.

2.1.2 FAU and EMT Frameworks

The 'Faujasite sheet' consists of cuboctahedra (at the 24 vertices of which there are either SiO_4 or $A1O_4^-$ tetrahedra) linked via hexagonal prisms (double six rings).[91] This Periodic Building Unit is common to two zeolite frameworks, FAU (corresponding to the (111) layer that stacks in ABCABC sequence) and EMT (corresponding to the (001) layer that stacks in ABAB sequence). Fig. 2-1a shows the $[111]_{FAU}$ /$[001]_{EMT}$ views of a 'Faujasite sheet'. FAU belongs to space group $Fd\bar{3}m$ and has a cubic crystal structure with unit cell parameters a=24.7 Å and α=90°.[91] Fig. 2-1b shows the inversion symmetry between Faujasite sheets along $[111]_{FAU}$ in the FAU framework resulting in a 'sheet of FAU cages'.[100] The FAU framework consists of an array of 'supercages,' each with a free diameter of ca. 13 Å (marked by blue spheres in Fig. 1-1a), separated by 12-membered ring apertures with a diameter of 7.4 Å. EMT belongs to space group $P6_3/mmc$ and has a hexagonal crystal structure with unit cell parameters a=17.4 Å, c=28.3 Å, α=90° and γ=120°.[101] Fig. 2-1c shows the mirror symmetry between Faujasite sheets along $[001]_{EMT}$ in the EMT framework resulting in a "sheet of EMT cages".[100] The EMT framework has a tunnel structure with a diameter varying between 7.4 and 13 Å. Intersecting these tunnels which run along $[001]_{EMT}$ are elliptical apertures with dimensions of 6.9 and 7.4 Å.

As FAU and EMT are constructed from the same building unit, they can exist in the same material (FAU/EMT intergrowth) with the FAU and EMT components either segregated non-randomly into contiguous blocks or intimately intergrown together.[100] Segregation acts to reduce both the configurational entropy associated with stacking statistics and the elastic energy associated with coherency strain.[100] Moreover, faults (disruption of ABCABC sequence in FAU or ABAB sequence in EMT) can occur. The stacking of Faujasite sheets can be observed by High Resolution Transmission Electron microscopy (HRTEM) of crystals oriented along $[1\bar{1}0]_{FAU}$ (or $[100]_{EMT}$). Throughout this dissertation, we will refer to samples that contain both FAU and EMT as 'Faujasite' samples.

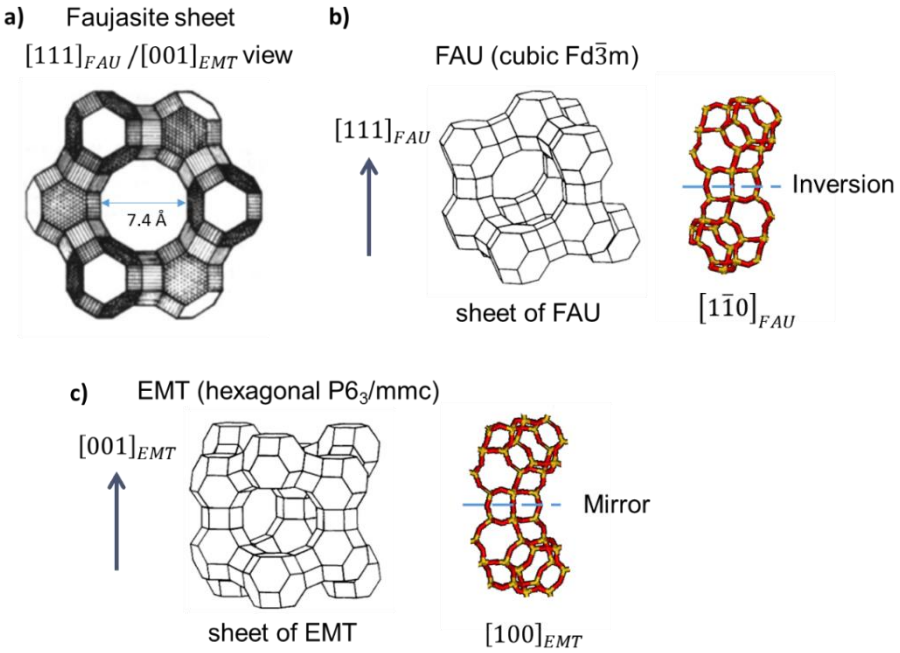

Figure 2-1: a) $[111]_{FAU}$ /$[001]_{EMT}$ views of a 'Faujasite sheet'. b) 'Sheet of FAU cages' resulting from inversion symmetry between Faujasite sheets along $[111]_{FAU}$ in the FAU framework and c) 'sheet of EMT cages' resulting from mirror symmetry between Faujasite sheets along $[001]_{EMT}$ in the EMT framework.

The common crystal habit for FAU is octahedral. Anisotropic sheet morphology has been reported for EMT and FAU/EMT intergrowth materials. Most FAU/EMT intergrowth materials reported in literature grow as anisotropic plates and in some cases, including ZSM-20 and ZSM-2, the plates interpenetrate at ~ 70°.[102]

FAU can be synthesized from aluminosilicate gel containing only Na^+ ions or with the addition of 15-crown-5.[101] EMT can be synthesized by adding 18-crown-6 to the aluminosilicate gel.[101] It was proposed that 18-crown-6 acts as a structure-directing agent and is located within the oblate cages of EMT on a growing Faujasite sheet forcing the following Faujasite sheet to grow with a mirror symmetry relative to the growing sheet resulting in EMT sheet.[103] This mechanism views the crystallization in terms of a layer growth which is supported by HRTEM of surface growth steps and by atomic force microscopy.[104] The syntheses of FAU/EMT intergrowth materials mostly utilize organics or cations other than sodium.[100,105] However, Davis reported the synthesis of VPI-6, FAU/EMT intergrowth, from an inorganic synthesis gel.[106]

2.2 Experimental Methods

2.2.1 Synthesis of House-of-card-like Assembly of Faujasite Sheets

House-of-card-like assemblies of Faujasite sheets were synthesized by following the procedure reported by Inayat et al.[70] but by replacing TPHAC, 3-(trimethoxysilyl) propyl hexadecyldimethyl ammonium chloride, by its homologue, 3-(trimethoxysilyl) propyl octadecyldimethyl ammonium chloride (TPOAC), which is commercially available (72 wt % TPOAC, 13 wt % methanol, 15 wt % (3-chloropropyl) trimethoxysilane from Sigma Aldrich). The synthesis gel molar composition used was 1 Al_2O_3:3.5 Na_2O:3 SiO_2:180 H_2O:0.06 TPOAC. Chemicals used in the synthesis were reagent grade sodium silicate solution (10.6% Na_2O, 26.5% SiO_2, 62.9% H_2O, Sigma Aldrich), anhydrous technical sodium aluminate (Sigma Aldrich) and NaOH (Mallinckrodt).

In a typical synthesis, 2g NaOH pellets and 3g sodium aluminate powder were dissolved in 51.1g deionized water. The sodium aluminate solution was added to 12g sodium silicate solution and they were blended mechanically for 1 hour. 0.85 mL TPOAC solution was added to the gel and it was aged for 1 day at room temperature. This was statically crystallized in polypropylene bottles at 75 °C for 4 days in a convection oven. The particles that formed were separated by repeated washing and vacuum filtration until the pH dropped to 8-9. They were then dried at 70 °C overnight and calcined at 650 °C in 80 mL/min air flow (heating ramp 2°C /min and dwell time 8h).

The synthesis was repeated using different sources of organosilane surfactant to check the reproducibility of the procedure. Different TPOAC solutions in methanol were used, namely,

1. 72 wt % TPOAC, 13 wt % methanol, 15 wt % (3-chloropropyl) trimethoxysilane from Sigma Aldrich.
2. 40-45 wt % TPOAC in methanol from Pfaltz and Bauer.
3. 42 wt % TPOAC, 50 wt % methanol, 8 wt % (3-chloropropyl) trimethoxysilane from Sigma Aldrich.

2.2.2 Material Characterization

Samples for Transmission Electron Microscopy (TEM) studies were prepared by applying a few drops of a zeolite suspension in ethanol onto a copper grid coated with Lacey Formvar/Carbon (Ted Pella Inc.) and leaving it to dry at room temperature. To study faulting in the structure, zeolite thin-sections were prepared by embedding zeolite powder in PolyBed 812 (Polysciences Inc.). 50 nm thick sections were prepared using a diamond knife on a Leica EM UC6 Ultramicrotome. The sections were collected on TEM grids for examination. TEM imaging and diffraction were performed on FEI Tecnai G2 F30 TEM operating at 300 kV and FEI Tecnai T12 TEM operating at 120 kV. All TEM images were captured using a CCD camera.

Samples for Energy Dispersive X-ray (EDX) analysis were prepared by applying a few drops of a sonicated zeolite suspension in ethanol onto a copper grid coated with holey carbon film (Pacific Grid Tech.). Samples were stored under vacuum (< 1E-7 torr) at a temperature of 150 °C overnight. High-Angle Annular Dark Field Scanning Transmission Electron Microscopy (HAADF-STEM) micrographs and STEM-EDX maps were acquired in an aberration-corrected FEI Titan 60-300 (S)TEM, equipped with an Analytical Super-Twin pole piece and FEI SuperX EDX detector, operating at 80 kV and having a STEM convergence angle of 15 mrad, 90 pA probe current, and 58.5 mrad HAADF inner angle. EDX spectrum maps were acquired using the Bruker Esprit software in a series of four low-dose acquisitions, approximately 10^5 electrons/nm^2 each, until zeolite size appeared to stabilize (i.e. shrinking due to beam damage stopped). A final high dose acquisition, approximately 10^6 electrons/nm^2, was then performed. All scans used an 18 µsec pixel dwell time with probe step size between 0.6 and 2.0 nm and variable frame size to obtain a map of the respective zeolite sheet. EDX net count maps of the Si Kα and Al Kα peaks were generated using the Esprit software with additional elemental consideration of sodium, carbon, oxygen, and copper. A trace copper peak is attributed to the TEM grid and a carbon peak is attributed to the organic surfactant in uncalcined T-H-Faujasite (TPOAC-hierarchical-Faujasite=T-H-Faujasite) and the carbon support film.

Scanning Electron Microscopy (SEM) images of uncoated samples on carbon tape were collected using a JEOL JSM-6700F scanning microscope operated at 3 kV.

X-ray Diffraction (XRD) patterns were acquired using a PANalytical X'Pert PRO MPD X-ray diffractometer, operated at 45 kV and 40 mA, equipped with a Co source.

Argon adsorption (87.3 K) was performed using a commercially available automatic manometric sorption analyzer (Quantachrome Instruments AutosorbiQ MP). Prior to adsorption measurements, the samples were outgassed at 573 K for 16 h under turbomolecular pump vacuum. Pore size distribution curves were calculated from the adsorption branch of the isotherm according to the Quantachrome density functional theory kernel for Argon at 87 K in spherical/ cylindrical zeolite pores.[107]

Inductively Coupled Plasma - Optical Emission Spectrometry (ICP-OES) analysis was done on a Thermo Scientific iCAP 6500 duo optical emission spectrometer fitted with a simultaneous charge induction detector. For each sample, standard, and blank, the data was replicated 5 times to determine a mean and standard deviation for each selected elemental wavelength. Samples were prepared by dissolving approximately 100-150 mg of zeolite powder in 1 ml of deionized water, 3 ml of nitric acid, 1.5 ml of hydrofluoric acid, and 1.5 ml of hydrochloric acid at 200 °C in a CEM Discover SP-D microwave system for 15 minutes. 14 ml of 4% Boric Acid solution in water was added and this solution was digested in the same manner for 10 minutes at 165 °C. Finally, 9 ml of deionized water was added to make the solution ready for further dilution and analysis. Samples were atomized and introduced to the instrument by a free aspiration or peristaltic pump rate of approximately 1 ml/min into a standard meinhardt concentric nebulizer.

Atomic Force Microscopy (AFM) measurement was done on a Bruker Nanoscope V Multimode 8 atomic force microscope in tapping mode in the repulsive regime. Sample was prepared by placing a drop of sonicated T-H-Faujasite in ethanol on silicon wafer followed by drying at ambient conditions. Image analysis was performed with Gwyddion

2.36 software. Height calibration was done using 2.0 and 1.0 nm steps on freshly cleaved muscovite mica etched in 50% Hydrofluoric acid for 4 hours.[108]

2.2.3 Electron Diffraction and Image Simulations

Electron diffraction and HRTEM image simulations were performed using the multislice method[109,110] code developed by Kirkland.[111] In this method the specimen is divided into thin two-dimensional slices along the electron beam direction and the electron beam alternately gets transmitted through a slice and propagates to the next slice. At each slice the electron wave function experiences a phase shift due to the projected atomic potential of all atoms in the slice and is then propagated for the thickness of the slice. Calculating the wave function sequentially through each slice needs much less computational resources compared to doing the calculation through all the atoms in a sample.

Atomic coordinates for FAU and EMT were taken from Accelyrs Material Studio Software. The projected atomic potentials were calculated by slicing the structure into 1 Å thick layers along $[111]_{FAU}$ /$[001]_{EMT}$. A buffer zone was placed around the crystal creating a super cell to avoid wrap-around error.[111] Simulations were done using 120 keV, 1024 Nx *1024 Ny pixels wave function, and no partial coherence and thermal vibrations. Coherent real space image simulations were done at 800 Å defocus, spherical aberration Cs3 of 2.2 mm and Cs5 of 0 mm, 10 mrad objective aperture and 2 fold and 3 fold astigmatism 0 Å and 0°, respectively.

2.3 Results and Discussion

Conventional FAU (C-FAU), obtained in the absence of surfactant, has a compact octahedral morphology (Fig. 2-2a). The house-of-cards arrangement of Faujasite sheets reported by Inayat et al.,[70] obtained in this work by using a homologous surfactant with two additional carbon atoms in the alkyl chain (3-(trimethoxysilyl) propyl octadecyldimethyl ammonium chloride, TPOAC), was confirmed using SEM (Fig. 2-2b). The house-of-cards Faujasite (TPOAC-hierarchical-Faujasite=T-H-Faujasite), was

achieved using different sources of organosilane surfactant given in section 2.2.1 (Fig. 2-3).

XRD was used to identify the crystal phases of the materials. The patterns for T-H-Faujasite and C-FAU were successfully indexed as FAU based on peak positions only (Fig. 2-2c). However, the relative intensities of the peaks do not match those of a pure FAU material, which might be an indication of faulting in the structures.[112–114] Similar observation was noted for CSZ-1, FAU/EMT intergrowth material that has a similar XRD pattern as zeolite Y but with peaks of different relative intensities.[77] The relative intensities also differed between T-H-Faujasite and C-FAU.

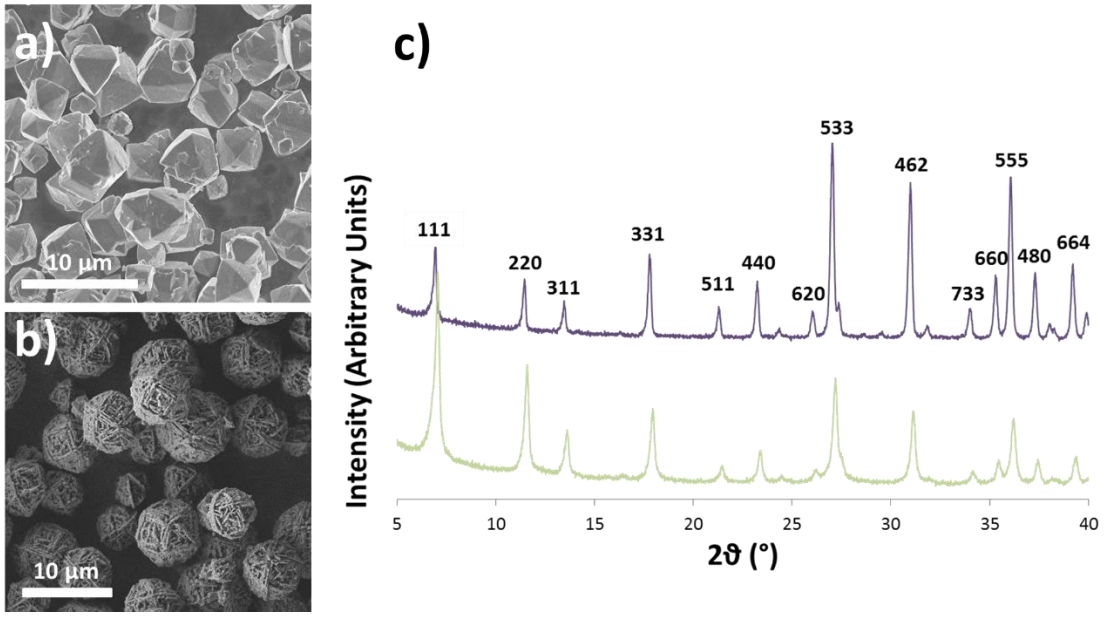

Figure 2-2: SEM images of a) C-FAU (octahedral morphology) and b) T-H-Faujasite (house-of-cards arrangement of nanosheets) using 72 wt % TPOAC from Sigma Aldrich. c) XRD patterns for calcined T-H-Faujasite (bottom) and C-FAU (top). Crystallinity is retained after calcination at 650 °C.

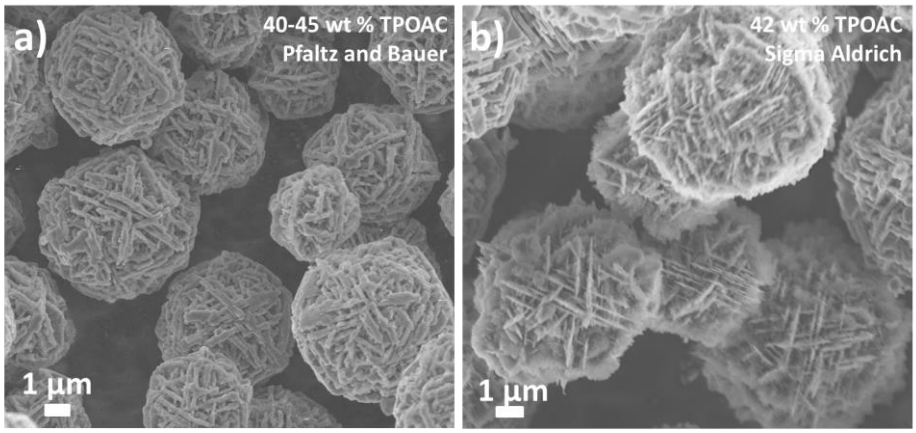

Figure 2-3: SEM images of T-H-Faujasite synthesized using a) 40-45 wt % TPOAC in methanol from Pfaltz and Bauer and b) 42 wt % TPOAC, 50 wt % methanol, 8 wt % (3chloropropyl) trimethoxysilane from Sigma Aldrich. Both TPOAC sources yield the house-of-card morphology.

To gain more insight into the evolution of T-H-Faujasite particles with time, the crystallization was followed with SEM (Fig. 2-4). After 1 day at 75 °C, crystalline sheets are observed along with amorphous aluminosilicate. This shows that the anisotropic sheets form rapidly at the beginning of the process and then grow larger during crystallization, consuming the amorphous aluminosilicate.

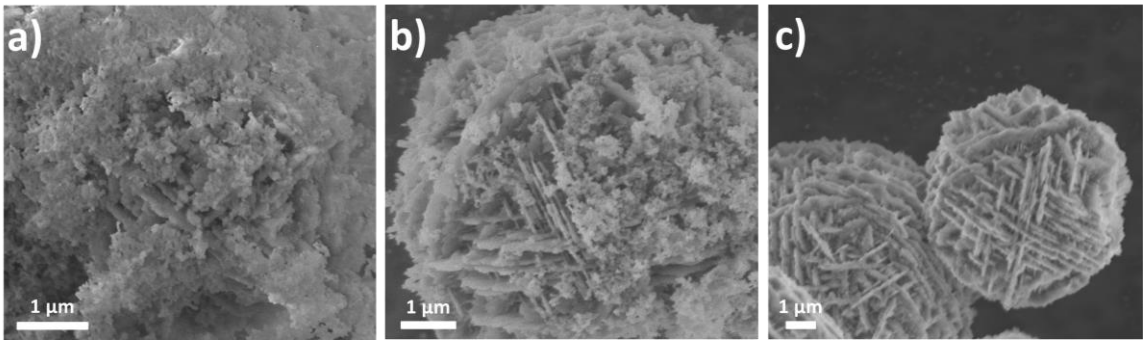

Figure 2-4: SEM images showing the evolution of T-H-Faujasite particles with time after a) 1 day, b) 2 days and c) 3 days synthesis at 75°C. Crystalline sheets are observed from day 1 along with amorphous aluminosilicate that is mostly consumed by day 4.

Argon physisorption was used to study the porosity of T-H-Faujasite and C-FAU. Pore size distributions were calculated from the adsorption branches of Ar isotherms according to the Quantachrome density functional theory kernel for Argon at 87 K in cylindrical/spherical zeolite pores.[107] The micropore volume of T-H-Faujasite is less than

that of C-FAU (Fig. 2-5a,b). In addition to the conventional zeolite microporosity, T-H-Faujasite contains 5.5 nm mesopores (Fig. 2-5c) within the Faujasite sheets, as reported by Inayat et al.[70] and evidenced by TEM (Fig. 2-5d).

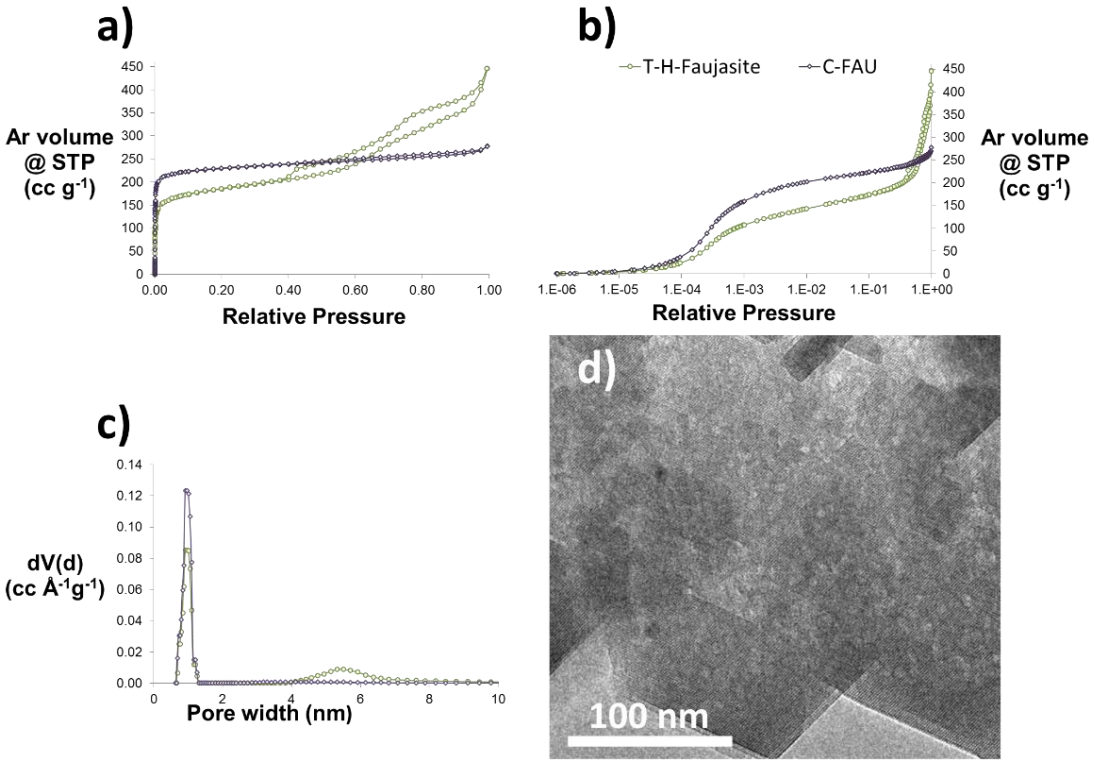

Figure 2-5: Argon physisorption isotherms at 87K for T-H-Faujasite and C-FAU, a) linear scale and b) semi-logarithmic scale to highlight the low relative pressure region, showing lower microporosity for T-H-Faujasite. c) Pore size distributions up to 10 nm for calcined T-H-Faujasite and C-FAU calculated from the adsorption branches of Ar isotherms according to the Quantachrome density functional theory kernel for Argon at 87 K in cylindrical/spherical zeolite pores.[107] d) TEM image showing mesopores within the Faujasite sheets.

Nuclear Magnetic Resonance (NMR) spectra for T-H-Faujasite before and after calcination are shown in Fig. 2-6. Both ^{29}Si NMR spectra (Fig. 2-6a,b) show the resolution into five Si(nAl) bands. The band shape and position change with composition and the resolution obtained agrees with high Al Faujasite zeolite.[115] ^{29}Si CP (Cross Polarization) NMR shows an additional broad and weak peak centered around -57 ppm for T-H-Faujasite before calcination (Fig. 2-6c). This resonance is assigned to Si-C bonds and is not observed for T-H-Faujasite after calcination (Fig. 2-6d). The position of the resonance band from organosiloxane [$RSi(OSi)_m(OH)_{3-m}$, m = 1-3] depends on the

coordination. It has been reported to be at -68 ppm for m=3 and -56 ppm for m=2 in the case of ZSM-5.[116] The resonance for tetrahedrally coordinated Si bonded to one carbon has been reported at -60 ppm for Faujasite X zeolite.[117] The Si-C resonance does not show in ^{29}Si NMR because of its low concentration.

Evidence of Si-C bonds can also be seen in ^{13}C CP NMR (Fig. 2-6e). The broad peak at ~ 10 ppm can be assigned to the Si-C bonds (agreeing with the broad peak in ^{29}Si CP NMR). This shows that the organic is stable under the reaction conditions. No peaks are observed for the calcined particles (Fig. 2-6f), showing complete removal of the organic upon calcination at 650 °C. The resonance at 53 ppm and 60-70 ppm can be assigned to the methyl and methylene groups, respectively, attached to the ammonium nitrogen. A peak at ~ 13 ppm was not detected indicating that the CH_3 end carbon on the surfactant chain is probably in mobile environment (i.e. in the mesopores).[118] ^{27}Al NMR spectra for T-H-Faujasite before and after calcination show only one resonance at around 59 ppm assigned to (tetrahedral) Al incorporated in the framework (Fig. 2-6g-h).[119] This shows that no significant octahedral Al was formed after calcination.

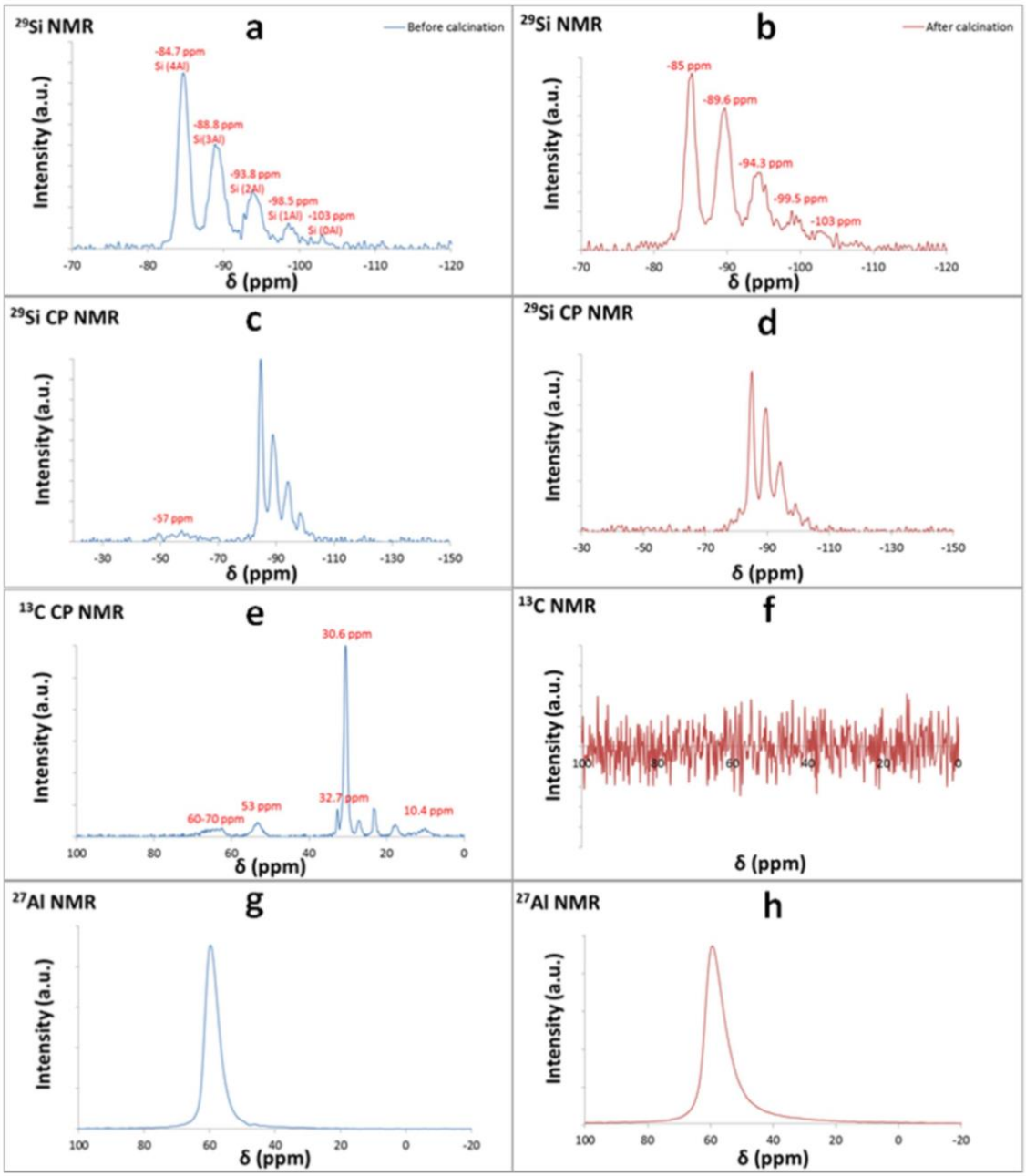

Figure 2-6: ^{29}Si NMR spectra for T-H-Faujasite a) before and b) after calcination agreeing with high Al Faujasite zeolite.[115] ^{29}Si CP NMR spectra for T-H-Faujasite c) before and d) after calcination. e) ^{13}C CP NMR spectrum for T-H-Faujasite before calcination. f) ^{13}C NMR spectrum for T-H-Faujasite after calcination. ^{29}Si CP NMR and ^{13}C CP NMR spectra show Si-C resonance before calcination and complete removal of the organic upon calcination at 650 °C. ^{27}Al NMR spectra for T-H-Faujasite g) before and h) after calcination showing that Al is incorporated in the zeolite framework.

As shown in Fig. 2-7a, the intergrown nanosheets in T-H-Faujasite form a skeletal cuboctahedron, such that from one direction a triangular assembly of sheets with 3-fold symmetry is observed (Fig. 2-7b) (corresponding to a triangular face in a cuboctahedron), and another direction shows a square assembly of sheets with a 4-fold symmetry (corresponding to a square face in a cuboctahedron). The cuboctahedron is a habit of cubic crystals as shown in Fig. 2-7c. The arrangement of T-H-faujasite sheets into this cuboctahedral skeletal arrangement can be easily visualized by the assembly of four hexagonal plates (≡ 4 {111} planes) with interpenetration angles of 70.5º and 109.5º between any two plates (Fig. 2-7d).

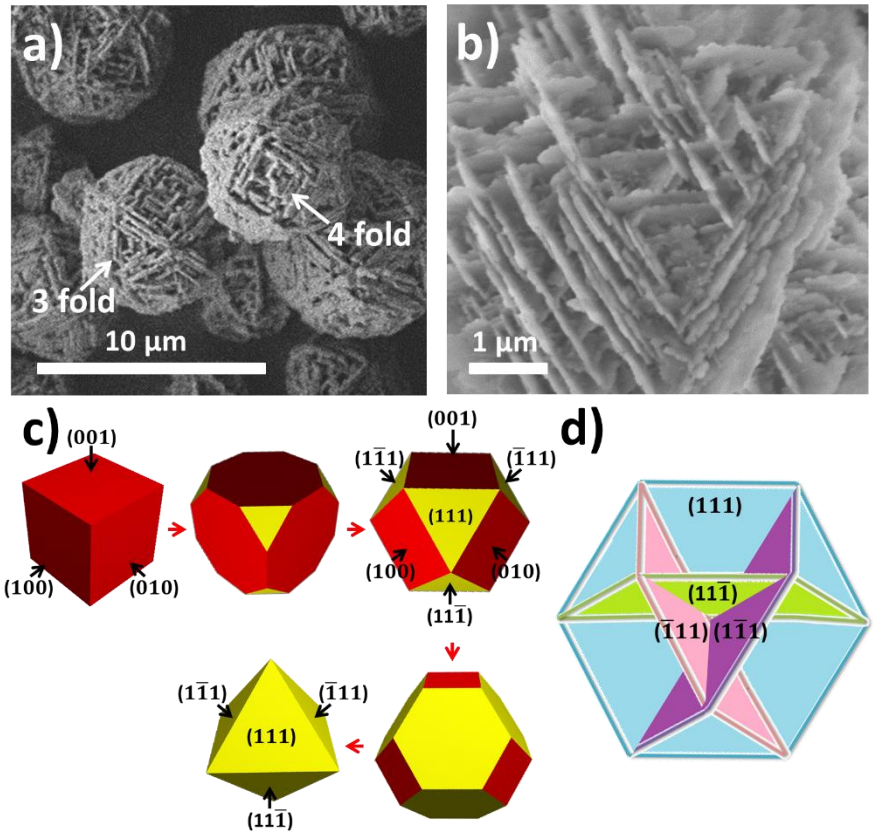

Figure 2-7: a) SEM image showing the cuboctahedral skeletal arrangement of sheets in T-H-Faujasite (3-fold and 4-fold symmetries in sheet arrangements are evident). b) SEM image highlighting the triangular assembly of T-H-Faujasite sheets with 3-fold symmetry (corresponding to a triangular face in a cuboctahedron). c) Evolution of the cubic crystal habit from cube to octahedron (produced using Stella4D), {111} and {100} planes are labelled. d) Assembly of four hexagonal (111) plates with interpenetration angle of 70.5° or 109.5° between any two plates resulting in a cuboctahedral skeletal arrangement exhibiting 3-fold and 4-fold symmetric arrangement of plates.

A confirmation that the thin dimension of the nanosheets coincides with $[111]_{FAU}$ is shown in Fig. 2-8. By sonicating T-H-Faujasite in ethanol for a few minutes, some sheets get dislodged from the particles. Fig. 2-8a shows a high-resolution TEM image [inset: Fast Fourier Transform (FFT)] of such a sheet with a hexagonal symmetry, indicating that the thin dimension of the sheet coincides with $[111]_{FAU}$. In agreement with Inayat et al.,[70] mesoporosity is evident within the sheets (see arrows in Fig. 2-8a). Fig. 2-8c shows electron diffraction from another sheet with a hexagonal projection (Fig. 2-8b). The electron diffraction pattern shows that the sheet is single-crystalline and has a hexagonal symmetry showing a hexagonal array of more intense spots, marked with A, which index according to the FAU <111> zone axis and intervening weaker spots, marked with B, which index according to the EMT < 0001 > zone axis. This confirms the conclusion drawn from high-resolution imaging that the thin dimension of the sheets coincides with $[111]_{FAU}$ and provides evidence for the possible presence of EMT. The relationship between FAU and EMT structures and their intergrowth is reviewed in section 2.1.2. The fact that the intensities of the reflections marked by B are weak when compared to the A reflections, indicates that the sheet is not completely recurrently faulted.[120]

Electron diffraction simulations show that the reflections marked with B in Fig. 2-8c can arise from regions of EMT intergrowing with FAU (Fig. 2-9),[120] or from an incomplete cubic stacking sequence of Faujasite layers for thin FAU sheets in the absence of EMT (Fig. 2-10). The former will be confirmed in the following results.

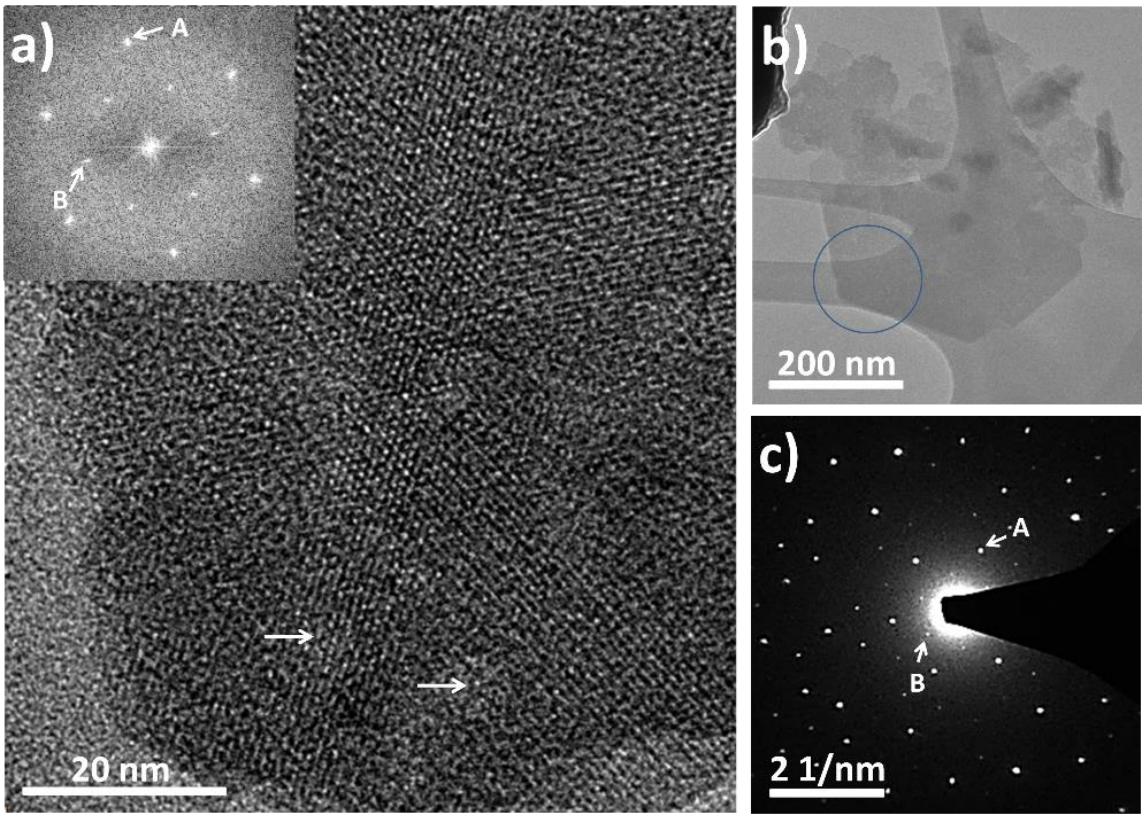

Figure 2-8: a) High-resolution TEM image showing a crystalline mesoporous sheet dislodged by sonication of T-H-Faujasite in ethanol (mesopores are indicated by arrows) and inset FFT showing hexagonal symmetry. b) Low-magnification TEM image of a hexagonal sheet dislodged by sonication of T-H-Faujasite in ethanol. c) Electron diffraction pattern of a selected area from the part of the sheet marked in (b). The reflections marked with A index according to the FAU < 111 > zone axis and those marked with B index according to the EMT < 0001 > zone axis. Electron diffraction patterns are indexed in Fig. 2-9.

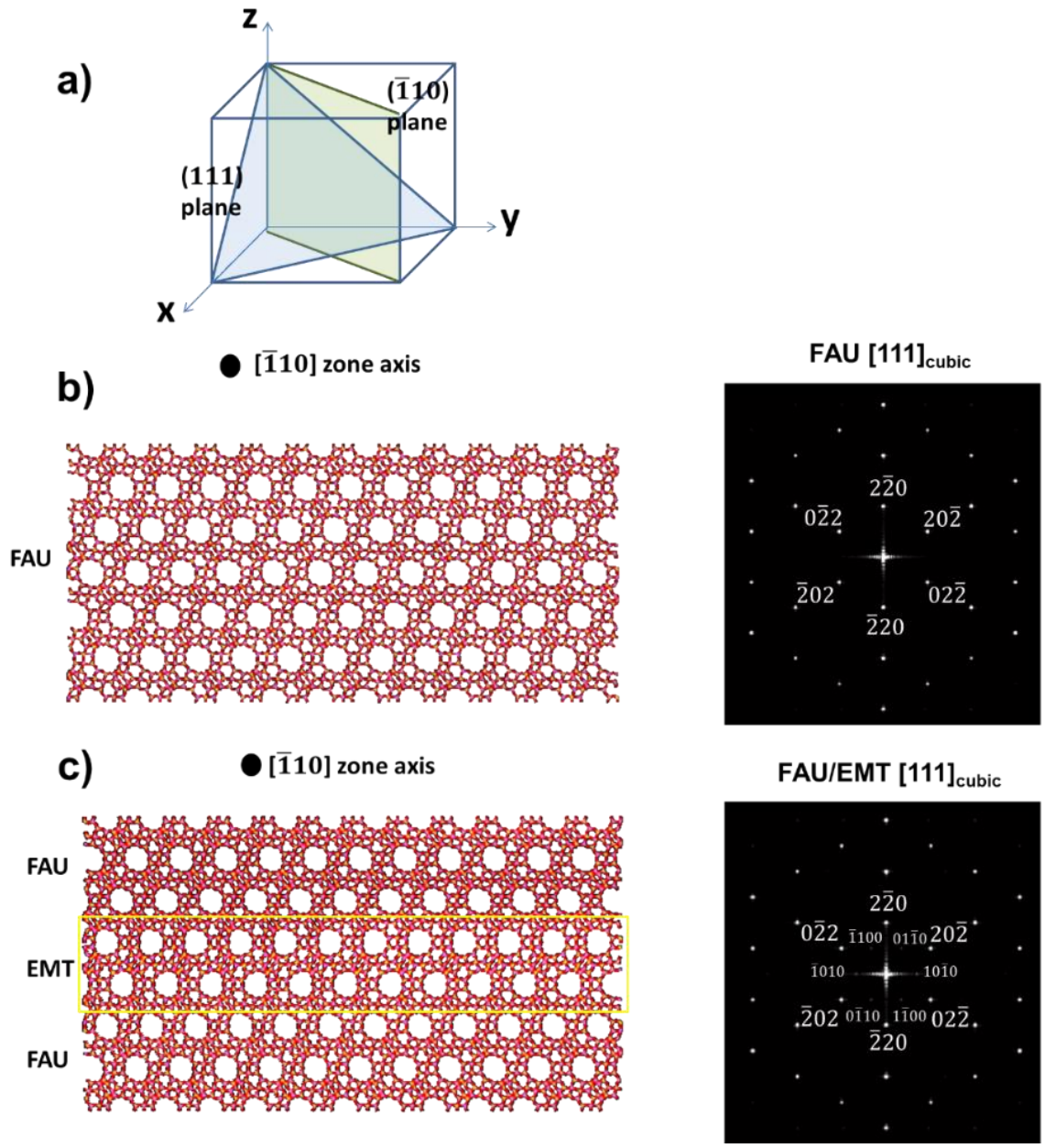

Figure 2-9: a) Illustration showing (111) and $(\bar{1}10)$ planes in a cubic unit cell. $[\bar{1}10]$ structure view and simulated electron diffraction pattern along $[111]_{cubic}$ zone axis for b) FAU and c) FAU/EMT intergrowth with 1 EMT unit cell along $[111]_{cubic}$. Simulations were done using TEMSIM for a 120kV microscope.[111]

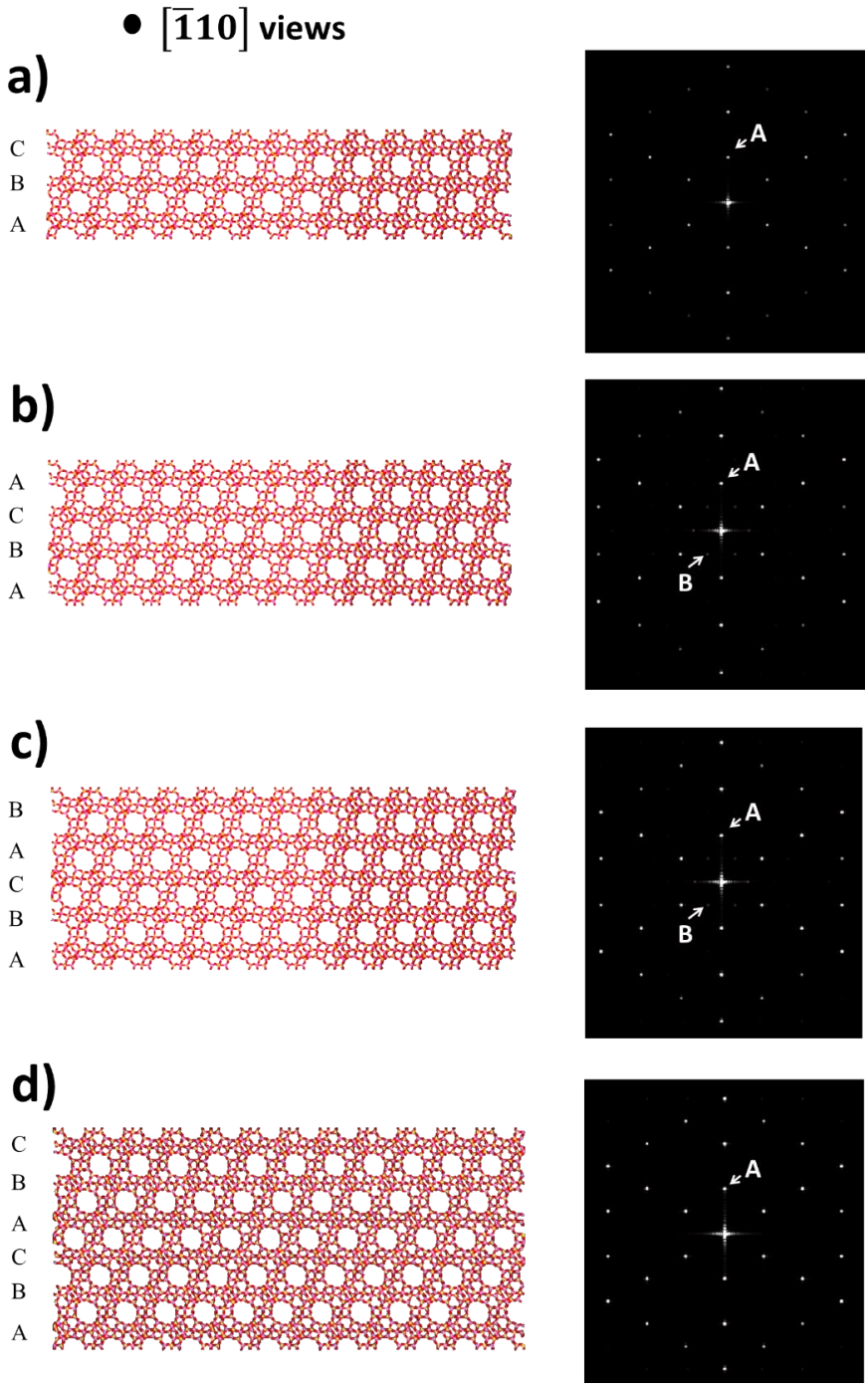

Figure 2-10: $[\bar{1}10]$ views and simulated electron diffraction patterns along $[111]_{cubic}$ zone axis for a) ABC, b) ABCA, c) ABCAB and d) ABCABC sequences of Faujasite sheets. The hexagonal array of spots marked A, index according to FAU <111> zone axis and the intervening weaker spots, marked B, index according to EMT <0001> zone axis. Simulations were done using TEMSIM for a 120kV microscope.[111]

EMT domains in T-H-Faujasite were observed by high resolution TEM both from the direct examination of thin sheets dislodged by sonication and from thin sections prepared by microtomy of T-H-Faujasite particles embedded in polybed 812 (Fig. 2-11). The TEM images show single faults and EMT extending for up to two unit cells along <0001> and up to 20 nm in the directions perpendicular to <0001>. Region II marked in Fig. 2-11a is a FAU domain and region III is a faulted domain indicating that EMT domains are interrupted and enclosed by FAU domains and/or amorphous regions or mesopores. Amorphous regions, visible in Fig. 2-11b, could be partly responsible for the lower microporosity of T-H-Faujasite compared to that of C-FAU, measured by Ar adsorption (Fig. 2-5 a-b).

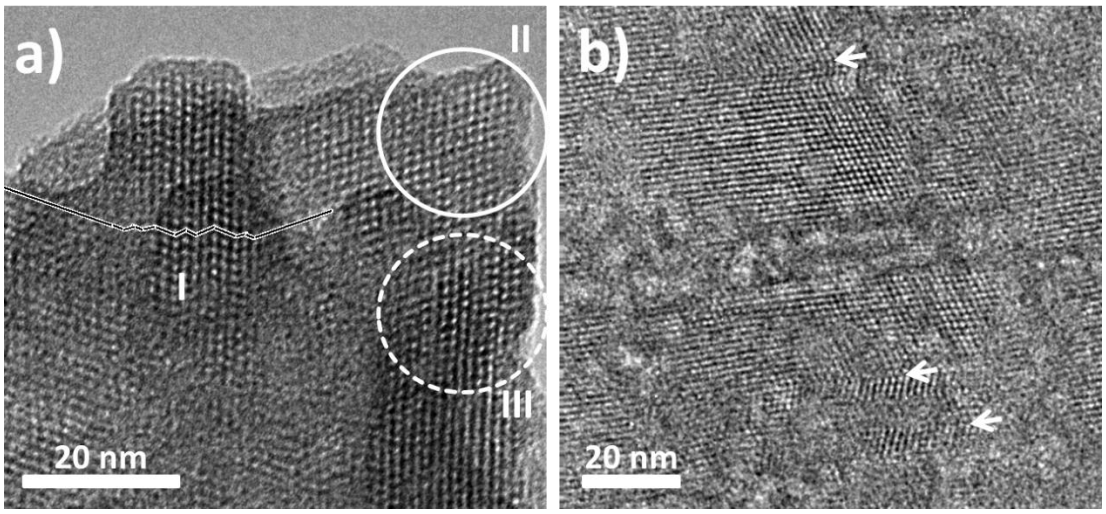

Figure 2-11: Bright-field TEM images showing a) faulting in a sheet dislodged by sonication of T-H-Faujasite in ethanol (region I shows excessive faulting and regions II (FAU) and III (faulted) show that EMT domains are enclosed by FAU domains) and b) faulting in a sheet observed from thin microtomed section of T-H-Faujasite embedded in polybed 812 (faults are marked by arrows).

Additional confirmation of the presence of EMT domains (ca. 20 nm) within the sheets is obtained by electron diffraction and imaging along the $[323]_{cubic}$ zone axis (Fig. 2-12). The diffraction pattern (Fig. 2-12b) taken from the part of the dislodged sheet marked in Fig. 2-12a shows reflections from the $[323]_{cubic}$ zone axis for FAU, mirror FAU (rotated 60° around $[111]_{cubic}$ with respect to FAU aligned along the $[323]_{cubic}$), and EMT. This is shown by the simulated diffraction pattern in Fig. 2-12c. The break-down of the domains contributing to this diffraction pattern is presented in Fig. 2-13. The same pattern of Fig.

2-12b and c was also observed by FFT from high resolution imaging along the $[323]_{cubic}$ zone axis (Fig. 2-12d and inset FFT).

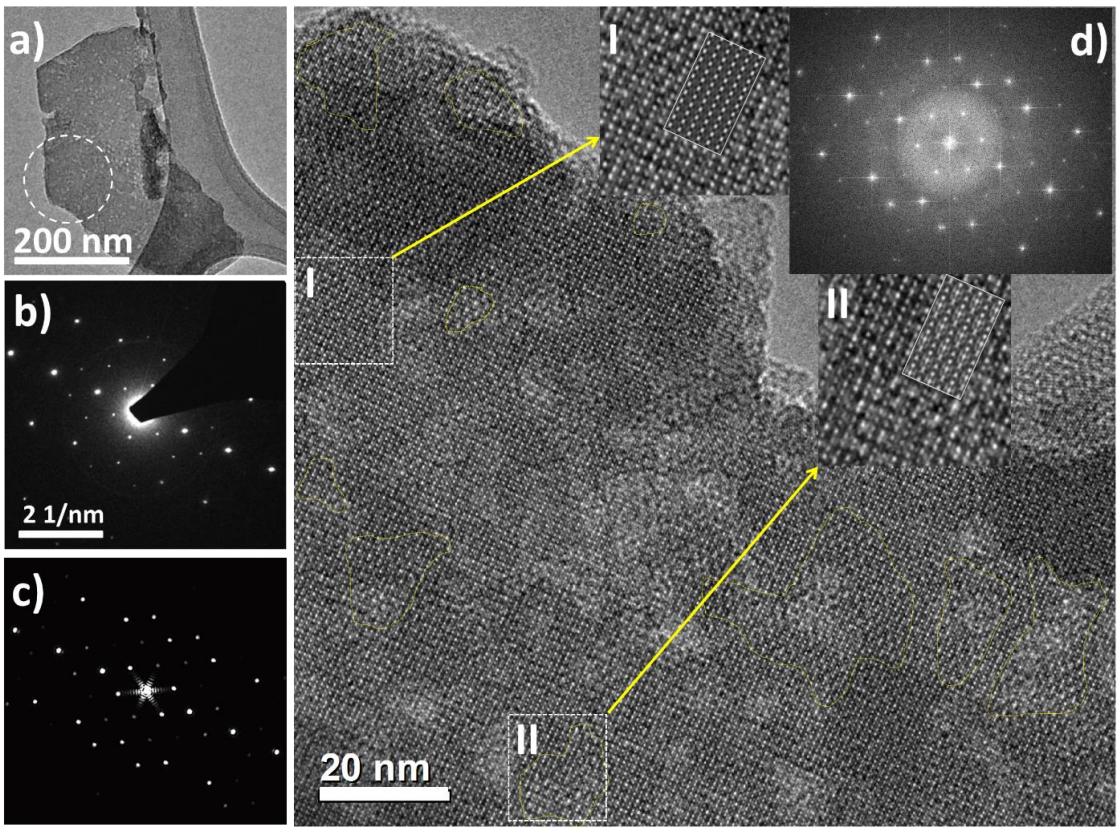

Figure 2-12: a) Low magnification TEM image of a hexagonal sheet dislodged by sonication of T-H-Faujasite in ethanol. b) Electron diffraction pattern of a selected area from the part of the sheet marked in (a). c) Simulated electron diffraction pattern from the $[323]_{cubic}$ zone axis for FAU, mirror FAU (rotated 60° around $[111]_{cubic}$ with respect to FAU aligned along $[323]_{cubic}$), and EMT. d) The $[323]_{cubic}$ high-resolution TEM image of a sheet (inset FFT) with the FAU/EMT domains marked and magnified regions I (FAU) and II (FAU/EMT) superimposed by simulated $[323]_{cubic}$ high-resolution images.

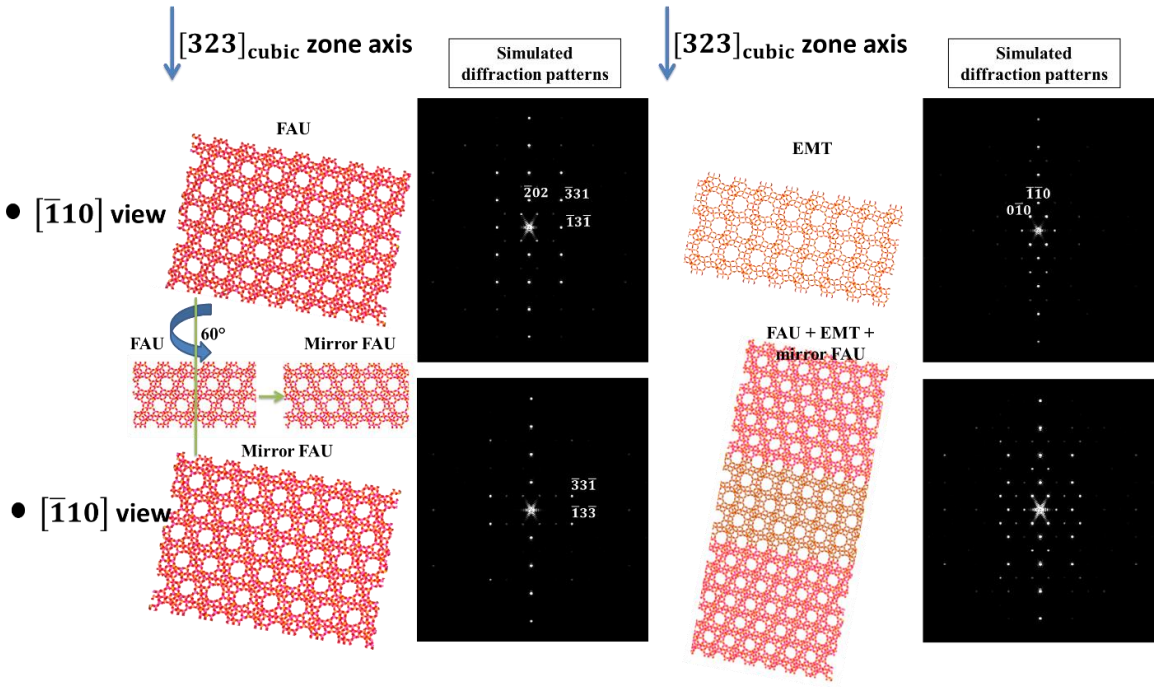

Figure 2-13: Illustration of the domains (FAU, mirror FAU and EMT) that build up a T-H-Faujasite sheet ([1̄10] views) and simulated electron diffraction pattern for each domain and their composite down [323] zone axis for FAU.

The high-resolution image motif along the $[323]_{cubic}$ zone axis can also be used to distinguish FAU-only and FAU/EMT domains in a sheet. Down this zone axis, the projection of FAU shows a rectangular pattern while that of FAU/EMT shows a centered pattern with larger features (simulations for different sizes of EMT domains presented in Fig. 2-14). Fig. 2-12d shows the experimental TEM image marking representative FAU/EMT domains as determined by the [323] motif. Magnified views of regions I (FAU-only) and II (FAU/EMT) are presented and superimposed by the simulated [323] high-resolution images for FAU and FAU/EMT, respectively. This interpretation is also supported by image filtering, in which the removal of the EMT reflections from the FFT returns a high-resolution image without large, centered features (Fig. 2-15). The $[323]_{cubic}$ view is in agreement with the $[111]_{cubic}$ view. In addition, it has the advantage of revealing the small portions of included EMT domains in the predominant FAU matrix.

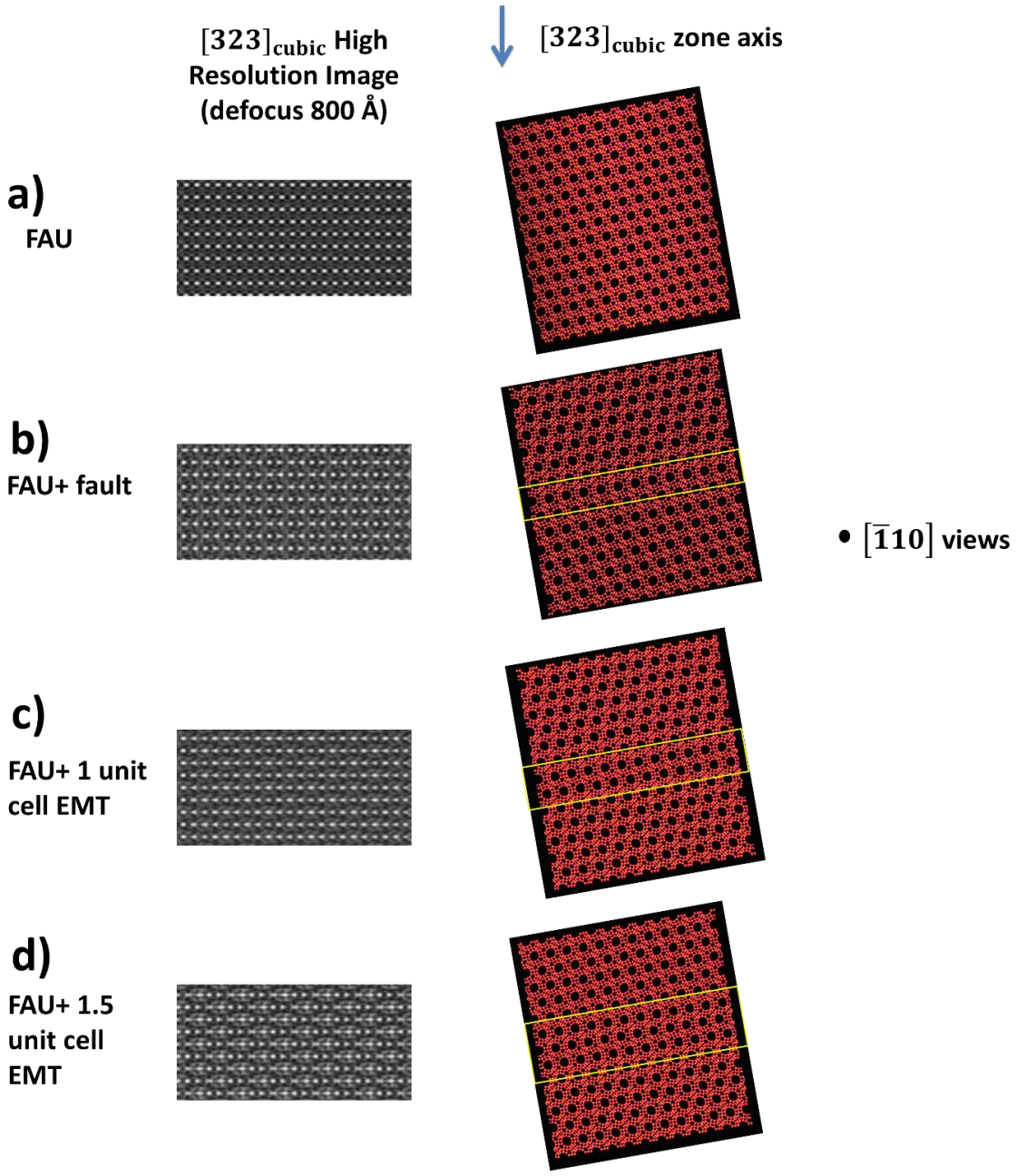

Figure 2-14: $[323]_{cubic}$ simulated high resolution images at 800 Å defocus and $[\bar{1}10]$ views for a) FAU , b) FAU + fault, c) FAU + 1 unit cell EMT and d) FAU + 1.5 unit cell EMT. The $[323]_{cubic}$ zone axis is indicated. Adding EMT to FAU creates larger, centered features in the projected view.

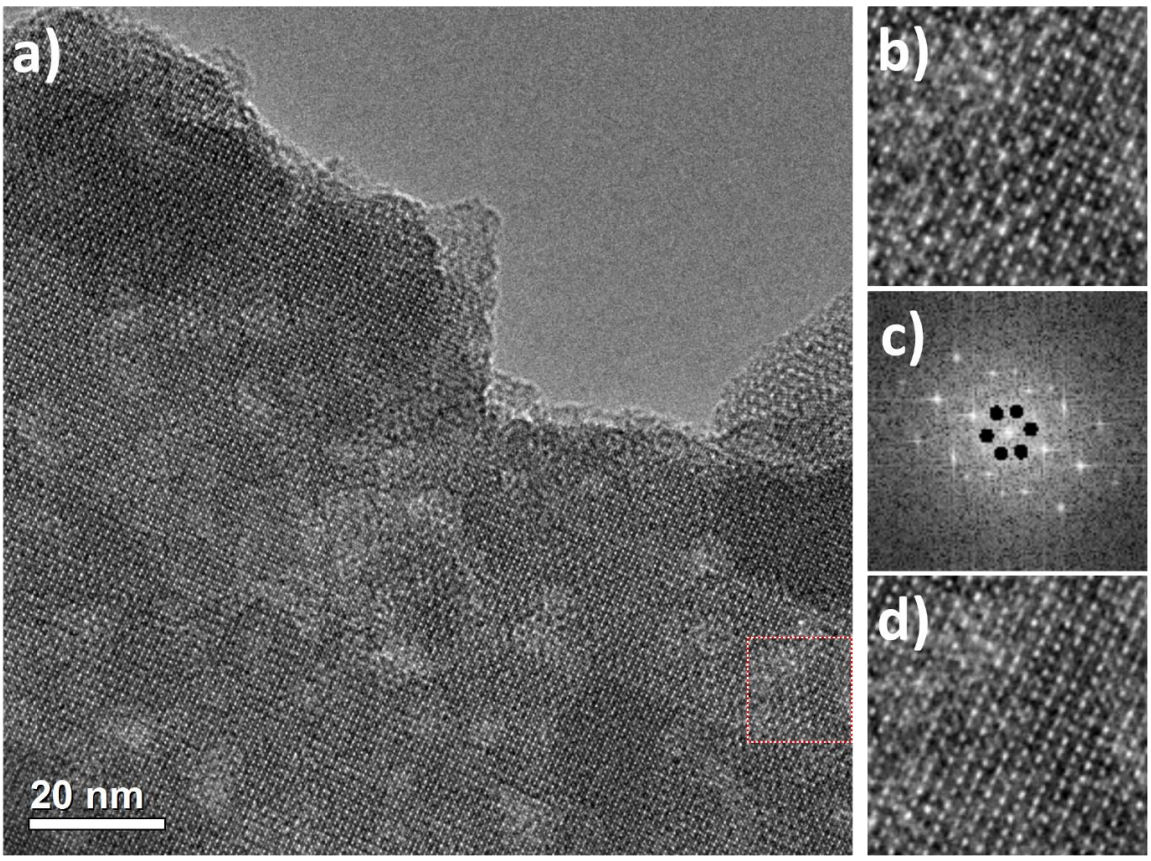

Figure 2-15: a) $[323]_{cubic}$ high resolution TEM image of T-H-Faujasite sheet, b) magnified view of the FAU/EMT region marked in (a) showing large features with centered pattern, c) FFT from (b) indicating with black dots the EMT reflections and d) filtered high resolution image from (b) excluding the EMT reflections marked by dots in (c).

The results presented above show that T-H-faujasite: 1) at the particle level has a cuboctahedron morphology consistent with cubic FAU; 2) each cuboctahedron particle consists of a skeletal arrangement of nanosheets interpenetrating at 70.5° or 109.5°; 3) each nanosheet is thin along the $<111>_{cubic}$ axis, and is predominantly composed of FAU, with EMT present in small isolated domains that do not give rise to XRD peaks. The presence of these hardly detectable EMT domains appears to be the necessary ingredient for the formation of T-H-Faujasite.

Scanning Transmission Electron Microscopy (STEM) analysis was performed to identify variations in the Si/Al ratio across the nanosheets. Fig. 2-16 shows the High-Angle Annular Dark-Field (HAADF) STEM images and the STEM Energy Dispersive X-ray

(STEM-EDX) Si/Al net count heat maps of sheets dislodged by sonication in ethanol. The HAADF images show spots with dark contrast corresponding to the mesopores of about 5 nm in size. Due to beam damage, the zeolite particles lose their crystallinity. The loss of crystallinity apparently densifies the particles and some shrinkage is evident by observing a sequence of TEM images at different stages of electron beam exposure (net doses as high as 10^6 electrons per nm^2). However, this damage appears to be local, as there are no apparent changes in the contrast attributed to the mesopores with increased electron beam exposure. Therefore, we believe that despite the electron beam damage, the Si/Al ratio determined by EDX is representative of that in the undamaged sample. Unlike silicon and aluminum, sodium migrates fast out of the sample and is found in the vicinity of the zeolite particles on the copper grid. The EDX Si/Al net count heat maps show that, on a 10 nm scale, there is a factor of 2.5 variation in Si/Al across the sheets. At this level of resolution, we find no evident correlation of the Si/Al ratio with morphological features like surface steps and pores. Moreover, due to the beam damage, we are not able to conclude if the differences in Si/Al are associated with the FAU/EMT versus FAU-only domains discussed in Fig. 2-12. This should be the subject of further investigations.

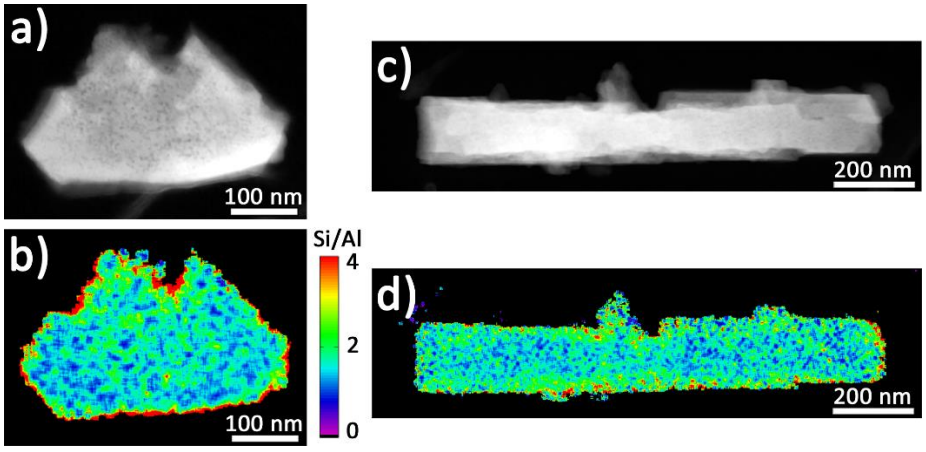

Figure 2-16: HAADF-STEM image and STEM-EDX Si/Al net count heat map of the top (a and b, respectively) and side views (c and d, respectively) of two different sheets. The color code bar on the right of the heat maps indicates the colors for a Si/Al ratio range from 0 to 4.

The edges of the sheets show an apparent higher Si/Al ratio compared to the bulk. This is believed to be an artifact resulting from the low counts per pixel at the thin edges. It arises from the small dwell time needed to limit beam damage coupled with the reduced interaction volume at the thin particle edges. This was concluded by careful examination of the number of X-ray counts and is supported by X-ray photoelectron spectroscopy (XPS) data, which do not show a Si-rich surface for the sheets (the Si/Al ratio on the surface of the zeolite particles was determined by XPS to be 1.7). The average Si/Al ratios obtained from EDX measurements for both sheets (excluding edges) is 1.6, which, considering that we did not use a calibration standard, is in good agreement with the Si/Al ratio determined by inductively coupled plasma optical emission spectroscopy (ICP-OES) (1.4) and SEM EDX (1.3). This shows that the particles have a high Al content and are classified as zeolite X.[91]

In the following discussion we will present a conceptual growth model for T-H-Faujasite. According to the Hartman–Perdok theory, FAU {111} faces are classified as "F faces" (flat and slow growing faces), because they have three coplanar periodic bond chains (PBCs) within a slice of thickness d_{111}.[121] The perpendicular <111> directions to these faces are the directions along which the Faujasite layers stack and can fault. Intergrowth is possible because the (111) plane in FAU is identical to the (0001) plane in EMT. For a pure FAU phase, the growth is isotropic. However, if instead of inversion, a mirror plane (fault) forms along one of the four Faujasite sheet stacking directions, a local hexagonal (EMT) structure is created supporting anisotropic growth. For EMT, the in-plane growth perpendicular to <0001> has been reported to be 15 times faster than the growth along <0001> and is reflected in the hexagonal platelet morphology of EMT.[103] The fast in-plane growth of EMT is anticipated by the Hartman–Perdok PBC theory, which states that the dimension of a crystal along a particular direction is proportional to the bonding strength along that direction. Each sodalite cage has three double-6 member ring connections along a (0001) plane and only one connection either to the Faujasite layer above or below. Less bonding along the $<0001>_{hex}$ axis favors in-plane growth. This is also anticipated by the Bravais–Friedel–Donnay–Harker (BFDH) theory, because the

<0001> spacing in EMT is the largest and therefore the growth along this direction is expected to be the slowest. According to these arguments based on PBC and BFDH theories and prior experimental evidence, the EMT domains are necessary for the nanosheet morphology to develop. The small size of EMT domains is apparently a result of the simultaneous multiple nucleation of FAU and EMT on {111} faces in a growth regime favoring 2D nucleation and slower (with respect to nucleation) in-plane propagation such that as growth progresses, EMT gets overgrown by the predominant FAU (Fig. 2-17). It is likely that the organosilane surfactant used for the T-H-Faujasite synthesis as a mesoporogen also acts, upon incorporation at a growth front, to retard the propagation of the nucleated islands.

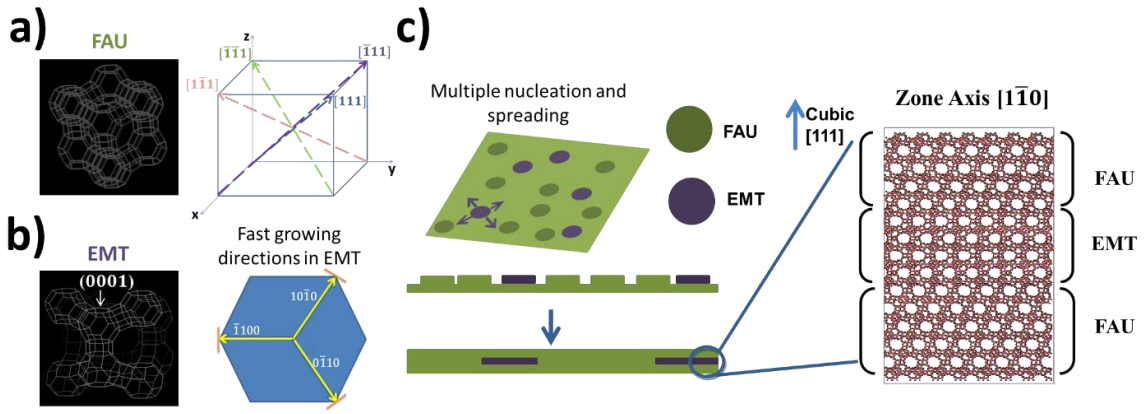

Figure 2-17: a) FAU cubic crystal structure and illustration of the four distinct <111> directions perpendicular to the {111} cubic faces. b) EMT hexagonal crystal structure and illustration of the fast in-plane growth directions for EMT (<10$\bar{1}$0>, <$\bar{1}$100> and <0$\bar{1}$10>). c) Kinetic roughening regime characterized by simultaneous multiple nucleation of FAU and EMT on {111} faces and sequential overgrowth of EMT by predominant FAU.

This model is supported by AFM measurements on dislodged T-H-Faujasite sheets (deposited on a silicon wafer) that show the presence of islands with lateral dimensions and heights as small as approximately 20 nm and 1 nm, respectively (Fig. 2-18). Steps with heights corresponding to one (1.42 nm) and two (2.85 nm) Faujasite layers were observed frequently, but not exclusively, on these surfaces. This surface structure might not be indicative of the surface structure under growth conditions, but it is consistent with the TEM observations and the proposed growth model.

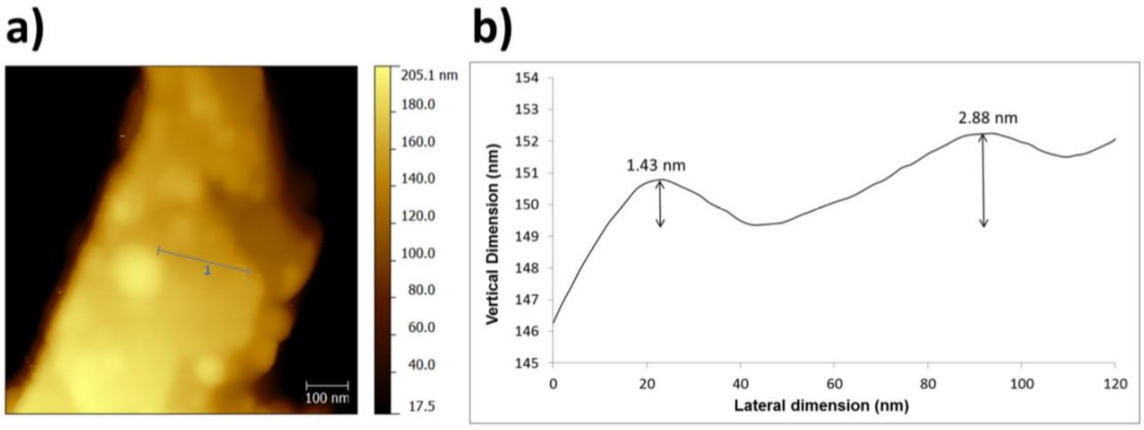

Figure 2-18: a) AFM topographical image of dislodged T-H-Faujasite sheet lying flat on silicon wafer. b) Height profile labelled '1' in (a) revealing surface roughness of 1.43 nm (one Faujasite layer thick) and 2.88 nm (two Faujasite layers thick).

The remaining question is how branching happens. If growth proceeds by nucleating FAU and EMT on a single (111) face, fast propagation in-plane will lead to sheets. A different event has to happen at the branching points. We argue that EMT island nucleation at the edge of a nanosheet is responsible for branching. EMT nucleation is a random event and happens on all {111} faces. If EMT nucleates on a vicinal {111} plane near the edge of the basal plane, it can extend along its fast growing direction before being overgrown by FAU domains. Fig. 2-19 shows an example, in which EMT nucleation at the edge of a sheet (sheet 1), on its (111) and $(11\bar{1})$ faces, is followed by branching to form sheet 2. Further growth leads to sheet interpenetration. Sheet 2 eventually thickens and gets surrounded by FAU and branching can happen on this sheet as well. Other possible scenarios are presented in Fig. 2-20 and different interpenetration possibilities are presented in Fig. 2-21. It should be noted that sheet 2 does not necessarily contact sheet 1 throughout its plane dimensions. This is supported by Fig. 2-19b, which shows out-growing sheets that are laterally much smaller than the basal sheet in the image plane.

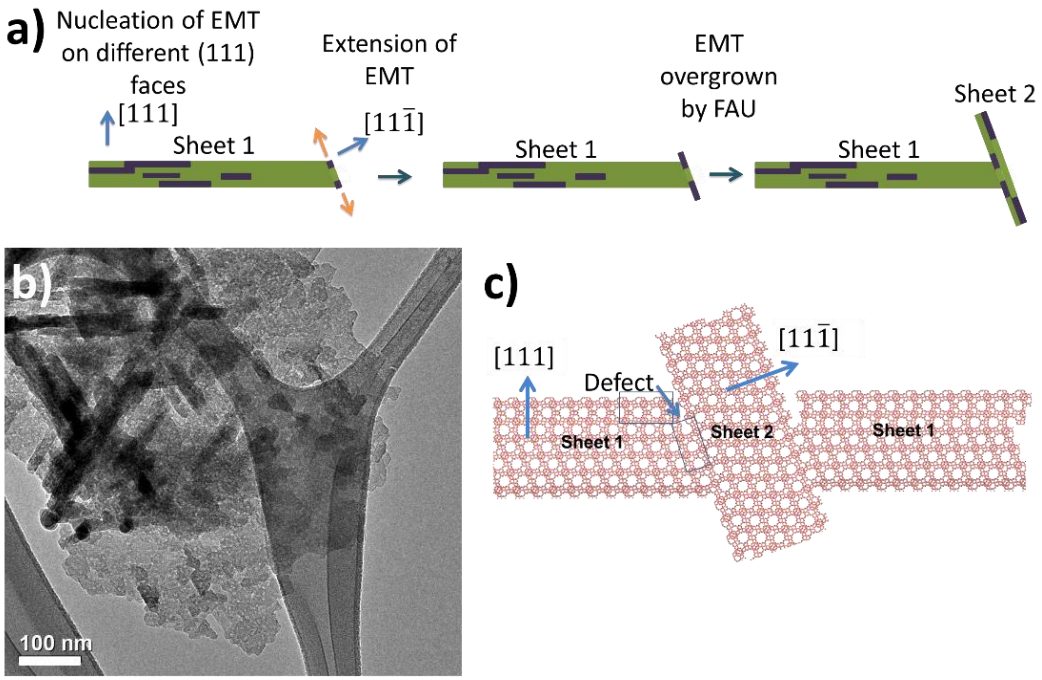

Figure 2-19: Illustration of the branching mechanism in T-H-Faujasite. a) Nucleation of EMT close to the edge of sheet 1 on (111) and (11$\bar{1}$) followed by its extension along its fast growing direction before being overgrown by FAU domains leads to branching of sheet 2. b) TEM image highlighting the triangular assembly of T-H-Faujasite sheets with 3-fold symmetry (corresponding to a triangular face in a cuboctahedron; the interconnected sheets were dislodged by sonicating T-H-Faujasite in ethanol. c) Structural model showing defect formation when the EMT domains on (111) and (11$\bar{1}$) meet, because EMT cannot coherently bond at 70.5°.

The branching process repeats itself in all four $<111>_{cubic}$ directions (Fig. 2-7d), leading to the hierarchical open house-of-cards arrangement with a well-defined interpenetration angle of 70.5°. Sheet 1 in Fig. 2-19a slowly grows perpendicular to its plane because sheet 2 deprives it of nutrients as the latter extends along its plane and develops as a sheet. This allows the structure to branch and grow in a skeletal morphology before the voids are filled at long synthesis times and an octahedral morphology develops (Fig. 2-22).

If EMT domains, which nucleated on two different neighboring {111} faces [e.g., (111) and (11$\bar{1}$)] meet, a defect will form, because EMT cannot coherently bond at 70.5° (Fig. 2-19c). Such a highly disrupted structure with a large number of defects has also been reported for ZSM-20 prepared using tetraethylammonium cation, which also grows as interpenetrating plates,[103] but with less branching than observed for T-H-Faujasite.

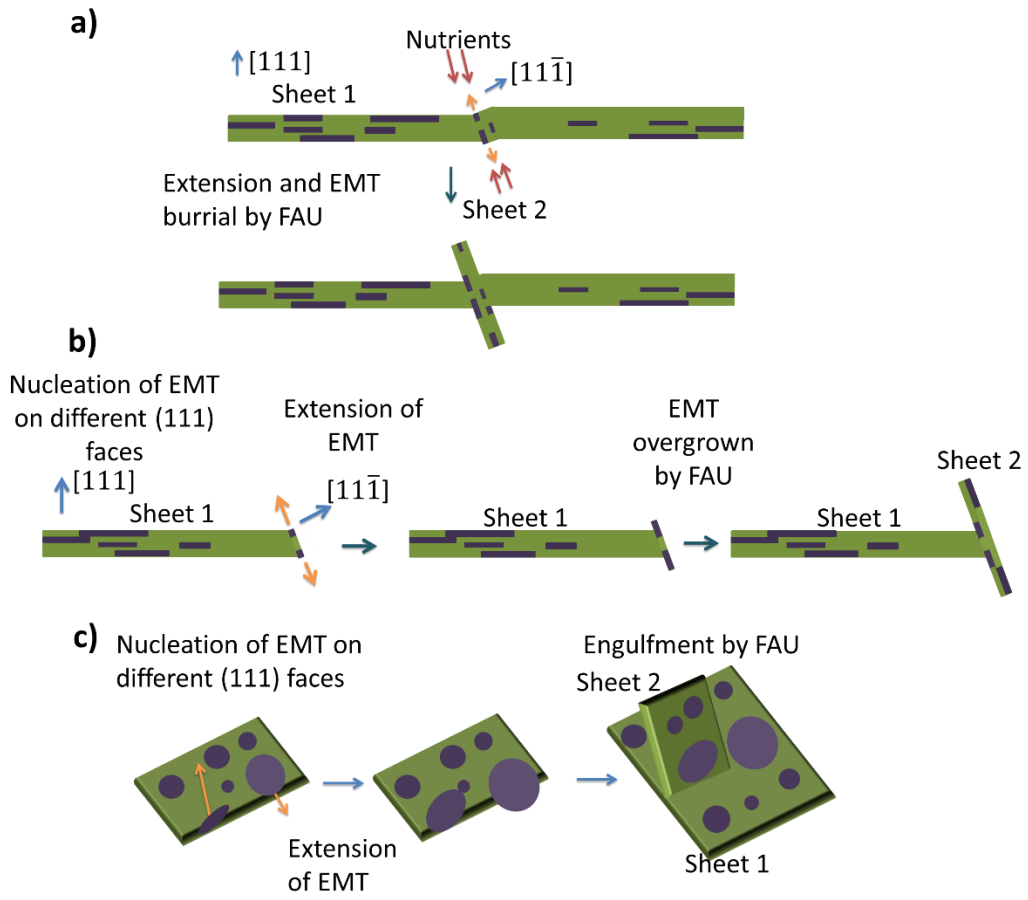

Figure 2-20: Illustration of the branching mechanism in T-H-Faujasite. Nucleation of EMT close to the edge on (11$\bar{1}$) allows the FAU/EMT intergrowth region on (11$\bar{1}$) to extend along its plane and develop as sheet 2 upon thickening. a) If sheet 1 continues to grow along the (111) plane after EMT nucleation on (11$\bar{1}$), sheet interpenetration results. b) In other cases, termination of sheet 1 lateral growth can happen. c) EMT can also nucleate close to the edge on a small region of (11$\bar{1}$) of sheet 1. This region develops as sheet 2, while other regions with EMT nucleation on (111) of sheet 1 still extend along the plane of sheet 1. In this case, sheet 2 can appear as if it interpenetrates sheet 1 throughout its plane dimensions.

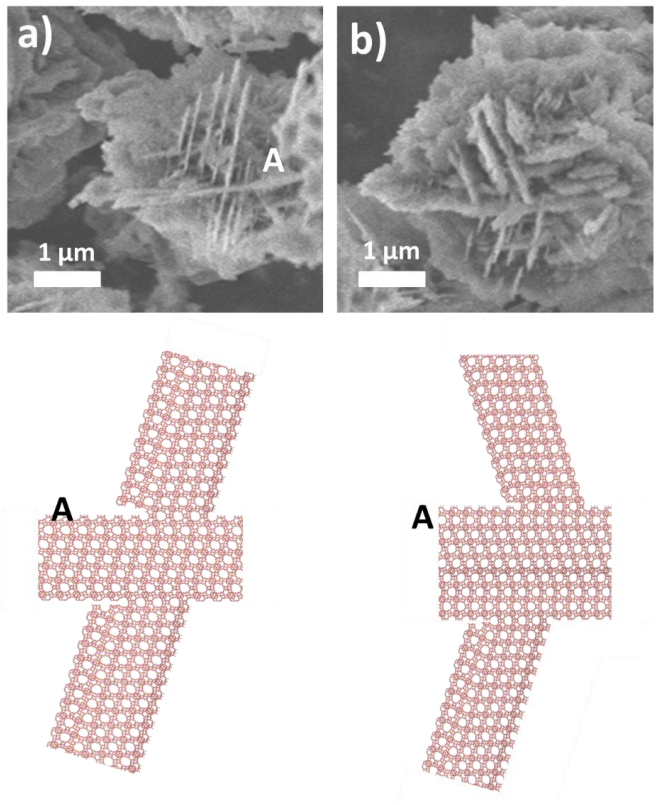

Figure 2-21: Two options for sheet interpenetration depending on the number of faults in sheet A, a) even or b) odd.

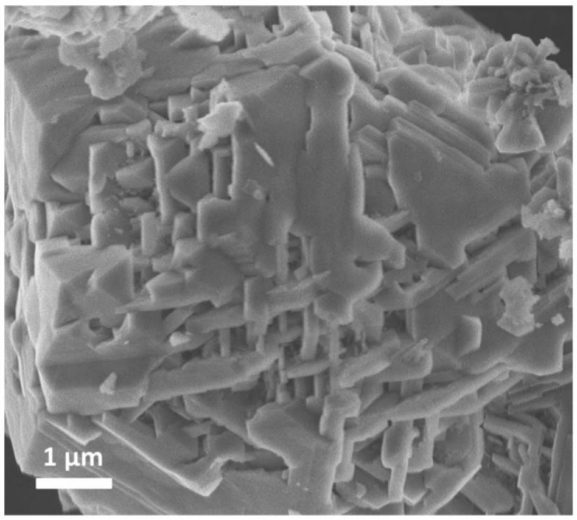

Figure 2-22: SEM image of T-H-Faujasite after 6 days synthesis at 75 °C showing void filling of open structure with time.

According to the model, the connection between the sheets is FAU, which is cubic and can coherently connect at angles of 70.5°. Our proposed conceptual growth model suggests that the random nucleation of small EMT islands, which are not detectable by XRD, on all {111} faces and under growth conditions far from equilibrium, which are characterized by a delicate interplay between surface nucleation, step propagation, and branching, lead to the repetitively branched morphology. This type of dendritic growth is analogous, yet distinct, to that observed in more common crystals including snowflakes. The latter, for example, form a hexagonal lattice that cannot coherently bond at 70.5° and so they branch only in-plane, thereby forming thin hexagonal plates at suitable conditions (Fig. 2-23b).[122] Such branching, along the intrinsic directions of fast growth, occurs when the growth is fast in the beginning, but then switches to faceting when supersaturation drops, developing hexagonal plates.[122] T-H-Faujasite appears to follow the same growth principle (Fig. 2-23a), but since it is predominantly cubic, it can branch in four directions due to the growth instability introduced by EMT.

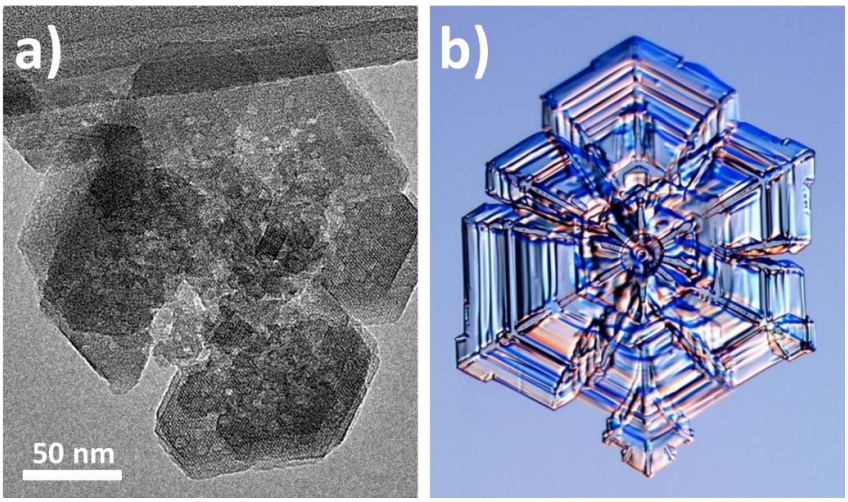

Figure 2-23: a) Low-magnification TEM image of a mesoporous Faujasite sheet dislodged by sonicating T-H-Faujasite in ethanol. b) Snowflake (reprinted with permission from reference [123]). Copyright 2006 by Kenneth Libbrecht.

This model for intergrowth is conceptually different from the model that was developed for the self-pillared pentasil (SPP) which is made of single-unit-cell nanosheets of MFI intergrown orthogonally to each other.[43] Although both models are based on polytypism, it was hypothesized for SPP that lower symmetry MFI sheets grow epitaxially from a

higher symmetry MEL node that acts as a 4-fold symmetric connector, whereas in the case of T-H-Faujasite, the EMT islands intergrow with FAU to break up the cubic symmetry within a nanosheet (the connection between the nanosheets is attributed to FAU, i.e. EMT does not act as a connector). EMT not only directs the formation of anisotropic nanosheets but also creates the growth instability leading to branching. According to the proposed model, hierarchical Faujasite consisting exclusively of single unit sheets cannot be made by this branching mechanism, because branching requires a certain thickness of FAU to be achieved first and rare EMT nucleation to take place at its edges.

2.4 Conclusions

This, and the earlier work on MFI/MEL,[43] demonstrate that there is a direct link between the polytypes involved and the repetitive branching mechanism leading to the hierarchical structures. Once understood, this mechanism will set the stage of what is achievable in terms of characteristic diffusion length, mesopore size, and other characteristics. Similar investigations on other documented intergrowths (e.g. CHA/SOD[124] and ETS-10/ETS-4[125]) are desirable to establish possible branching mechanisms leading to hierarchical materials.

Confirming this work, recently Inayat et al. reported similar house-of-card Faujasite from inorganic syntheses by adding simple inorganic salts, such as zinc nitrate and lithium carbonate.[76] For some of their materials, EMT was present in amounts significant enough to show up in XRD. In the absence of the organic, mesoporosity arises from voids between the sheets.

ACKNOWLEDGEMENTS

The STEM-EDX experiments shown in Fig. 2-16 were performed by Dr. Andrew J. Wagner and the AFM experiments were performed by Neel Rangnekar.

Chapter 3

Combining Pre- and Post-nucleation Trajectories for the Synthesis of High FAU-content Faujasite Nano-crystals from Organic-Free Sols

3.1 Introduction

In chapter 2 we discussed rotational intergrowth as an attractive and promising route to creating hierarchical Faujasite. Another approach is the synthesis of nano-sized crystals. The synthesis of zeolite nano-crystals (smaller than 500 nm) remains an active area of research given certain desirable characteristics that smaller zeolite crystals hold in comparison to their micrometer counterparts. These include substantial changes in the surface properties of the nano-crystals (i.e., increase in external surface area and its contribution to catalytic activity) and reduction in diffusion path length, which positively impacts their performance in adsorption applications and in catalytic and separation processes hindered by diffusion limitations.[43,49,51,126,127] Moreover, the packing of nano-sized crystals give rise to inter-crystalline voids. Nano-zeolites may also find use in the fabrication of zeolite films and membranes,[8,128–134] the fabrication of hierarchical macrostructures, the preparation of functionalized materials and as seeds for zeolite syntheses.[51,126] Several emerging applications of nano-zeolites may also be positively impacted by the availability of pure and precisely sized and shaped zeolite nano-crystals. These include chemical sensing,[17–19] optoelectronics,[20,135] and medicine.[21–25] Moreover, optically clear and colloidally stable nano-zeolite systems can be model systems to develop understanding of zeolite nucleation and growth (chapter 4).[136]

Reports are available for the synthesis of nano-zeolites both from hydrogel (SOD, LTA, FAU and EMT structures) and clear sol (FAU, MFI, MEL, SOD, GIS, LTA, BEA, AEI and CHA structures) mixtures.[51,126] Most of the syntheses from clear precursor mixtures use organic additives, mainly tetraalkyl ammonium cations or amines. The organic additive is believed to play a role in altering supersaturation and hence nucleation and in sterically stabilizing the precursor nano-particles resulting in stable colloidal suspensions of discrete zeolite nano-crystals with narrow particle size distributions. However, this

approach has several drawbacks, namely the low yield compared to micrometer sized crystals and the usage of large amounts of expensive and non-recyclable organic, the removal of which can lead to irreversible aggregation of the nano-crystals.[137,138] This hinders the scale-up and increases production costs. Therefore, nano-zeolite synthesis from all-inorganic mixtures is desirable. Other methods of synthesizing nano-zeolites include the use of seeding, microwave or sonication heating, confined synthesis and growth inhibition using organosilanes.[51,126,139,140]

As an important component of fluid catalytic cracking (FCC) catalysts, Faujasite is one of the most widely used zeolites.[105] FAU and EMT can crystallize from the same synthesis mixtures,[141] and they can exist in the same crystal with the FAU and EMT components either segregated non-randomly into adjoining blocks or intimately intergrown together.[100] FAU and EMT have different pore connectivity resulting from the different arrangement of the Periodic Building Unit (section 2.1.2). This will affect their bulk properties and intergrowth materials might potentially be better catalysts than pure FAU or EMT. Therefore, both crystal size and FAU/EMT content affect the catalytic properties of Faujasites. For example, reducing FAU crystal size from 0.65 μm to 0.06 μm improved selectivity to intermediate products like gasoline in cracking of gas oil and the improvement was attributed to enhanced diffusion,[142] while FAU/EMT performed better than pure FAU and pure EMT (synthesized using crown ether) in FCC gasoline hydro-upgrading where they exhibited a good balance between hydrodesurfurization efficiency and Octane Number preservation.[92] Therefore, future studies should focus on the correlation of catalytic activity with structural disorder and intergrowth in nano-crystals, which implies that control of FAU/EMT content in conjunction with controlling particle size and shape is desirable. Interpenetration of nano-crystals can create mesoporosity between the crystals improving performance in catalytic applications hindered by diffusion limitations. On the other hand, discrete Faujasite nano-crystals can be used for the fabrication of zeolite films and membranes.

Most synthesis recipes of FAU/EMT intergrowth materials utilize organics or cations other than sodium and most reports on the synthesis of colloidal nano-FAU use excess

tetramethylammonium cations.[100,105] However, there are also reports on the synthesis of Faujasite nano-crystals in the absence of organics from highly alkaline gel mixtures[143–145] and by seeding.[146,147] Earlier work reported the synthesis of Faujasite nano-crystals from inorganic aluminosilicate sol mixed at 0 °C.[146] Davis reported the synthesis of VPI-6, FAU/EMT intergrowth, from an inorganic synthesis gel.[106] Recently, Awala et al. reported the synthesis of colloidally stable nano-sized Faujasite with enhanced FAU content from such all-inorganic aluminosilicate sols.[138]

In this work, we investigated the effect of synthesis conditions on FAU content, crystal size, and crystal interpenetration in Faujasite particles made from inorganic sols with the aim of maximizing the FAU content in discrete nano-crystals. Comparison of experimental X-ray diffraction patterns with simulated patterns using DIFFaX was used to give an overall indication of the extent of intergrowth while high resolution transmission electron microscopy imaging was used for localized views of intergrowths and faulting. Evidence is provided that all the samples made in this work contain FAU/EMT intergrowths. By investigating composition ranges (1.8-33) SiO_2: 1 Al_2O_3: (2.7-33) Na_2O: (41-1000) H_2O, Faujasite nano-crystals with FAU contents between 0.6-0.8 were synthesized. The increase in FAU content is accompanied by an increase in crystal size (>100 nm). The higher FAU purity can be extended to nano-crystals only by using a specific combination of pre- and post-nucleation trajectories which include first mixing the sol at high water content compositions that favor nanocrystal formation and then - after a certain time - lowering by freeze-drying the water to levels favoring the formation of FAU.

3.2 Experimental Methods

3.2.1 Synthesis

FAU can be synthesized from inorganic aluminosilicate gel containing only Na^+ ions. However, such syntheses yield aluminum rich Faujasite (Si/Al close to 1-zeolite X) which is highly hydrophilic and can be used as basic catalyst,[98,99] ion exchanger,[148] or as selective adsorbent.[149] The proton form of zeolite X is unstable and cannot be used as an

acid catalyst. The preparation of high-silica (type Y, SiO_2 /Al_2O_3=4.9) Faujasite by D. W. Breck in the late 1950's established synthetic Faujasite as an acid catalyst.[150] The increase in Si/Al ratio gives it high thermal stability in the acid form to be used for petroleum processes[151] and biomass-related catalytic processes.[52] Later efforts have only raised SiO_2 /Al_2O_3 to about 6 by hydrothermal synthesis. Increasing Si/Al by hydrothermal synthesis is not possible without adding seeds (nucleation centers) because the synthesis composition needed has a low pH (to reduce the silica solubility) that drastically decreases the crystallization rate. The effect of pH on zeolite Si/Al ratio has been well-established.[152] SiO_2 /Al_2O_3 approaching 10 can be achieved by adding crown ether to the synthesis gel.[101] Other additives used include cesium ions,[153] bis-(2-hydroxyethyl)-dimethylammonium ions,[154] and replacing part of the sodium aluminate with aluminum salt such as aluminum sulfate, chloride, and nitrate.[155] Increasing Si/Al ratio beyond this has been achieved by post-synthetic modifications including steaming and acid leaching,[156] treatment with silicon tetrachloride,[157] and treatment with ethylenediamine-tetraacetic acid.[158]

EMT can be synthesized by adding 18-crown-6 to the aluminosilicate gel.[101] Mintova et al. reported the synthesis of ultrasmall (6-15 nm) EMT crystals from inorganic aluminosilicate sols at low temperature (30°C).[159]

An attempt to control FAU/EMT intergrowth in micron-sized crystals was reported by using a mixture of 18-crown-6 and 15-crown-5 in different proportions.[105] In this work we attempt to control FAU/EMT intergrowth in nano-crystals from inorganic sols. The small differences between the lattice energies of FAU and EMT zeolites suggest that kinetic factors play a major role in nucleation. Thus, it is critical to control the nucleation kinetics in order to obtain a desired intergrowth.

The synthesis mixtures used in this work were inorganic sodium aluminosilicates, i.e., X SiO_2: Y Al_2O_3: Z Na_2O: ZZ H_2O. Molar composition was varied in attempts to find conditions that give optically clear mixtures and crystallize nano-crystals with high FAU content (favor crystal nucleation over crystal growth).

Chemicals used were reagent grade sodium silicate solution (10.6% Na_2O, 26.5% SiO_2, 62.9% H_2O, Sigma Aldrich), LUDOX® HS-40 colloidal silica (Sigma Aldrich), LUDOX® HS-30 colloidal silica (Sigma Aldrich), anhydrous technical sodium aluminate (Sigma Aldrich), aluminum (foil, thickness 0.05 mm, 99.8% trace metals basis, Sigma Aldrich), NaOH (Mallinckrodt) and deionized water.

In a typical synthesis using sodium silicate solution and anhydrous sodium aluminate, two solutions were prepared. Solution A was prepared by dissolving NaOH pellets in 65 wt% of the total amount of deionized water needed and then added to sodium silicate solution. Solution B was prepared by dissolving sodium aluminate in the remaining amount of deionized water. Solutions A and B were kept in ice water bath for 1 h and then solution B was added dropwise into solution A in a teflon bottle (kept in ice bath) while stirring. The synthesis system was kept mixing in ice bath for 1 h and then aged for 24 h at room temperature before heating in an oil bath. Synthesis temperatures studied include room temperature, 40, 50, 60, 80 and 120 °C. The crystals were then washed by repeated centrifugation and re-dispersion until the pH dropped to 8-9. They were then dried at 70 °C overnight.

In syntheses using LUDOX® HS, adding sodium hydroxide solution to LUDOX resulted in a gel, which became a clear sol after heating at 90 °C. In syntheses using Al foil, the foil was cut into small pieces and slowly added into NaOH solution in water to dissolve (note: the reaction is exothermic and produces hydrogen). The amount of NaOH solution added in solutions A and B was also varied for different syntheses. Specifics of certain experiments are mentioned with the results.

According to the procedure of reference 138, a set of experiments were performed involving freeze-drying of freshly prepared or aged sols followed by hydrothermal treatment at 50 °C. Freeze-drying was performed using Labconco FreeZone 4.5 Liter Benchtop Freeze Dry System. If needed, the water content was adjusted after freeze-drying by adding a certain amount of water.

Hydrothermal microwave synthesis was carried out using microwave Teflon liners (EasyPrep Temperature Control Vessel Assembly, CEM Corporation) placed in a MARS (microwave accelerated reaction system) model unit (CEM Corporation, 2450 MHz).

3.2.2 Material Characterization

Samples for conventional Transmission Electron Microscopy (TEM) studies were prepared by applying a few drops of a zeolite suspension in ethanol or water onto a copper grid coated with ultrathin Carbon (<3nm) on Carbon Holey support film (Ted Pella Inc.) and leaving it to dry at room temperature. TEM imaging was performed on FEI Tecnai G2 F30 TEM operating at 300 kV. The microscope has a twin-pole piece with a point-to point resolution of 0.24 nm. All TEM images were captured using a CCD camera.

Scanning Electron Microscopy (SEM) images of uncoated samples on carbon tape were collected using a JEOL JSM-6700F scanning microscope operated at 3 kV.

Argon adsorption (87.3 K) was performed using a commercially available automatic manometric sorption analyzer (Quantachrome Instruments AutosorbiQ MP). Prior to adsorption measurements, the samples were outgassed at 573 K for 16 h under turbomolecular pump vacuum.

Following the procedure in reference 74, Inductively Coupled Plasma - Optical Emission Spectrometry (ICP-OES) analysis was done on a Thermo Scientific iCAP 6500 duo optical emission spectrometer fitted with a simultaneous charge induction detector.

X-ray Diffraction (XRD) measurements reported were performed either in-house or at Beamline 17-BM at Advanced Photon Source, Argonne National Laboratory. For the latter, sample powder was loaded in 0.8-1 mm diameter Kapton® capillaries. The wavelength used was 0.72768 Å. 2-D diffraction data were collected in transmission geometry by a PerkinElmer® amorphous silicon flat panel detector, and were subsequently processed with program GSAS II to obtain conventional XRD plots of

Intensity vs. 2θ. The in-house PANalytical X'Pert PRO MPD X-ray diffractometer is equipped with Co source (wavelength of 1.7890 Å) and operated at 45 kV and 40 mA. All XRD patterns presented in this work are converted to correspond to wavelength 1.7890 Å.

3.2.3 X-ray Diffraction Pattern Fitting

To estimate the FAU contents of samples, powder XRD patterns were simulated using the DIFFaX program of Treacy et al.[160] 0.72768 Å wavelength was used. Instrumental broadening was simulated as the Gaussian function, with full-width half maximum set to 0.05° (obtained using a standard Lanthanum hexaboride). A constant value of full-width half maximum is adequate given the 2θ range considered in this work. All XRD patterns presented in this work are converted to correspond to wavelength 1.7890 Å. The structural parameters of a Faujasite layer were set as a=b=17.585 Å, c=14.358 Å and γ= 120°. The Si^{+4} and O^{-2} coordinates were used from the example files provided with the DIFFaX program. The layer width, number of stacked layers, and transition probabilities were varied depending on the sample.

Fits to experimental XRD patterns of samples composed of nano-crystals with different faulting probabilities and crystal sizes (discussed in section 3.3.1), were simulated assuming the existence of two populations in a physical mixture: a population of pure FAU crystals and a "representative" population of FAU/EMT crystals. The recursive option in DIFFaX could not be used to fit experimental XRD patterns of nano-crystals with random stacking of very few Faujasite sheets in FAU/EMT crystals. In such cases, fits were obtained by using explicitly defined stacking sequences of Faujasite sheets described in terms of stacking of sheets of FAU cages ('F') and EMT cages ('E'). Size constraints were imposed based on evidence regarding size of pure FAU and FAU/EMT crystals obtained from TEM images. It should be noted that this methodology is not statistically rigorous and other combinations of pure FAU and sets of FAU/EMT intergrowths may give equally good fits of the XRD data. Best fits to experimental XRD patterns were made by inspection focusing on 2θ range 5-15°. Simulations were done for

distinct experimental patterns. However, it should be noted that the similar appearance of some XRD patterns can be partly attributed to size broadening such that minor differences (if present) would be impossible to detect.

Pure silica zeolites were used for the simulations, whereas synthesized samples are aluminum rich as evidenced by Si/Al obtained by ICP-OES (Table 3-2). This might be one of the factors contributing to some of the discrepancies in peak relative intensities between experimental and simulated XRD patterns. Other factors include faulting in several <111> directions which results in small embedded domains and is not accounted for in DIFFaX, defects arising when the Faujasite sheets stack differently in different parts of a crystal (Fig. 3-9e), interpenetration of crystallites and variation of lattice constants between nano-crystals with different FAU/EMT contents.

Two independent probabilities (α_{FF} – the probability that a sheet of FAU cages is followed by another sheet of FAU cages- and α_{EE} – the probability that a sheet of EMT cages is followed by another sheet of EMT cages) are needed to model intergrowth clustering in FAU/EMT materials based on the assumption that only the nearest-neighbor layer interactions are important.[100,160] The fraction of FAU sheets in a crystal is given by,

$$\frac{1-\alpha_{\mathrm{EE}}}{2-\alpha_{\mathrm{EE}}-\alpha_{\mathrm{FF}}},$$

The stacking probability values for a crystal can be calculated by tracking the sideways shifts in the sheet stacking from TEM $[1\bar{1}0]_{cubic}$ view using,

$$\alpha_{\mathrm{EE}} \approx \frac{n_{\mathrm{EE}}}{N_{\mathrm{E}}}, \quad \alpha_{\mathrm{FF}} \approx \frac{n_{\mathrm{FF}}}{N_{\mathrm{F}}},$$

where n_{EE} and n_{FF} are the total numbers of EMT-EMT and FAU-FAU stackings, respectively, and N_E and N_F are the total numbers of EMT and FAU sheets, respectively.[100] It should be noted that stacking probability values calculated from crystals with finite numbers of stacked Faujasite sheets might not be accurate. In such cases, the fraction of FAU sheets is calculated by counting the number of FAU sheets in a

crystal and dividing this by the total number of FAU and EMT sheets. The stacking probability values are still given as an indication of the nature of FAU/EMT intergrowth in crystals (large values of α_{FF} and α_{EE} signify FAU and EMT components segregated non-randomly into contiguous blocks while small values of α_{FF} and α_{EE} signify FAU and EMT intimately intergrown together).[100]

3.3 Results and Discussion

3.3.1 FAU/EMT Intergrowth

Faujasite has been typically reported to crystallize in micron sizes from gel systems.[150] Starting from molar composition 3.6 SiO_2: 1 Al_2O_3: 4.3 Na_2O: 214 H_2O,[161] it was attempted to find compositions that would crystallize nano-FAU from optically clear mixtures. Earlier efforts starting from reference 146 investigated composition range (4.5-12) SiO_2: (0.7-1.3) Al_2O_3: (9-15) Na_2O: 214 H_2O and identified clear starting sols.[162] In this work, composition range (1.8-33) SiO_2: 1 Al_2O_3: (2.7-33) Na_2O: (41-1000) H_2O was investigated.

Using high resolution TEM and XRD simulations (DIFFaX), a description of the degree of faulting and FAU/EMT intergrowths in the samples is given. Conclusions from TEM can be biased towards the faulting patterns in thin, electron-beam-transparent crystallites, while XRD patterns provide representative fingerprints of the bulk specimen. However, TEM is especially needed for characterizing nano-crystals because of the XRD peak broadening that might hide important faulting/intergrowth features. TEM is also needed to obtain crystal size information to reduce the number of parameters required to fit experimental XRD patterns. This is required because, as it will be discussed, crystals with different faulting probabilities and different sizes coexist in the same sample.

Ternary diagrams (SiO_2- Al_2O_3- Na_2O) are used to present the starting mixture compositions explored in this work. Fig. 3-1a shows the compositions for H_2O / Al_2O_3=214 conventionally heated at 60 °C (silica source: sodium silicate solution, aluminum source: anhydrous sodium aluminate). Samples in this ternary diagram are

representative and will be the focus of the discussion. Ternary diagrams for H_2O / Al_2O_3 =300 and 150 can be found in Fig. 3-2 and 3-3, respectively. All samples crystallized from these compositions are FAU/EMT intergrowths with varying crystal/particle sizes and morphologies (crystal anisotropy and degree of crystal interpenetration).

At Si/Al= 1.8 (**A** 3.6 SiO_2:1 Al_2O_3:4.3 Na_2O:214 H_2O, **B** 3.6 SiO_2:1 Al_2O_3:4.7 Na_2O:214 H_2O, **C** 3.6 SiO_2:1 Al_2O_3:4.9 Na_2O:214 H_2O, **D** 3.6 SiO_2:1 Al_2O_3:5.2 Na_2O:214 H_2O, **E** 3.6 SiO_2:1 Al_2O_3:5.6 Na_2O:214 H_2O, **F** 3.6 SiO_2:1 Al_2O_3:7.3 Na_2O:214 H_2O) increasing the amount of Na_2O increases the viscosity upon adding solution B to solution A (for a description of solutions A and B see section 3.2.1) and shortens the crystallization time. For all mixtures, the gel breaks into a suspension upon stirring. Fig. 3-1b shows the morphological changes upon increasing Na_2O; the higher the Na_2O content, the smaller the individual crystallite size, but clusters of crystals (group of crystallites with no clear evidence of intergrowing together) form. Initially, the size and shape of the particles can be described as micron sized distorted octahedra which change to intergrown sheets (the size of the latter decreases as Na_2O increases) and eventually to clusters of crystallites. As shown in Fig. 3-1c, the XRD patterns from samples A, E and F exhibit increased broadening as the amount of Na_2O increases due to the decrease in crystal size. This broadening however, can also be partly attributed to the faulting in the Faujasite structure, which is evident by the emergence of a shoulder peak, at around 6.7°, resulting from faulting/non-extended EMT domains (Fig. 3-1c trace E). The extension of EMT domains is a relative term and depends on the size of FAU domains (for a representative set of DIFFaX simulations see Fig. 3-4). The appearance of plate morphology also confirms Faujasite faulting since this morphology is not consistent with FAU-only materials.

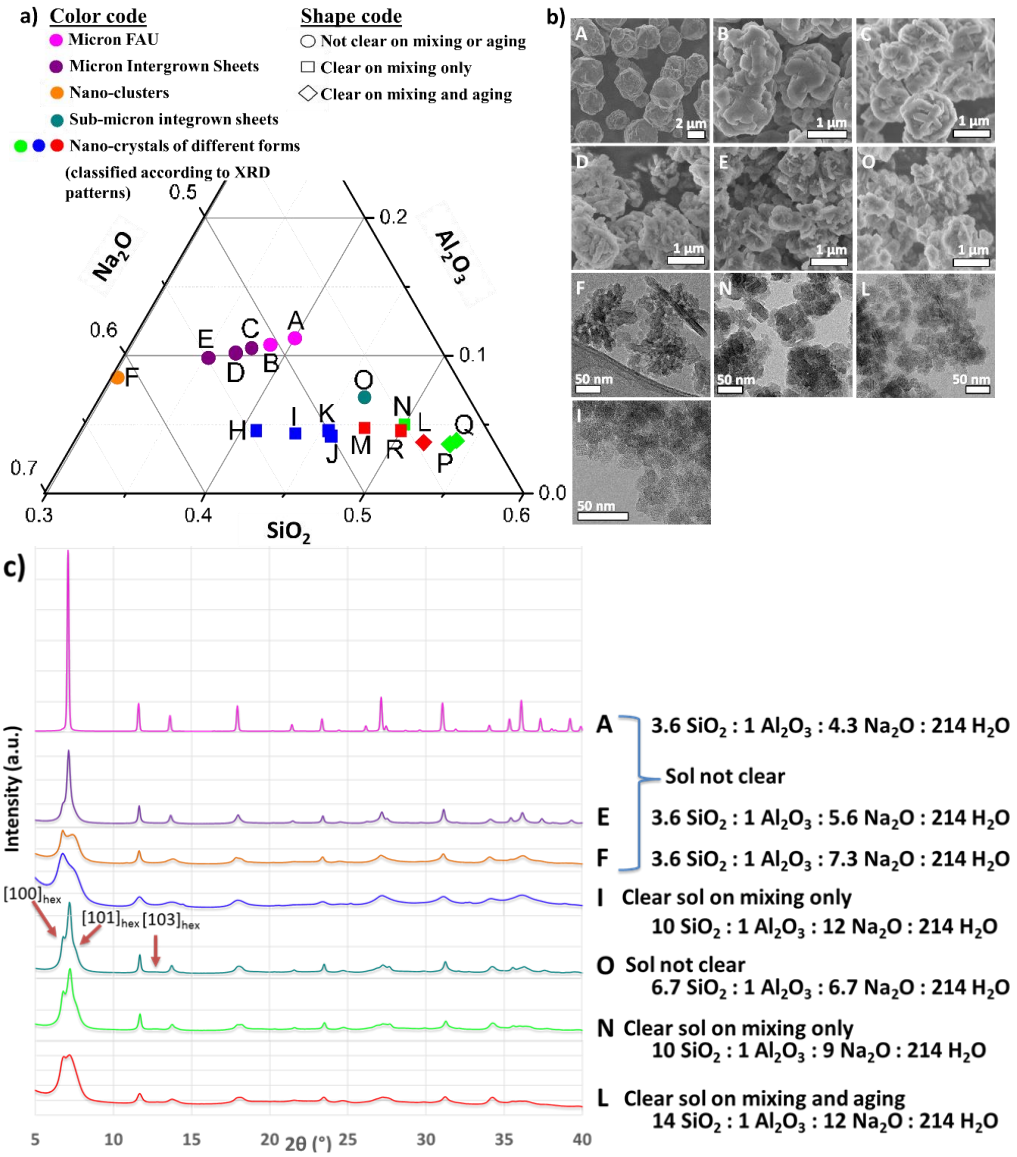

Figure 3-1: (a) Ternary diagram (SiO_2- Al_2O_3- Na_2O) for mixtures with H_2O / Al_2O_3=214 conventionally heated at 60 °C (silica source: sodium silicate solution, aluminum source: anhydrous sodium aluminate). The color and shape codes of the ternary diagram highlight the variation in crystal morphology and the optical clarity of the mixtures at start and after aging. Mixture compositions that crystallize nano-crystals are classified according to their XRD patterns, i.e. nano-crystals that have similar XRD patterns are presented with the same color code. Compositions marked A, E, I, N and L are representative of their respective categories. (b) SEM (A, B, C, D, E and O) and TEM (F, N, L and I) images (with inset labels corresponding to samples in the ternary diagram (a)) showing the morphological variation of Faujasite crystals with synthesis mixture composition. Samples A and B are micron sized distorted octahedra. Particles in samples C, D, E and O consist of intergrown sheets. TEM images show nano-sized Faujasite (F: nano-clusters, N: nano-intergrown sheets, L and I: nano-crystals). (c) XRD patterns (showing the effect of synthesis mixture composition on crystallite size and faulting signified by peak broadening and the appearance of shoulder peaks) representative of the samples in the ternary diagram in (a). The EMT [100], [101] and [103] peaks are marked. XRD measurements were performed at Beamline 17-BM at Advanced Photon Source, Argonne National Laboratory. Starting mixture compositions are shown next to the XRD traces. Detailed discussion of XRD patterns and morphology is provided in the text.

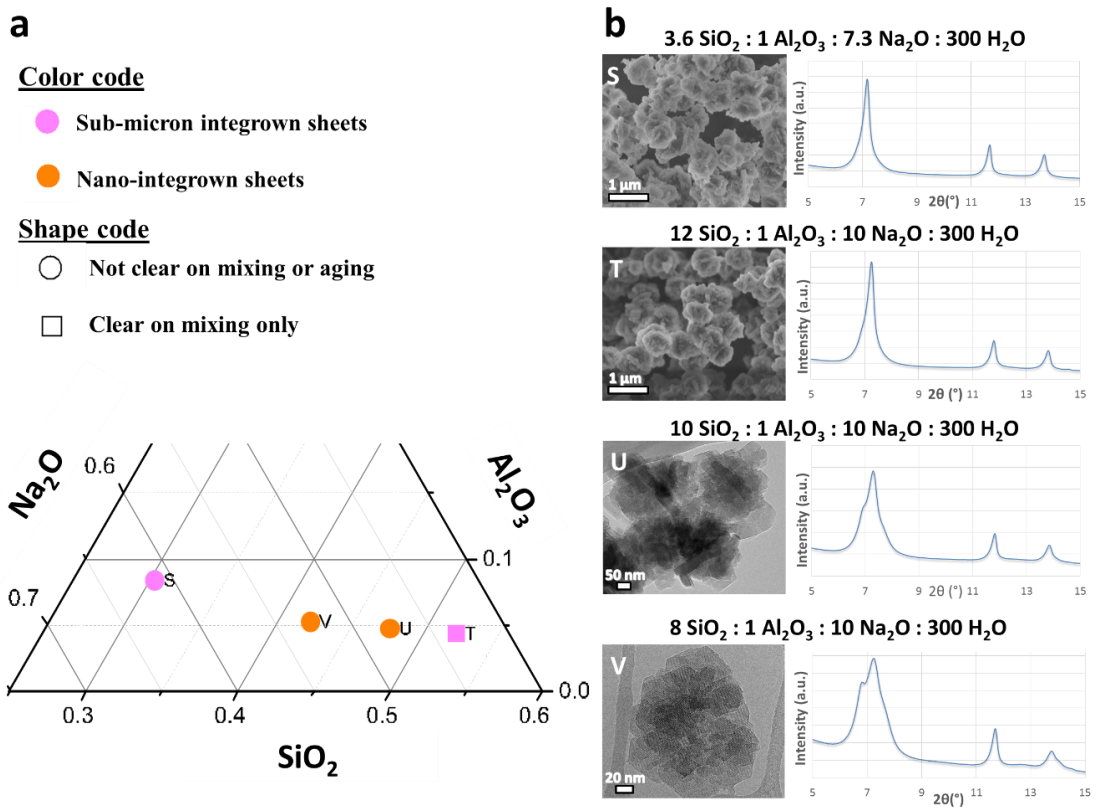

Figure 3-2: (a) Ternary diagram (SiO_2- Al_2O_3- Na_2O) for mixtures with H_2O / Al_2O_3=300 conventionally heated at 60 °C (silica source: sodium silicate solution, aluminum source: anhydrous sodium aluminate). The ternary diagram highlights the clarity of the systems at start and after aging, and the variation in crystal morphology. (b) SEM (S, T) and TEM (U, V) images (with inset labels corresponding to samples in the ternary diagram (a)) indicating the morphological changes of Faujasite crystals with synthesis mixture composition. Samples S and T are sub-micron intergrown sheets and samples U and V are nano-sized intergrown sheets. Corresponding XRD patterns (indicating the effect of composition on crystallite size and faulting signified by peak broadening and the appearance of shoulder peaks) are shown next to the TEM/SEM images. XRD measurements were performed in-house.

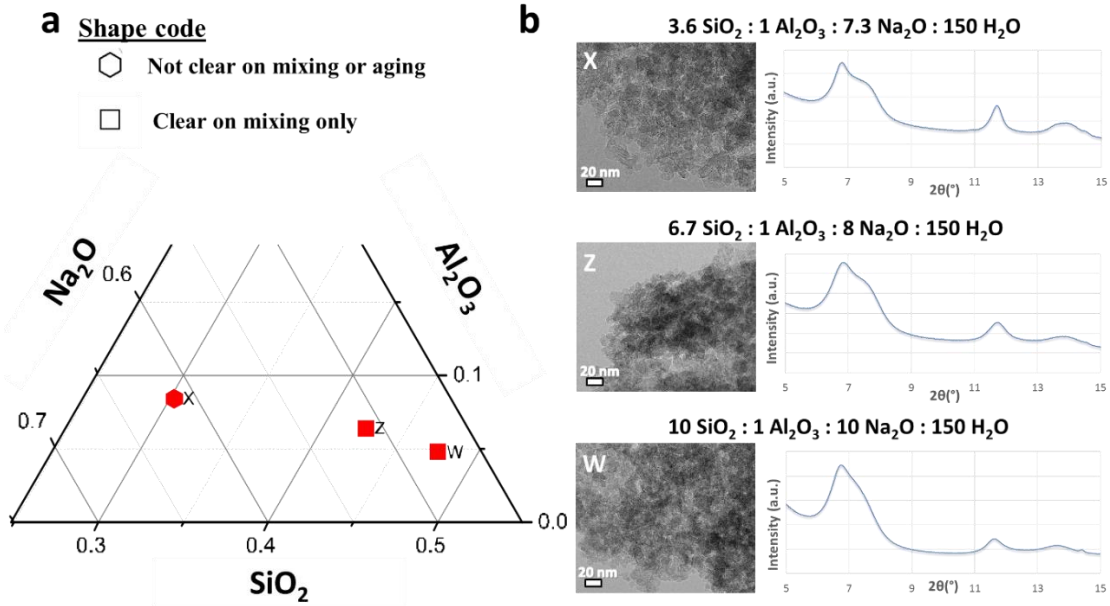

Figure 3-3: (a) Ternary diagram (SiO_2- Al_2O_3- Na_2O) for mixtures with H_2O / Al_2O_3=150 conventionally heated at 60 °C (silica source: sodium silicate solution, aluminum source: anhydrous sodium aluminate). The ternary diagram highlights the clarity of the systems at start and after aging. (b) TEM images (with inset labels corresponding to samples in the ternary diagram (a)) showing that samples W, X, and Z are all nano-crystals. Corresponding XRD patterns are shown next to the TEM images. XRD measurements were performed in-house for all samples except W for which XRD was performed at Beamline 17-BM at Advanced Photon Source, Argonne National Laboratory.

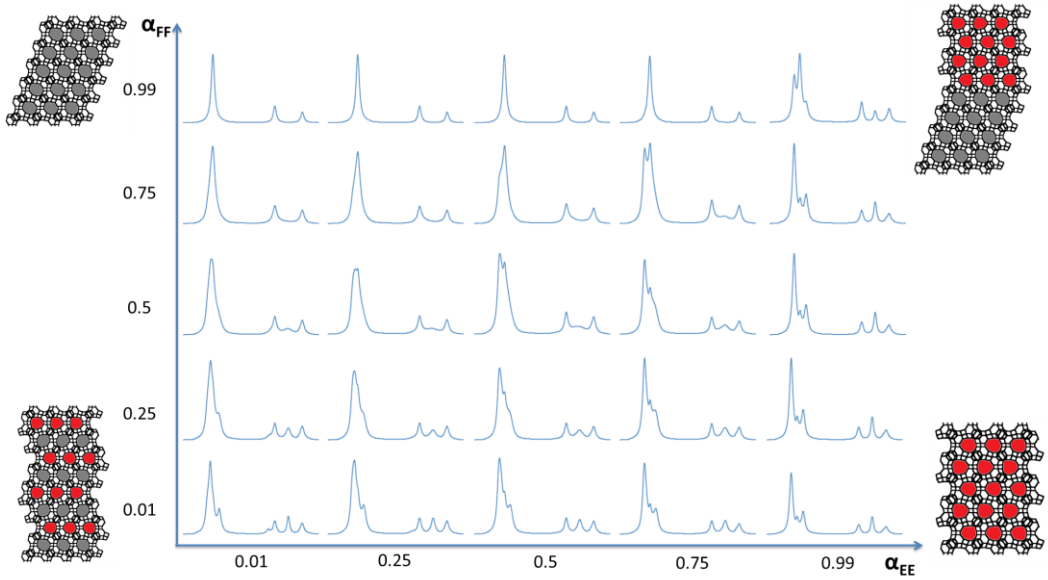

Figure 3-4: FAU/EMT faulting map (2θ scale 5-15°, λ=1.7890 Å) simulated recursively (for a statistical ensemble of crystallites, each with a distinct stacking sequence, but weighted by the probability that such a sequence will occur) for 50 nm crystals with 50 stackings. Structures that satisfy $\alpha_{FF} + \alpha_{EE} = 1$ show random, uncorrelated faulting. As α_{FF} and α_{EE} approach 1, FAU and EMT sheets cluster together whereas as they approach 0, FAU and EMT sheets alternate. In the schematics, FAU and EMT sheets are highlighted gray and red, respectively.

The XRD pattern (Fig. 3-1c trace F) for a sol with composition 3.6 SiO_2: 1 Al_2O_3: 7.3 Na_2O: 214 H_2O (marked F in Fig. 3-1a) clearly shows anisotropic broadening where the FAU [111]/EMT [002] and FAU [311] peaks are broadened more compared to the EMT [100] and FAU [220]/EMT [110] peaks. Using information from TEM (Fig. 3-5), the anisotropic broadening arises from ~30-50 nm FAU crystals (Fig. 3-5I) and anisotropic plate-like faulted crystals (Fig. 3-5II). The faulted crystals can be as large as around 150 nm laterally with only 10 Faujasite sheets in thickness (Fig. 3-1b- F). The laterally big FAU and EMT domains explain the sharp EMT [100] and FAU [220]/EMT [110] peaks. A similar XRD pattern was reported by Inayat et al. for the Lithium house-of-card Faujasite.[76] As the amount of Li in their synthesis increases, the interpenetrating sheets become thinner and give XRD pattern similar to the one reported for sample F. This confirms our earlier suggestion (chapter 2) that the creation of hierarchical Faujasite, the thickness of the sheets and the openness of its structure are determined by the frequency of faulting.[74]

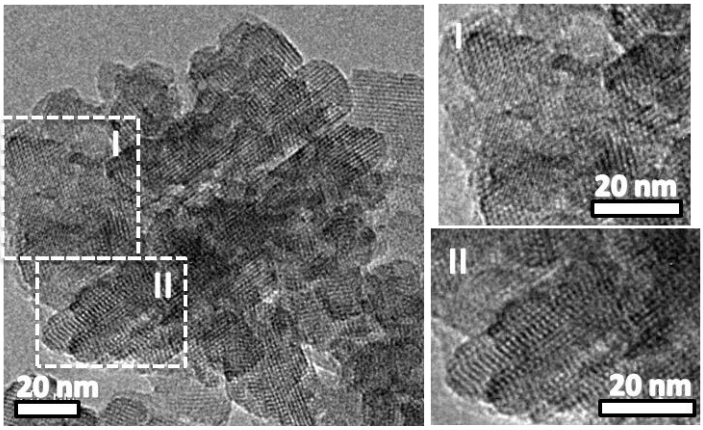

Figure 3-5: TEM image for sample F (3.6 SiO_2: 1 Al_2O_3: 7.3 Na_2O: 214 H_2O, see Fig. 3-1) showing the presence of pure FAU (inset I) and faulted crystals (inset II) in nano-clusters.

Mixtures with compositions **H** (9 SiO_2: 1 Al_2O_3: 12 Na_2O: 214 H_2O), **I** (10 SiO_2: 1 Al_2O_3: 12 Na_2O: 214 H_2O), **J** (11 SiO_2: 1 Al_2O_3: 12 Na_2O: 214 H_2O) and **K** (10 SiO_2: 1 Al_2O_3: 11 Na_2O: 214 H_2O) in the ternary diagram of Fig. 3-1a crystallize nano-crystals that appear from TEM to be physical mixtures of FAU/EMT crystals and FAU crystals (Fig. 3-6). For Na_2O/Al_2O_3= 12, changing SiO_2/Al_2O_3 from 6 to 11 does not make a noticeable difference in the samples (according to XRD patterns). A representative XRD

pattern for such samples is shown in Fig. 3-1c for sample I. This XRD pattern is very similar to that of sample F, except that the peaks are broader. This is due to the smaller sizes of crystals. The drop in the FAU [111] intensity is a result of the smaller sizes of FAU domains in FAU/EMT crystals (this is also attributed to by the decrease in crystal size). Both the pure FAU and FAU/EMT crystals are of comparable sizes in these samples. Crystals are typically between 15-40 nm and FAU/EMT crystals have around 8-15 Faujasite sheets.

The FAU/EMT nano-crystals do not exhibit a uniform faulting probability, i.e. each crystal has its own probability (corresponding to its distinct nucleation and growth trajectory) that is not representative of the entire sample. The stacking probability values of two FAU/EMT crystals were measured by tracing the sideways shifts in the sheet stacking from the $[1\bar{1}0]_{cubic}$ views (Fig. 3-6 (b, e) and (c, f)). These crystals are rich in EMT and have FAU fractions lower than 0.5. The variation of faulting content among crystals is a result of the finite number of Faujasite sheets in each nano-crystal, such that a single crystal cannot represent the whole sample. This non-homogeneity of the crystals makes it difficult to simulate similar patterns by DIFFaX and the approach taken here for quantitative estimation of FAU content is described in section 3.2.3. It should be noted that repeated experiments show XRD patterns with no detectable differences by inspection, which indicates that the samples are statistically identical and have reproducible FAU/EMT content.

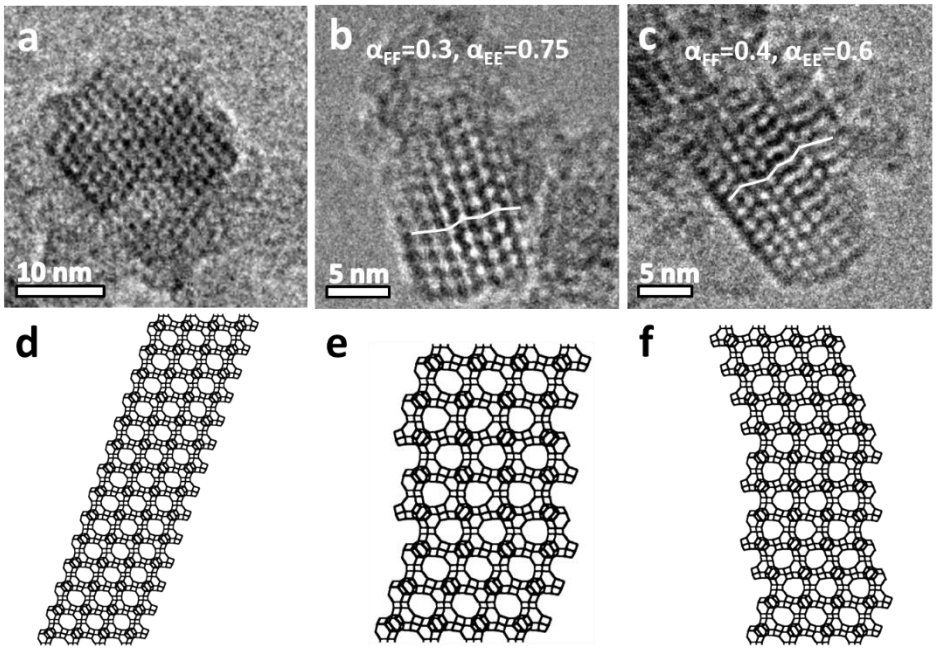

Figure 3-6: TEM images for crystals from sample I (10 SiO_2: 1 Al_2O_3: 12 Na_2O: 214 H_2O, see Fig. 3-1) showing $[1\bar{1}0]_{cubic}$ views of (a) FAU nano-crystal, (b) FAU/EMT nano-crystal with faulting probability α_{FF}=0.3, α_{EE}=0.75 and FAU fraction of 0.43 (stacking sequence of Faujasite sheets is traced) and (c) FAU/EMT nano-crystal with faulting probability α_{FF}=0.4, α_{EE}=0.6 and FAU fraction of 0.5 (stacking sequence of Faujasite sheets is traced). (d, e and f) Representations of the Faujasite sheet stacking for a, b and c, respectively.

XRD patterns, like trace I of Fig. 3-1c, should be interpreted using information from TEM. Otherwise, by only fitting XRD patterns, FAU/EMT materials can be misinterpreted as having hexagonal crystal structure, i.e., EMT phase only. This is due to the distortion of FAU domains in FAU/EMT materials resulting from the slight mismatch between FAU and EMT in-plane cell dimensions (e.g. CSZ-1[163]) affecting the overall symmetry of such materials. Even in the absence of TEM evidence, it should be pointed here that the XRD pattern of Fig. 3-1c trace I cannot be interpreted as indicative of pure EMT. This is supported by the absence of the $[103]_{hex}$ peak in the XRD patterns. In this respect, earlier interpretations of similar patterns in the literature should be revisited.

Mixtures with compositions **L** (14 SiO_2: 1 Al_2O_3: 12 Na_2O: 214 H_2O), **M** (10 SiO_2: 1 Al_2O_3: 10 Na_2O: 214 H_2O), **N** (10 SiO_2: 1 Al_2O_3: 9 Na_2O: 214 H_2O), **O** (6.7 SiO_2: 1 Al_2O_3: 6.7 Na_2O: 214 H_2O), **P** (15 SiO_2: 1 Al_2O_3: 12 Na_2O: 214 H_2O), **Q** (14 SiO_2: 1 Al_2O_3: 11 Na_2O: 214 H_2O) and **R** (11 SiO_2: 1 Al_2O_3: 10 Na_2O: 214 H_2O) in the ternary

diagram of Fig. 3-1a favor the crystallization of extended regions of EMT with FAU. This is evident from the XRD patterns in Fig. 3-1c and their comparison with the FAU/EMT faulting map in Fig. 3-4 (traces L, N, O are representative of their categories). The presence of EMT is also evident by the peak de-convolution presented in Fig. 3-7, which shows that the FAU [111]/EMT [002] peak is accompanied by two shoulder peaks corresponding to the EMT [100] and [101] peaks. Moreover, a broad and faint EMT [103] peak appears at around 13°. At high Si/Al ratio (Si/Al=7), a clear sol results from mixing silicate and aluminate solutions, that remains clear after 24 h aging at room temperature (Fig. 3-1a).

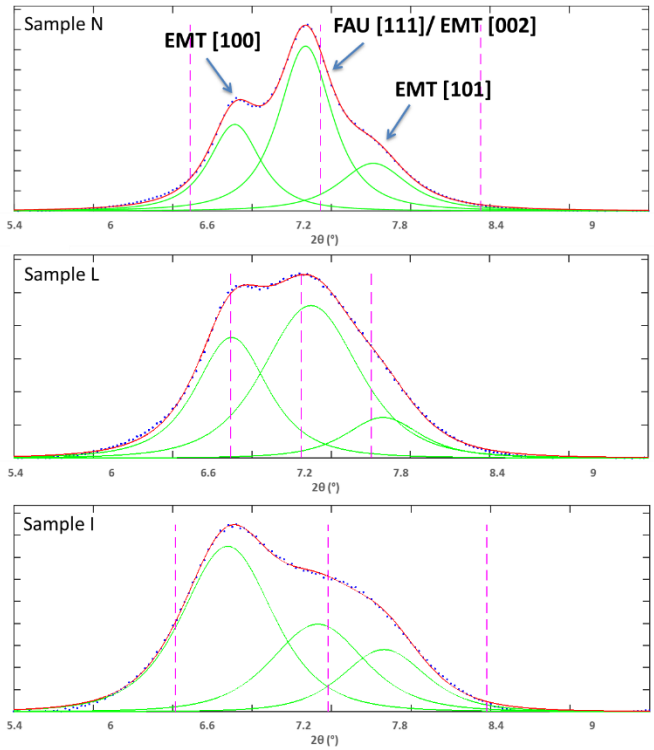

Figure 3-7: Peak de-convolution for samples N, L and I (Fig. 3-1a) in 2θ range 5.4°-9.3°showing that FAU [111]/EMT [002] peak develops 2 shoulder peaks from EMT phase, the EMT [100] and [101] peaks. Peaks were de-convoluted using the freely available Interactive Peak Fitter (Version 11) matlab function written by Professor Emeritus Tom O'Haver (University of Maryland at College Park). The code uses an unconstrained non-linear optimization algorithm to decompose a complex, overlapping-peak signal into its component parts. The Pearson peak shape was used. Shape parameter is used to fine-tune the peak shape, where a value of 1.0 gives a Lorentzian shape, a value of 2.0 gives a shape roughly half-way between a Lorentzian and a Gaussian, and larger values give a nearly Gaussian shape. The background was subtracted using a linear baseline interpolated from the edges of the data segment (assuming that the peak returns to the baseline at the edges of the signal). The least-square fitting was iterated 100 times.

From Fig. 3-1a, sols with compositions O and N crystallize sub-micron sized and nano-sized particles with intergrown sheets, respectively (Fig. 3-1b- O and N). The interpenetration of sheets results from faulting in several $< 111 >_{cubic}$ directions (Fig. 3-8a). On the other hand, sample L shows negligible interpenetration of sheets (Fig. 3-8b). Samples O and N show increase in relative FAU [111] intensity from XRD that arises from bigger FAU domains indicating that FAU favors sheet interpenetration. Fig. 3-8a shows segregation of FAU (Inset I) and EMT (Inset II) domains in FAU/EMT particle from sample N. Intimate intergrowths of the two structures also exist. This supports the earlier observation by Treacy et al. that ZSM-20 which showed crystallites intergrowing at angles of 70°, has FAU and EMT components segregated non-randomly into contiguous blocks.[100]

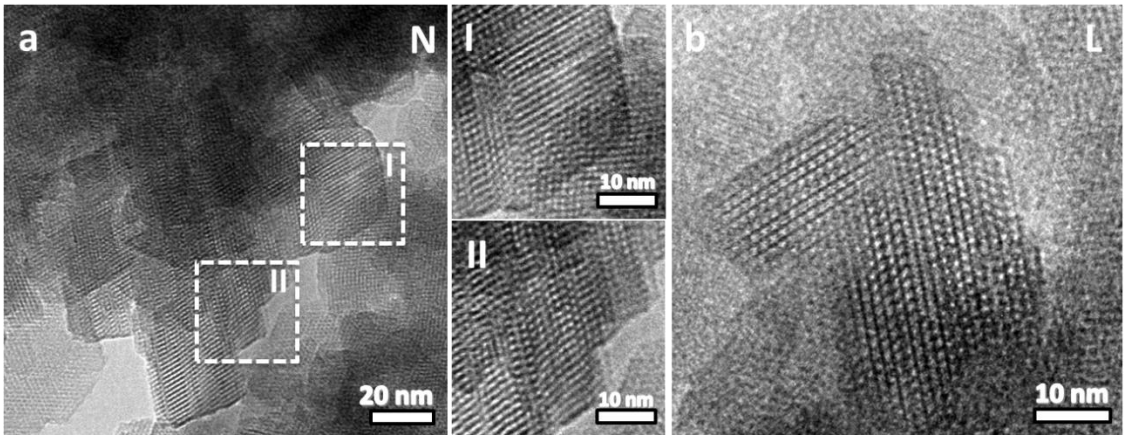

Figure 3-8: TEM images of samples N and L in Fig. 3-1a: (a) sample N showing nano-particle with intergrown sheets resulting from faulting in several $< 111 >_{cubic}$ directions (insets I and II show segregated FAU and FAU/EMT domains, respectively), and (b) sample L showing nano-particle with less pronounced intergrowth of sheets.

A sol with composition 14 SiO_2: 1 Al_2O_3: 12 Na_2O: 214 H_2O (marked L in Fig. 3-1a) crystallizes physical mixtures of nano-crystals with numerous faulting probabilities. Examples of crystallites with different faulting probabilities are shown in Fig. 3-9. Fig. 3-9a and b show a FAU nano-crystal and a predominantly FAU nano-crystal faulting in multiple $< 111 >_{cubic}$ directions, respectively. Fig. 3-9d and f show the stacking of Faujasite sheets for crystals in Fig. 3-9c and e, respectively. The crystal of Fig. 3-9d contains segregated FAU and EMT domains (α_{FF}=0.67, α_{EE}=0.83), while the one in Fig. 3-9f shows random stacking of Faujasite sheets (α_{FF}=0.33, α_{EE}=0.29). As mentioned

previously, the stacking in each nano-crystal does not represent the sample as a whole due to the limited number of Faujasite sheets in each crystal. It can also be noticed that the crystal in Fig. 3-9e shows different stacking sequences in different parts of the crystal leading to defects (marked in the Figure with a circle) that may be due to multiple nucleation events on the same (111) plane. As described in section 3.2.3, this non-homogeneity was taken into account for the estimation of FAU content, which for sample L indicates FAU fraction of 0.64 (Table 3-1 presented in section 3.3.3 gives FAU contents for samples discussed in this work).

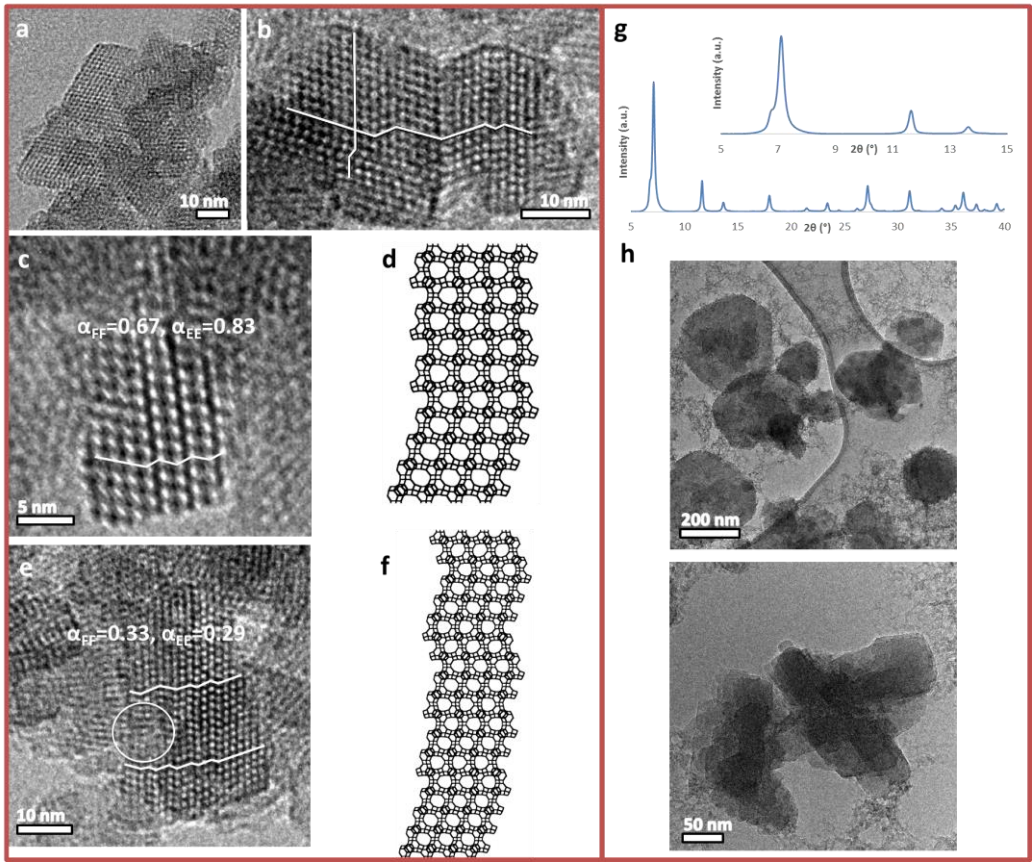

Figure 3-9: Effect of water content for mixture composition 14 SiO_2: 1 Al_2O_3: 12 Na_2O: X H_2O on particle size and FAU/EMT intergrowths. TEM images of sample L (X=214, Fig. 3-1a) aligned along the $[1\bar{1}0]_{cubic}$ views showing (a) FAU nano-crystal, (b) nano-crystal faulting in multiple $< 111 >_{cubic}$ directions, (c) nano-crystal with extended FAU and EMT domains described by probabilities α_{FF}=0.67, α_{EE}=0.83 (stacking sequence of Faujasite sheets is traced) and (e) nano-crystal with random stacking of Faujasite sheets described by probabilities α_{FF}=0.33, α_{EE}=0.29 (stacking sequence of Faujasite sheets traced). Defect from multiple nucleation events on the same (111) plane is marked by circle in 'e'. (d, f) Representations of the Faujasite sheet stacking for 'c' and 'e', respectively. (g) XRD pattern and (h) TEM images showing increase in FAU content and particle size up to ~300 nm for X=106 conventionally heated at 50 °C (silica source: LUDOX® HS-40, aluminum source: Al foil). XRD measurement was performed at Beamline 17-BM at Advanced Photon Source, Argonne National Laboratory.

Motivated by earlier reports on its role,[164–166] the effect of the water amount on FAU/EMT content was investigated. A sol with the lowest amount of water achievable (using LUDOX® HS-40 and Al foil) that remains clear after 24h aging at ambient temperature, has composition 14 SiO_2: 1 Al_2O_3: 12 Na_2O: 106 H_2O. It results in improved FAU content but the particle size increases to ~80-300 nm (Fig. 3-9h). These crystals have less extended EMT domains compared to FAU domains (α_{FF} =0.85, α_{EE}=0.4 in Fig. 3-4).

We have also attempted the synthesis using the composition reported for 10 nm zeolite Y (14.3 SiO_2: 1 Al_2O_3: 12.9 Na_2O: 228.6 H_2O)[138] but the result was similar to sample L with composition 14 SiO_2: 1 Al_2O_3: 12 Na_2O: 214 H_2O.

In an attempt to reduce the EMT content in the nano-crystals, critical synthesis parameters were screened to study their effect on FAU/EMT intergrowth for composition 14 SiO_2: 1 Al_2O_3: 12 Na_2O: 214 H_2O. These variations included crystallization temperature and time, stirring during heating and/or aging, aging time, mixing temperature and sources of aluminum and silicon. None of these parameters under the conditions studied here were found to eliminate the presence of EMT.

For composition 14 SiO_2: 1 Al_2O_3: 12 Na_2O: 214 H_2O, mixing silicate and aluminate solutions and aging at room temperature increase the crystal size. Moreover, the former affects the clarity of the system, where mixing at 0 °C helps obtain a clear system by decreasing the non-controlled polymerization of aluminosilicate species resulting in small amorphous precursor particles. Aging time was also found to affect only the particle size (crystals can nucleate without room temperature aging at this composition).

The effect of the synthesis temperature on the nucleation kinetics of FAU/EMT was investigated. Temperatures of 40, 60, 80 and 120 °C were studied for composition 14 SiO_2: 1 Al_2O_3: 12 Na_2O: 214 H_2O (marked L in Fig. 3-1a for 60°C). Fig. 3-10 shows XRD and TEM data. De-convolution of the peaks between 2θ= 5.4°-9.3° shows the presence of EMT reflections in all samples. As the synthesis temperature increases, the

crystal size also increases. TEM images show that pure FAU and FAU/EMT crystals are detected for all synthesis temperatures studied. Following the samples over different heating periods did not show any effect on the FAU/EMT content of the samples, instead, dense phase zeolite P forms on prolonged heating.

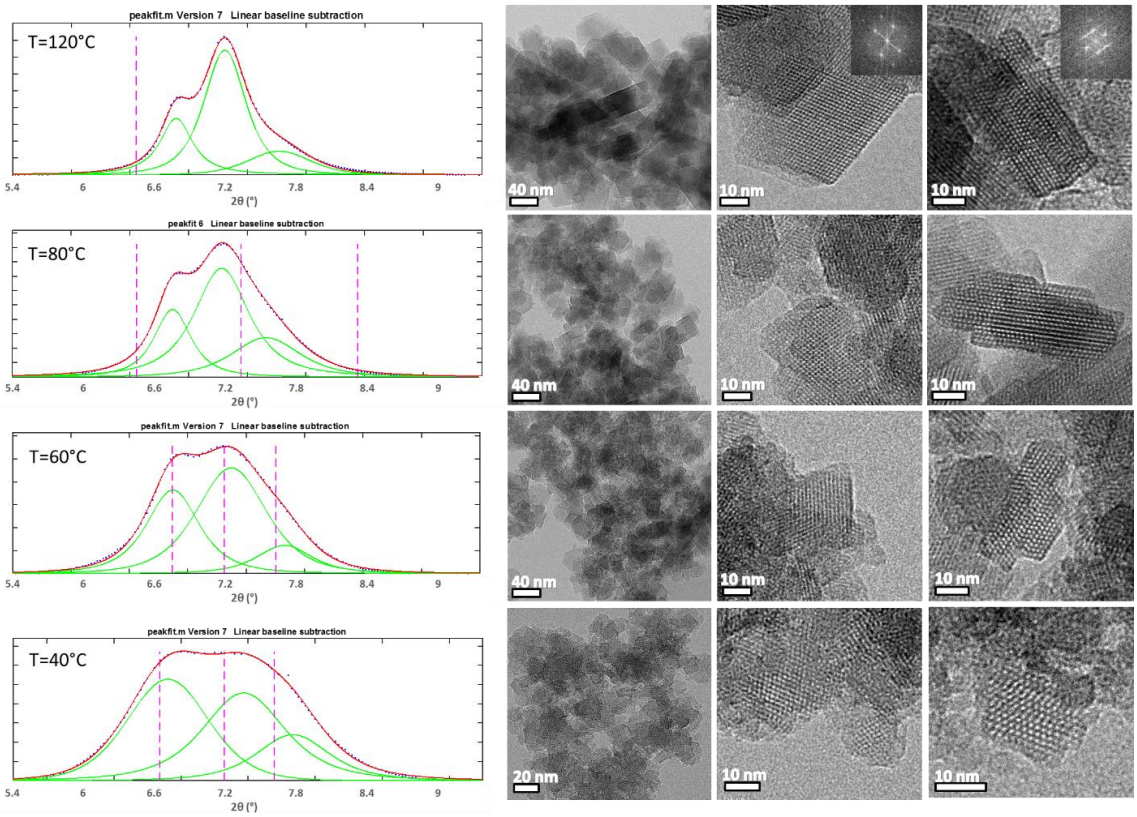

Figure 3-10: De-convoluted XRD peaks (2θ= 5.4°-9.3°) show the presence of EMT reflections in all samples synthesized at different temperatures (inset) for composition 14 SiO_2:1 Al_2O_3:12 Na_2O:214 H_2O. XRD was performed at Beamline 17-BM at Advanced Photon Source, Argonne National Laboratory. As the synthesis temperature increases, the crystal size also increases. TEM images (presented next to their corresponding XRD patterns) show the change in crystal size with temperature and the presence of pure FAU and FAU/EMT crystals for all synthesis temperatures studied. Peaks were de-convoluted as stated in the caption of Fig. 3-7.

Sources of aluminum and silicon are known to affect the crystallization of zeolites. Several combinations of reactant sources were tried (e.g sodium aluminate and LUDOX® HS-30 or HS-40, Al foil and LUDOX® HS-30 or HS-40, and Al foil and sodium silicate), but all yielded FAU/EMT intergrowth materials for composition 14 SiO_2: 1 Al_2O_3: 12 Na_2O: 214 H_2O (marked L in Fig. 3-1a for sodium silicate and sodium aluminate), i.e. the source had no effect under the conditions used in this work (not shown). Replacing sodium aluminate with Al foil helps achieve a clear aluminosilicate

precursor solution and results in smaller particles, but the EMT occurrence cannot be eliminated. The split ratio of the total NaOH and H_2O amount between the silicate and aluminate sols was also investigated but the latter also had no noticeable effect on FAU/EMT intergrowth. Even though the latter affects the clarity of the system on mixing aluminate and silicate sols, all systems turn clear after 1 day aging at room temperature (even if they were not clear initially). Small Angle X-ray Scattering from these mixtures shows that increasing the amount of NaOH added to the silicate solution results in smaller nano-particles initially, but eventually precursor nano-particles in all systems aggregate on aging (chapter 4).

We also studied the effect of microwave heating because it is known that it affects nucleation and growth kinetics and may promote uniformity of the nanocrystals.[167] Conventional heating can result in inhomogeneous heating of the sample due to the relatively long time needed to reach the set temperature. This can lead to local and temporal heterogeneities during crystallization. Microwaves, on the other hand, produce rapid and uniform heating of the precursor suspension and accelerate nucleation resulting in shorter crystallization times compared to conventional heating.[167] Microwave heating was used to crystallize nano-Faujasite from sol with composition 14 SiO_2: 1 Al_2O_3: 12 Na_2O: 214 H_2O marked L in Fig. 3-1a (source of Al: sodium aluminate, source of Si: sodium silicate). A ramp rate of 35 °C/min was used to heat the sol to 60 °C at 400W. A well- crystallized sample was obtained in 2 h (Fig. 3-11a). This is 12 times faster than conventional heating at 60 °C (24 h needed to obtain a well crystallized sample). This reduction in heating time makes microwave heating desirable. However, EMT still nucleates in the system as shown by peak de-convolution in 2θ range 5.4-9.3° (Fig. 3-11b). Ramp rates as low as 2.5 °C/min were also tried, with no significant effect detected. Fig. 3-11c and d show pure FAU and faulted crystals, respectively, from sample heated by microwave radiation.

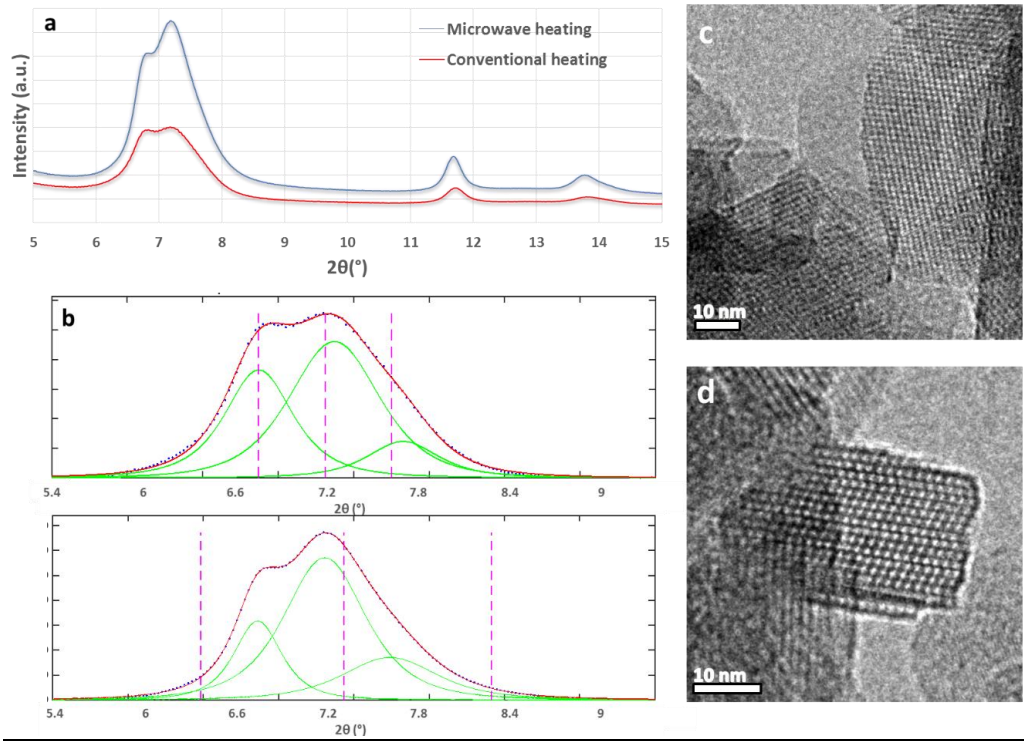

Figure 3-11: (a) XRD patterns for samples crystallized from sols with composition 14 SiO_2: 1 Al_2O_3: 12 Na_2O: 214 H_2O using conventional (marked L in Fig. 3-1a) and microwave heating at 60 °C (source of Al: sodium aluminate, source of Si: sodium silicate). A ramp rate of 35 °C/min was used to heat the sol to 60 °C at 400W. XRD was performed at Beamline 17-BM at Advanced Photon Source, Argonne National Laboratory. (b) EMT detected by peak de-convolution in 2θ range 5.4-9.3°. TEM images of (c) pure FAU and (d) FAU/EMT crystals from sample heated by microwave radiation. Peaks were de-convoluted as stated in the caption of Fig. 3-7.

3.3.2 High FAU Content Nano-crystals

Recalling from Fig. 3-9 that composition 14 SiO_2: 1 Al_2O_3: 12 Na_2O: 214 H_2O (i.e., with a higher water content) results in reduction in crystal size, while composition 14 SiO_2: 1 Al_2O_3: 12 Na_2O: 106 H_2O (i.e., with a lower water content) results in improved FAU purity in large crystals, leads to the hypothesis that *the synthesis of high FAU content nano-crystals would require a combination of trajectories from compositions with different water contents, i.e., 14 SiO_2: 1 Al_2O_3: 12 Na_2O: 214 H_2O and 14 SiO_2: 1 Al_2O_3: 12 Na_2O: 106 H_2O*. One way to combine both trajectories is by using freeze-drying.

Earlier reports indicate that freeze drying can be used to remove water from aluminosilicate mixtures. Jelić et al. showed that freeze drying an aluminosilicate hydrogel (that crystallizes zeolite A) and then adding back the removed water resulted in similar zeolite A crystal size distribution compared to directly subjecting the aluminosilicate hydrogel to hydrothermal conditions without the steps of freeze drying and adding back water. Based on this finding, they suggested that freeze-drying does not substantially change the distribution of nuclei in the amorphous aluminosilicate precursor gel established during precipitation.[168] On the contrary, Awala et al. suggested that freeze drying aluminosilicate sols to remove water after aging, followed by re-adjustment of the water to its initial level before freeze drying, leads to improved sol uniformity that can then lead to improved FAU content in Faujasite nano-crystals.[138,169,170] Motivated by the findings reported in ref. 138 (and 169), we decided to explore the effect of freeze-drying on Faujasite particle size and FAU content. Specifically, the role of water content and the timing (before or after aging) of freeze-drying were investigated.

By mixing the sol at 14 SiO_2: 1 Al_2O_3: 12 Na_2O: 214 H_2O (starting mixture composition of sample L in Fig. 3-1a) and then lowering the water content (14 SiO_2: 1 Al_2O_3: 12 Na_2O: 100 H_2O) after 24h aging at room temperature, nano-particles with improved FAU content can be obtained (Fig. 3-12 - path 1). This result suggests that freeze-drying after aging has a pronounced effect on the trajectory of crystallization. Control experiments (Fig. 3-12 - paths 2-7) further support this hypothesis and underscore the importance of the starting composition and the timing of freeze-drying for composition adjustment. The importance of the starting composition in determining the trajectory of crystallization is confirmed by mixing and aging the sol at 14 SiO_2: 1 Al_2O_3: 12 Na_2O: 106 H_2O and then freeze-drying to reach a final composition of 14 SiO_2: 1 Al_2O_3: 12 Na_2O: 100 H_2O (Fig. 3-12 - path 3). This synthesis path results in ~100-150 nm Faujasite crystals. The importance of timing of freeze-drying is supported by synthesis paths 4 and 5 in Fig. 3-12. Specifically, freeze-drying the sol with composition 14 SiO_2: 1 Al_2O_3: 12 Na_2O: 214 H_2O right after mixing (no aging) and adjusting the composition to 14 SiO_2: 1 Al_2O_3: 12 Na_2O: 100 H_2O (Fig. 3-12 - path 4) results in 100-200 nm crystals. Adding a 24 h room

temperature aging step at 14 SiO_2: 1 Al_2O_3: 12 Na_2O: 100 H_2O after freeze-drying still results in large crystals (Fig. 3-12 - path 5). Freeze-drying the sol and then adjusting the water content to the initial level 14 SiO_2: 1 Al_2O_3: 12 Na_2O: 214 H_2O (Fig. 3-12 - path 2) does not result in nano-crystals of improved FAU content. This shows that the higher FAU purity is only obtained by crystallization at the lower water content. Freeze-drying experiments were also performed for Na_2O/ SiO_2 = 0.89 and 1 (Fig. 3-13 and 3-14) with similar outcomes.

For the synthesis conditions studied here, the point at which freeze-drying is done is critical in determining the crystal size. It is possible that a particular sol structure evolves with aging and it is preserved upon freeze-drying and can affect the trajectory of crystallization leading to high nucleation rate of nanocrystals. On the other hand, sol composition (water content) is the determining factor for FAU content, suggesting that the 24h aged sols and the corresponding particles and aggregates they contain are not yet evolved to a level that can determine the FAU vs. EMT content. To acquire further insight, a TEM/SAXS study was performed on selected sols (chapter 4).

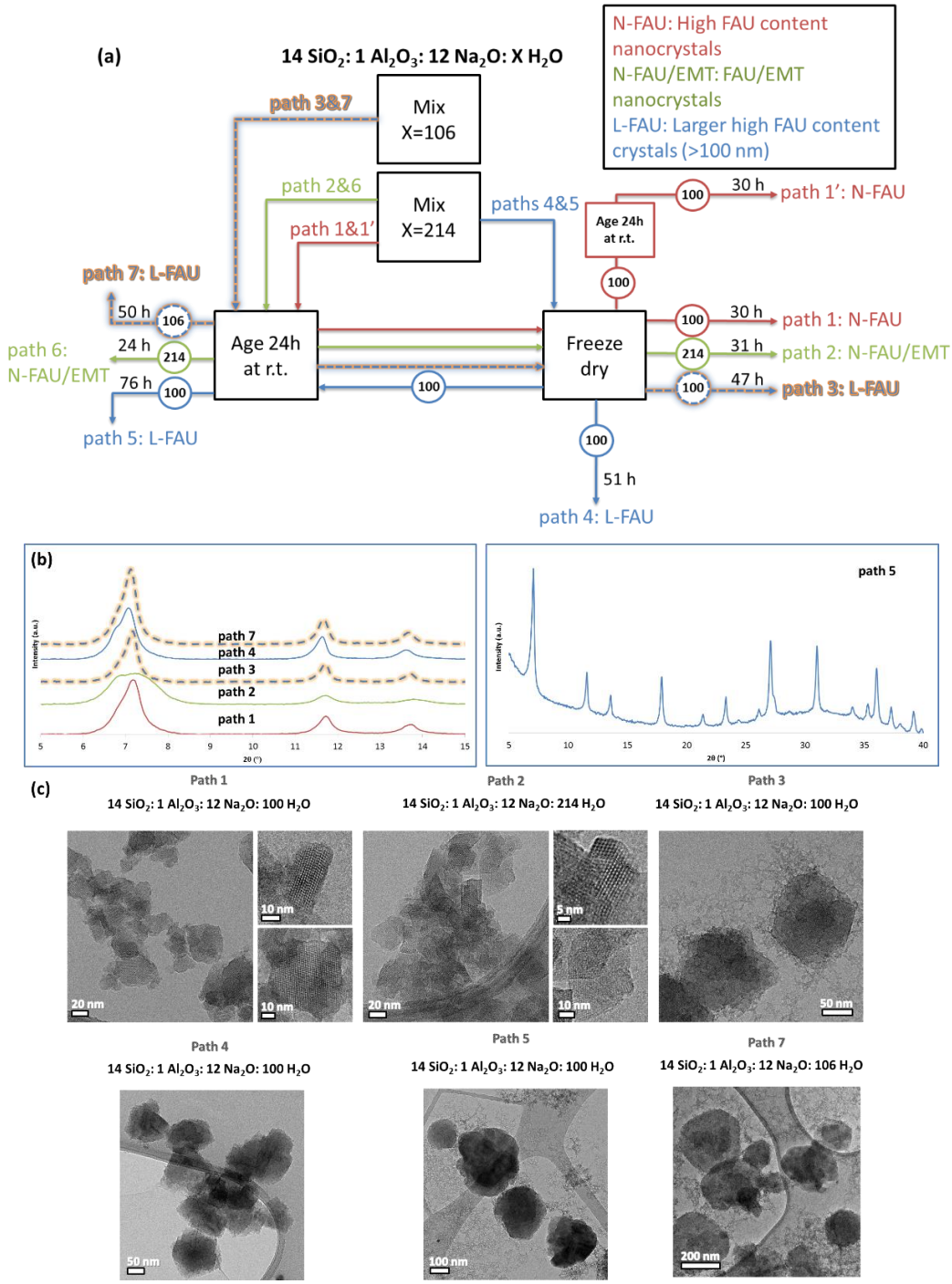

Figure 3-12: (a) Flow chart summarizing synthesis paths for 14 SiO_2: 1 Al_2O_3: 12 Na_2O: X H_2O exploring the effect of the starting composition, final composition, and the timing (before or after 24h room temperature aging) of freeze-drying on Faujasite particle size and FAU/EMT content. Numbers in the circles represent H_2O/ Al_2O_3 ratios. Numbers in hours correspond to heating duration at 50 °C. The path numbers correspond to those mentioned in the text. Path 6 corresponds to sample L in Fig. 3-1a. **N-FAU**: Nano-crystals with improved FAU purity, **L-FAU**: Large crystals (>100 nm) with improved FAU purity, **N-FAU/EMT**: Nano-crystals with large EMT content. (b) XRD patterns (collected in-house) and (c) TEM images.

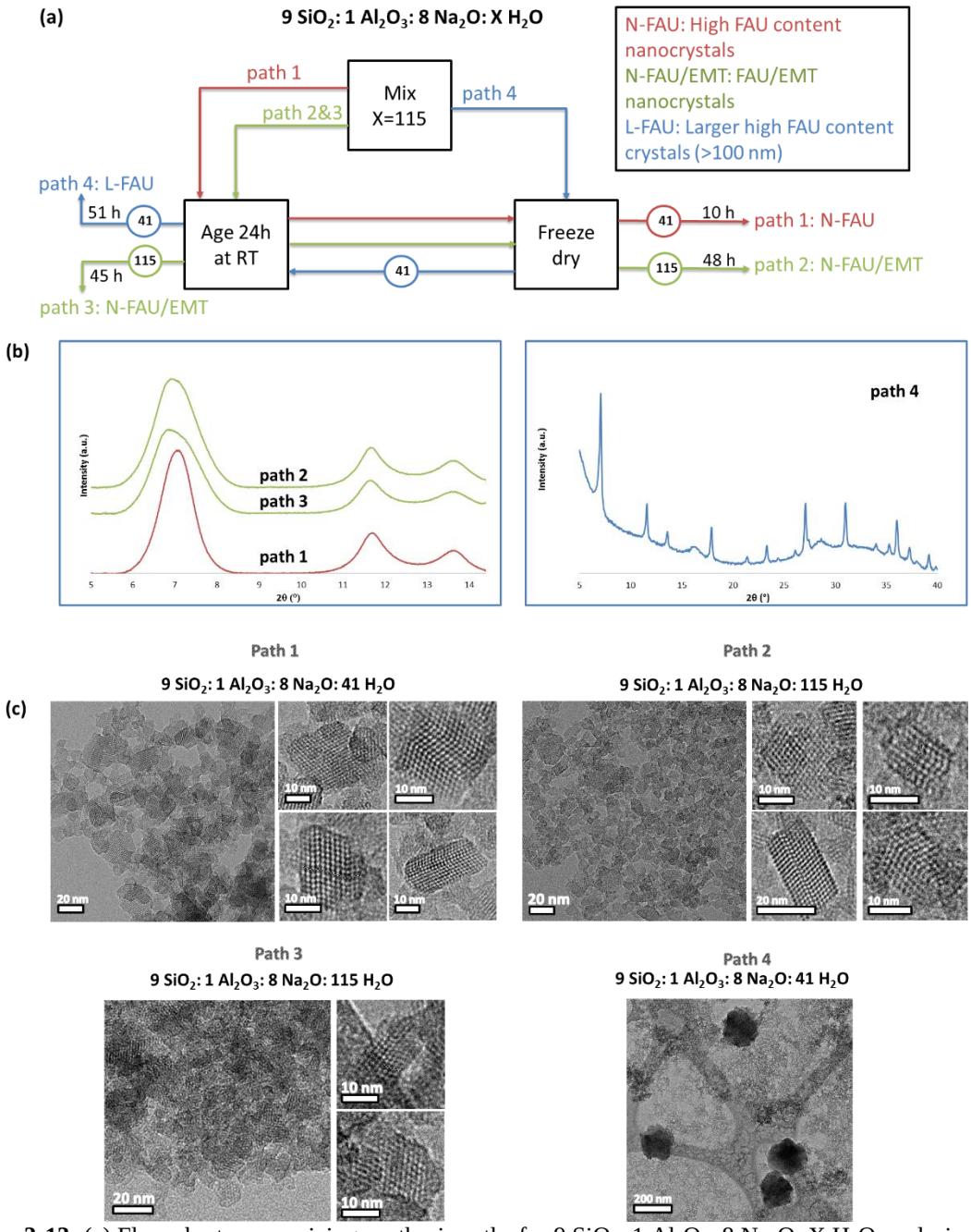

Figure 3-13: (a) Flow chart summarizing synthesis paths for 9 SiO_2: 1 Al_2O_3: 8 Na_2O: X H_2O exploring the effect of the starting composition, final composition, and the timing (before or after 24h room temperature aging) of freeze drying on Faujasite particle size and FAU/EMT content. Numbers in the circles represent H_2O/ Al_2O_3 ratios. Numbers in hours correspond to heating duration at 50 °C. **N-FAU**: Nano-crystals with improved FAU purity, **L-FAU**: Large crystals (>100 nm) with improved FAU purity, **N-FAU/EMT**: Nano-crystals with large EMT content. (b) XRD patterns (collected in-house) and (c) TEM images.

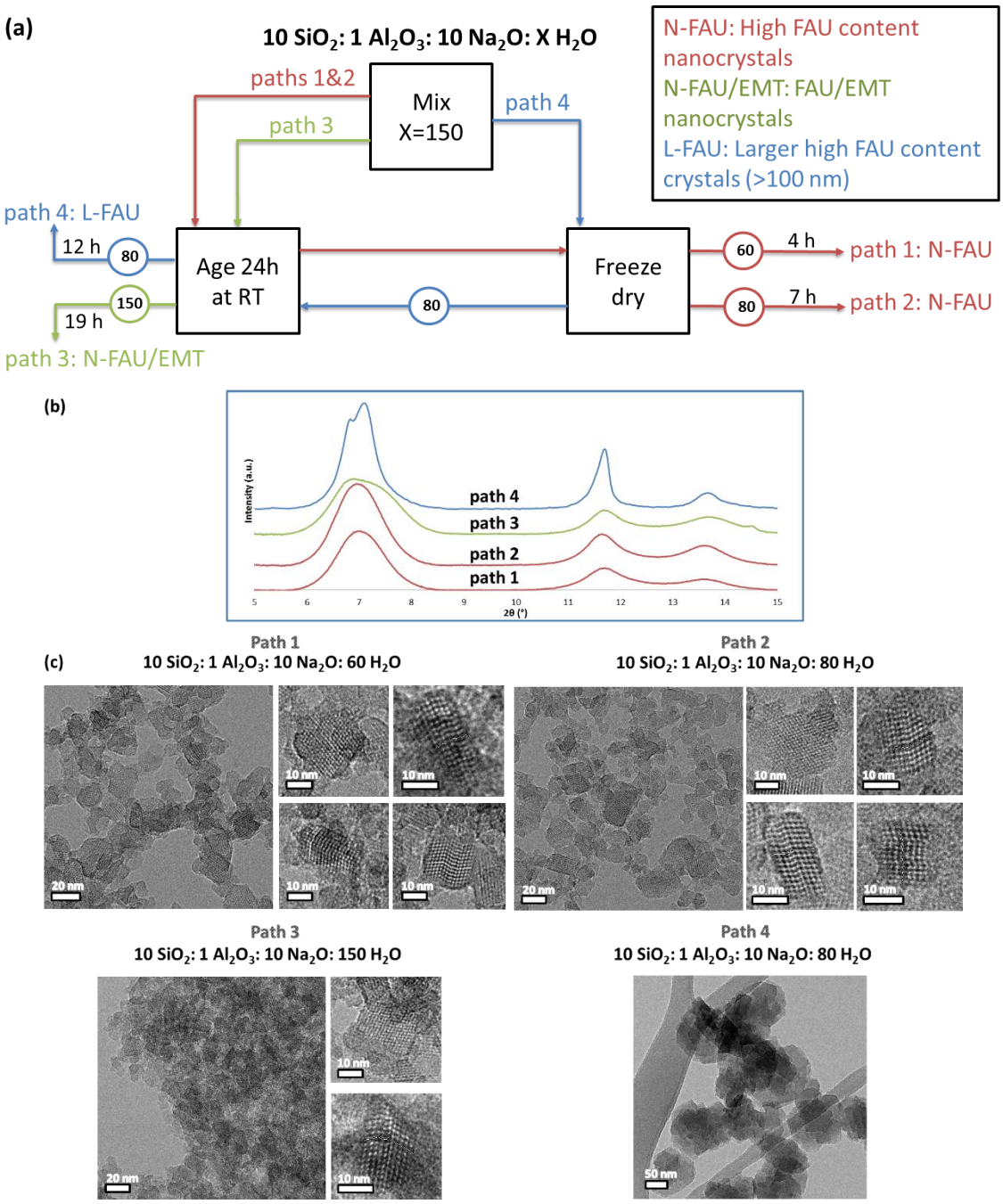

Figure 3-14: (a) Flow chart summarizing synthesis paths for 10 SiO_2: 1 Al_2O_3: 10 Na_2O: X H_2O exploring the effect of the starting composition, final composition, and the timing (before or after 24h room temperature aging) of freeze drying on Faujasite particle size and FAU/EMT content. Numbers in the circles represent H_2O/ Al_2O_3 ratios. Numbers in hours correspond to heating duration at 50 °C. **N-FAU**: Nano-crystals with improved FAU purity, **L-FAU**: Large crystals (>100 nm) with improved FAU purity, **N-FAU/EMT**: Nano-crystals with large EMT content. (b) XRD patterns (collected in-house) and (c) TEM images.

3.3.3 FAU Content of Nano-crystals

Table 3-1 shows that high FAU content nano-crystals can only be obtained following paths 1 in Fig. 3-12, 3-13 and 3-14, with aging before freeze-drying. Simulated XRD patterns for select samples from Fig. 3-1a, 3-9g, 3-12 and 3-13 are presented in Fig. 3-15 to 3-25 (experimental XRD patterns presented were collected at Beamline 17-BM at Advanced Photon Source, Argonne National Laboratory). *It seems that freeze-drying allows the extension of the higher FAU purity to nano-crystals by mixing and aging the sol at compositions favoring the formation of nano-crystals and then lowering the water content to allow the crystallization to proceed at conditions favoring the nucleation and growth of FAU.*

Table 3-1: DIFFaX fits to experimental XRD patterns of Faujasite samples from Fig. 3-1a, 3-9g, 3-12, and 3-13. The lateral size of crystals, number of stacked Faujasite sheets, faulting probabilities, and estimated total FAU fraction are given. When needed, samples are described by physical mixtures of pure FAU (population 1) and "representative" FAU/EMT crystals (population 2). Samples simulated using explicitly defined FAU/EMT crystals are described in terms of stacking of FAU ('F') and EMT ('E') sheets.

		Population 1 (α_{FF}=0.99, α_{EE} =0.01)		**Population 2**				
Sample (Fig. where it is presented)	Simulated XRD pattern	Lateral crystal size (nm)	Number of stacked Faujasite sheets	Lateral crystal size (nm)	Stacking of Faujasite sheets (number of sheets, or explicitly defined stackings)	α_{FF}	α_{EE}	Total FAU fraction
A (3-1a)	Fig. 3-15	Infinite	Infinite	X				0.99
E (3-1a)	Fig. 3-16	300	200	60	50	0.6	0.4	0.72
F (3-1a)	Fig. 3-17	40	30	100	EFFEFFFEEEE	-	-	0.59
I (3-1a)	Fig. 3-18	20	15	40	EEFFFEFEEFE	-	-	0.58
L (3-1a)	Fig. 3-19	20	15	40	30	0.5	0.75	0.64
N (3-1a)	Fig. 3-20	45	40	60	30	0.5	0.75	0.64
14 SiO_2: 1 Al_2O_3: 12 Na_2O: 106 H_2O (3-9g)	Fig. 3-21	-	-	200	100	0.85	0.4	0.8
Path 1 (3-12)	Fig. 3-22	50	40	50	40	0.7	0.5	0.79
Path 3 (3-13)	Fig. 3-23	20	15	30	EEFFFEFEEFE	-	-	0.58
Path 2	Fig. 3-24	20	15	30	EEFFFEFEE	-	-	0.62

(3-13)					FE			
Path 1 (3-13)	Fig. 3-25	-	-	25	15	0.8	0.2	0.8

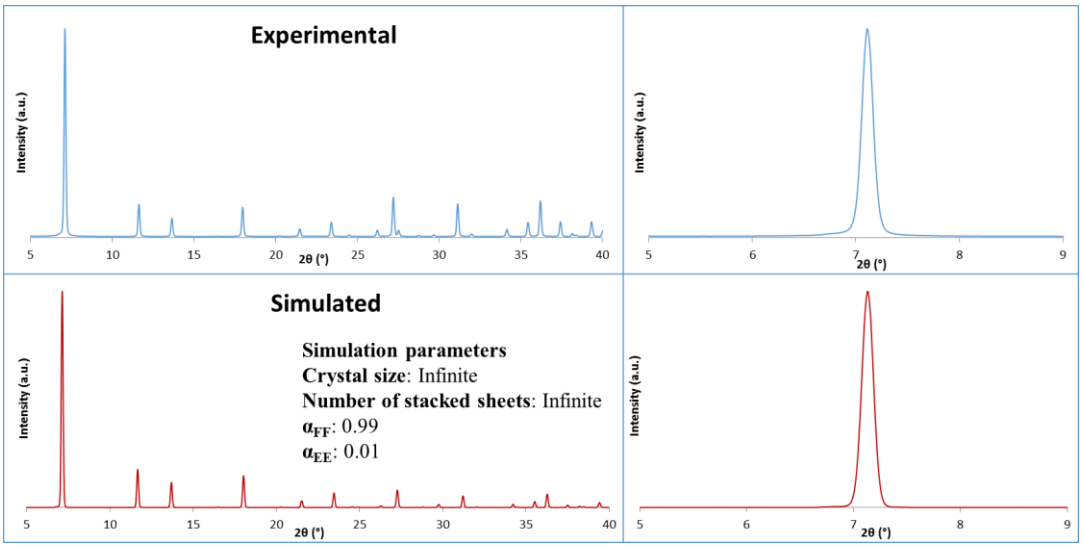

Figure 3-15: Simulated (DIFFaX) and experimental XRD patterns for sample A (Fig. 3-1a). Simulation parameters described in the inset.

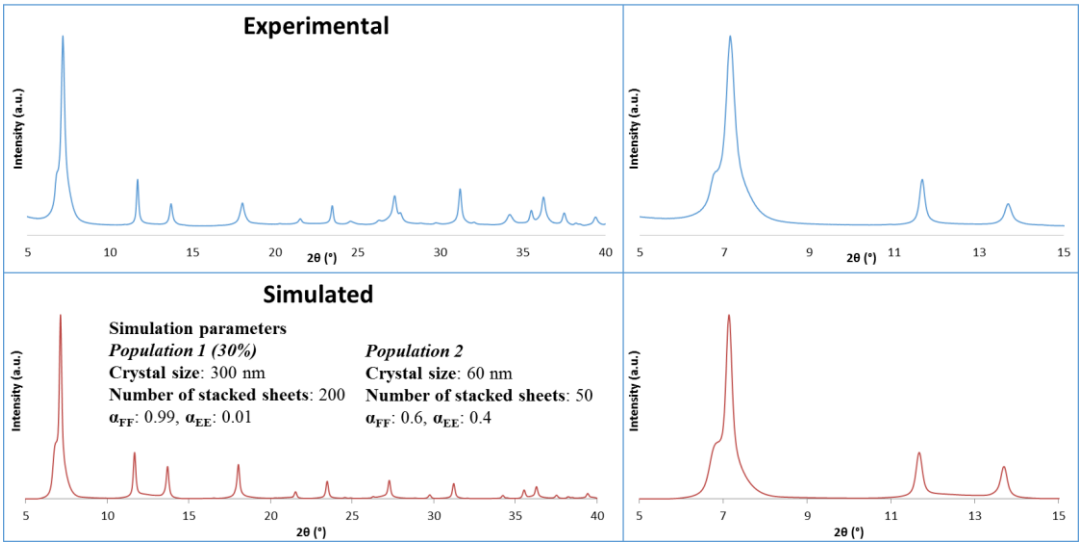

Figure 3-16: Simulated (DIFFaX) and experimental XRD patterns for sample E (Fig. 3-1a). Sample E (Fig. 3-1b) has a broad particle size distribution with crystal sizes ranging from smaller than 200 nm to as big as 1 μm. When simulating the XRD pattern, an average particle size of 300 nm gave a good fit to the experimental pattern with respect to peak broadening. However, the broadening of the EMT shoulder could only be accounted for by an even smaller size, around 60 nm (evidenced by TEM). This indicates that the EMT domains are interrupted by defects, likely caused by mismatch of Faujasite sheet stackings in different parts of the crystals. Though not perfectly accurate, a way to account for this difference in domain sizes in DIFFaX is to simulate the XRD patterns for 2 different populations. Simulation parameters described in the inset.

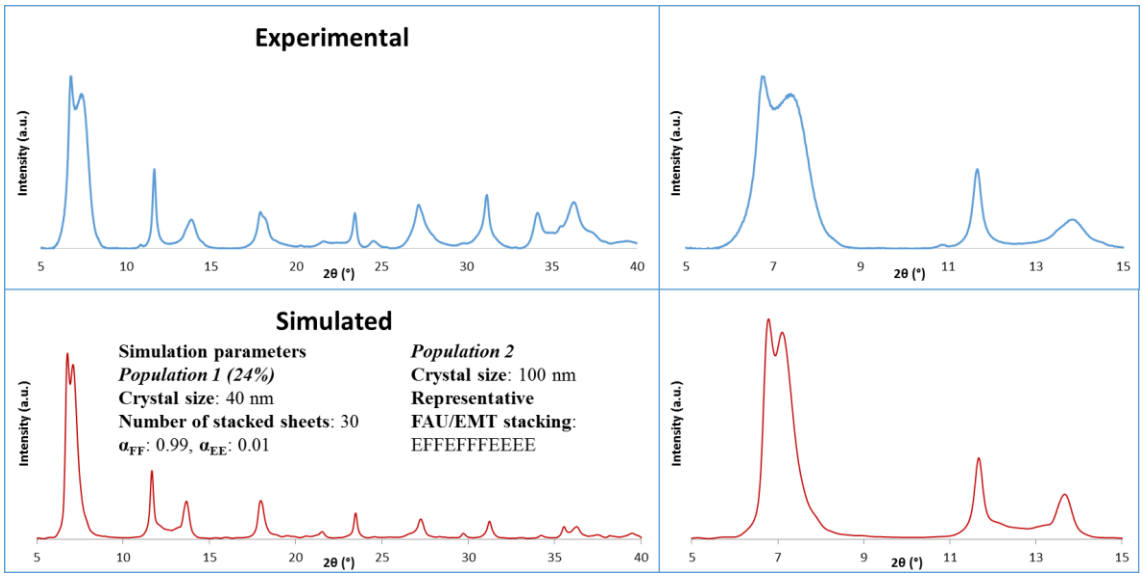

Figure 3-17: Simulated (DIFFaX) and experimental XRD patterns for sample F (Fig. 3-1a). Faulted crystals in sample F develop a highly anisotropic sheet-like morphology (Fig. 3-1b). For this reason, two crystal populations are needed to simulate the overall XRD pattern for the sample. Simulation parameters described in the inset.

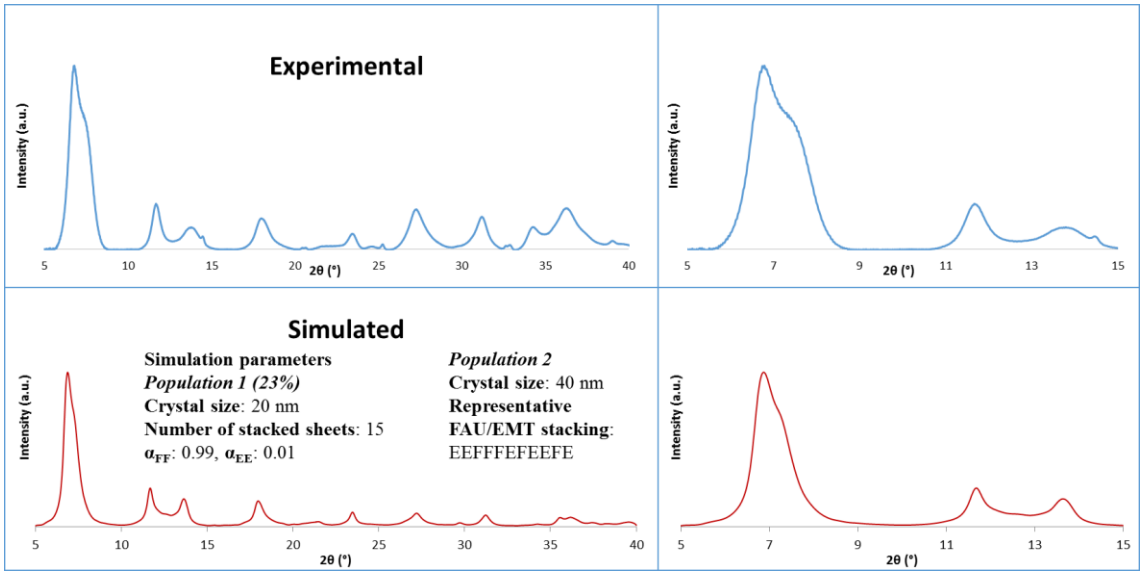

Figure 3-18: Simulated (DIFFaX) and experimental XRD patterns for sample I (Fig. 3-1a). The XRD pattern for sample I is very similar to that of sample F (Fig. 3-17), except that the peaks are broader. This is due to the smaller sizes of crystals. Both the pure FAU and the faulted crystals are of comparable sizes in this sample. Simulation parameters described in the inset.

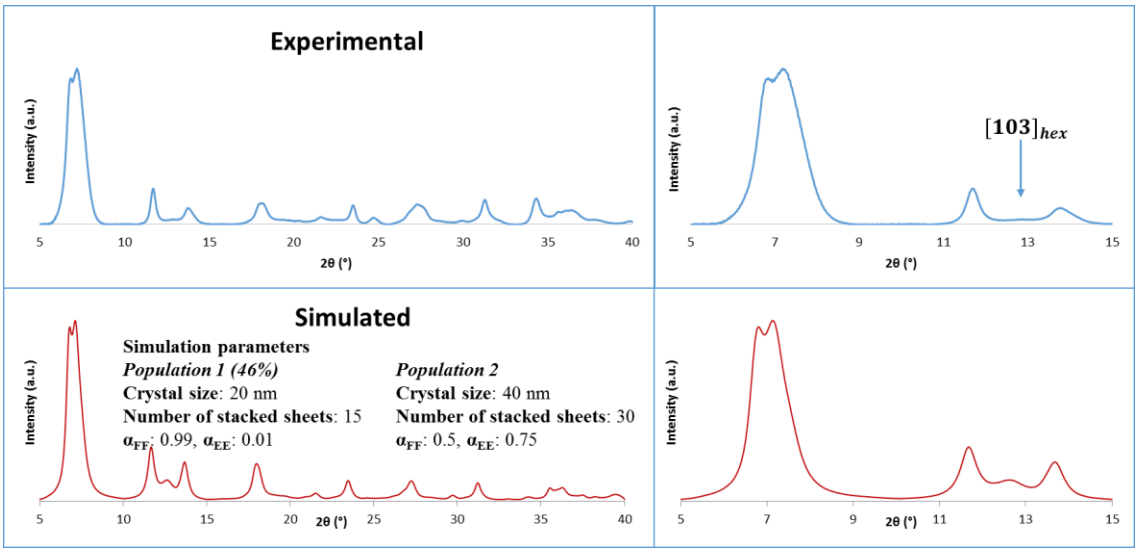

Figure 3-19: Simulated (DIFFaX) and experimental XRD patterns for sample L (Fig. 3-1a). The broad EMT [103] peak that shows up around 13° is an indication that the FAU and EMT domains in crystals are extended. Simulation parameters described in the inset.

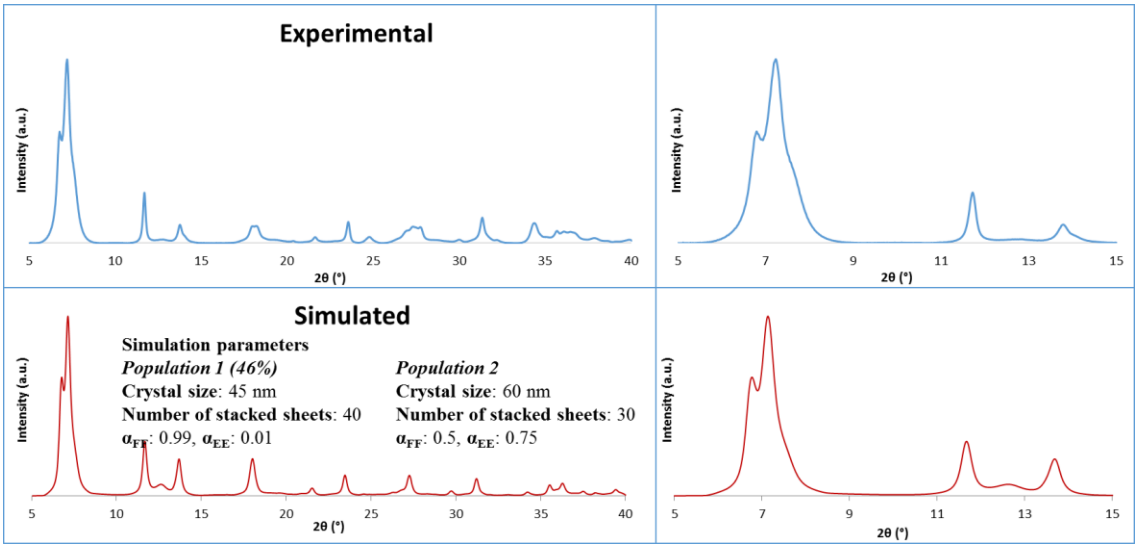

Figure 3-20: Simulated (DIFFaX) and experimental XRD patterns for sample N (Fig. 3-1a). Simulation parameters described in the inset.

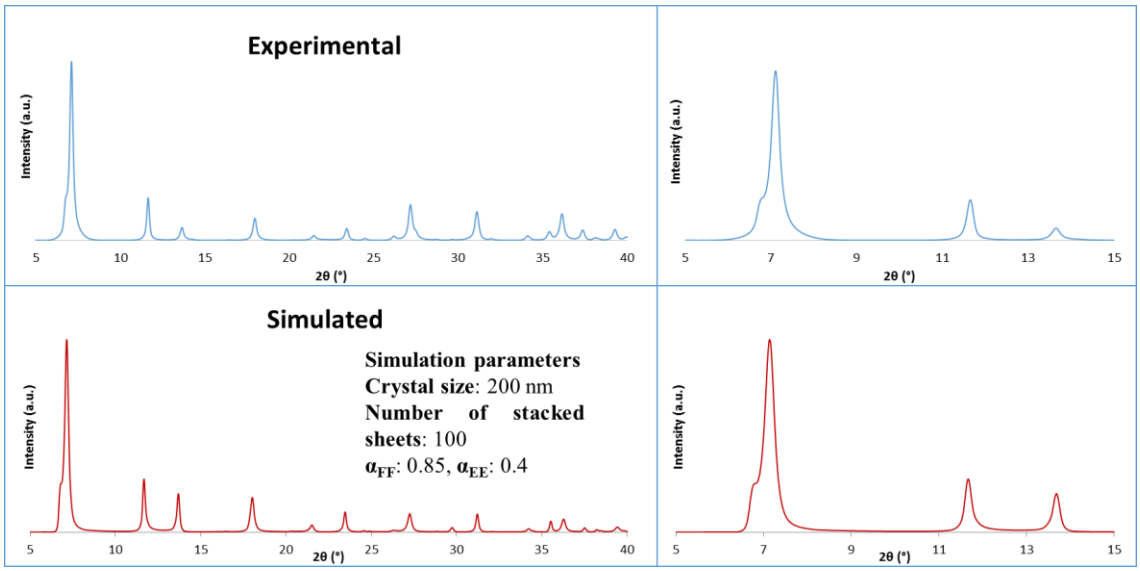

Figure 3-21: Simulated (DIFFaX) and experimental XRD patterns for sample synthesized from mixture 14 SiO_2: 1 Al_2O_3: 12 Na_2O: 106 H_2O (Fig. 3-9g). Simulation parameters described in the inset.

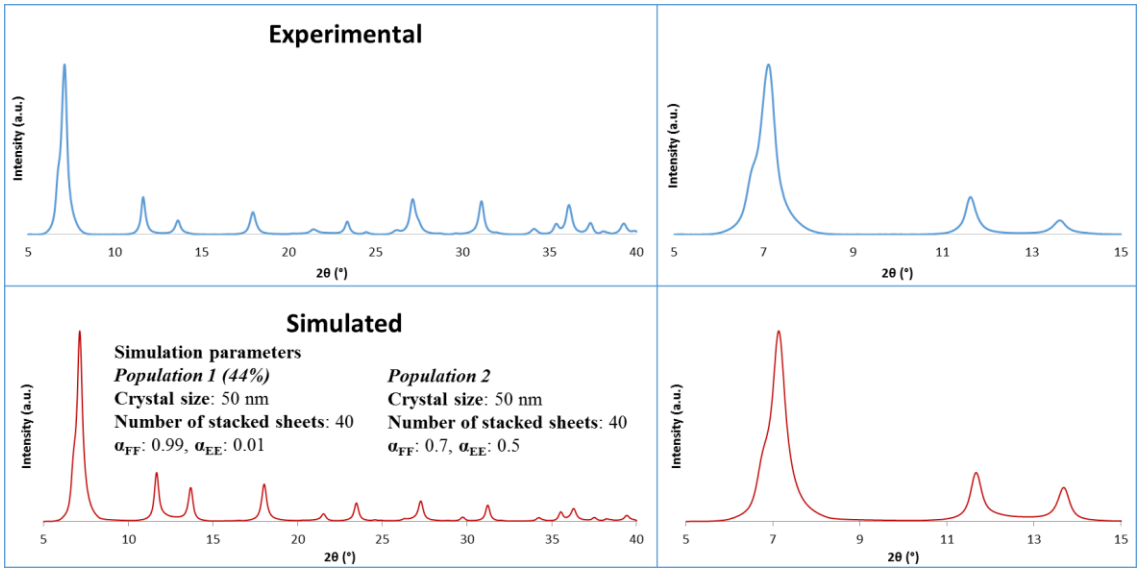

Figure 3-22: Simulated (DIFFaX) and experimental XRD patterns for sample synthesized following path 1 of Fig. 3-12. Simulation parameters described in the inset.

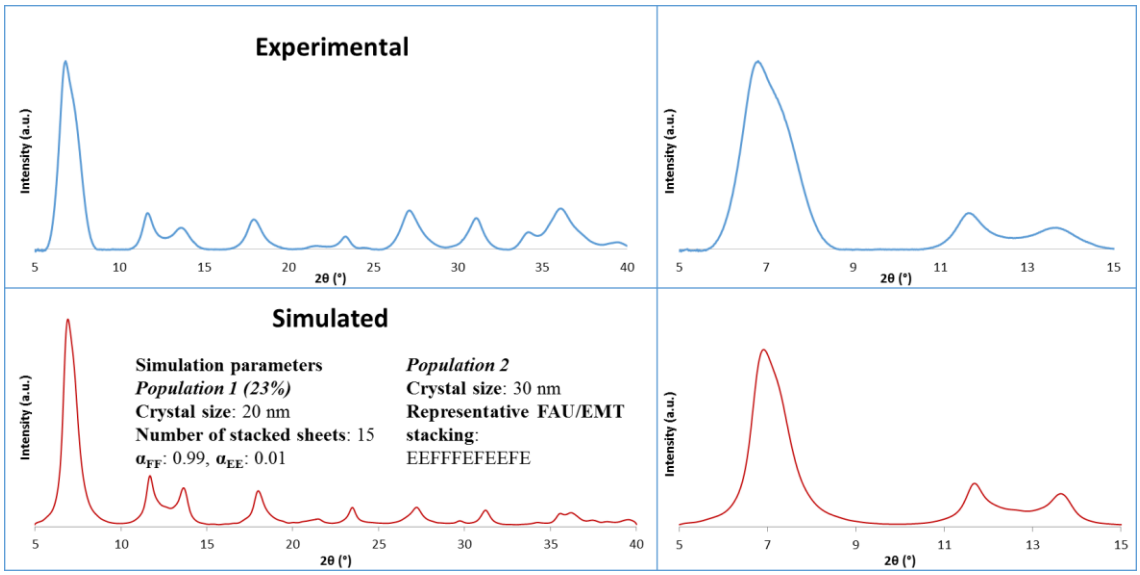

Figure 3-23: Simulated (DIFFaX) and experimental XRD patterns for sample synthesized following path 3 of Fig. 3-13. Simulation parameters described in the inset.

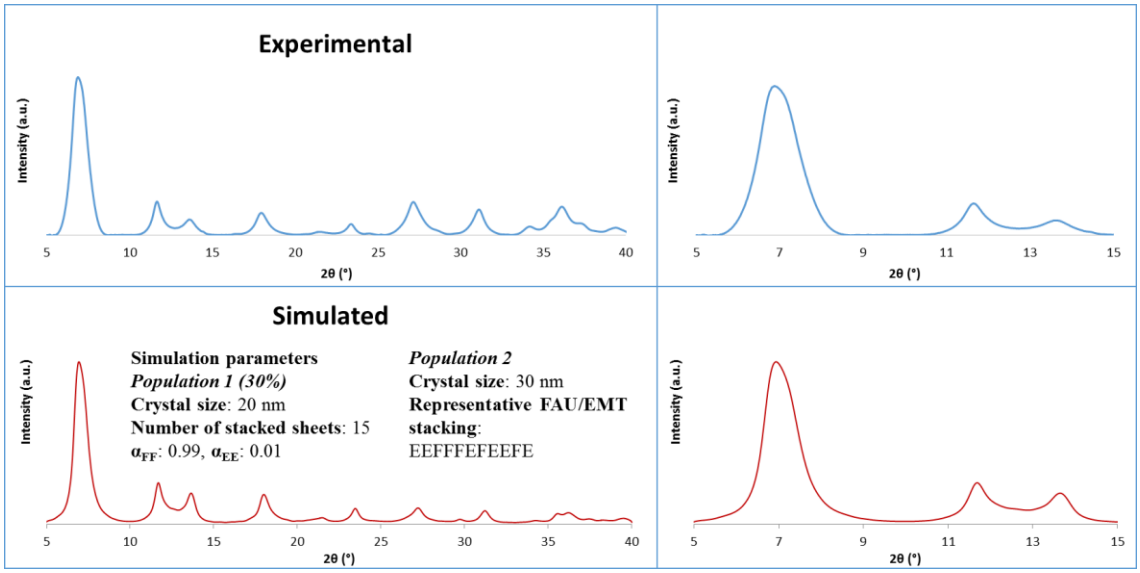

Figure 3-24: Simulated (DIFFaX) and experimental XRD patterns for sample synthesized following path 2 of Fig. 3-13. Simulation parameters described in the inset.

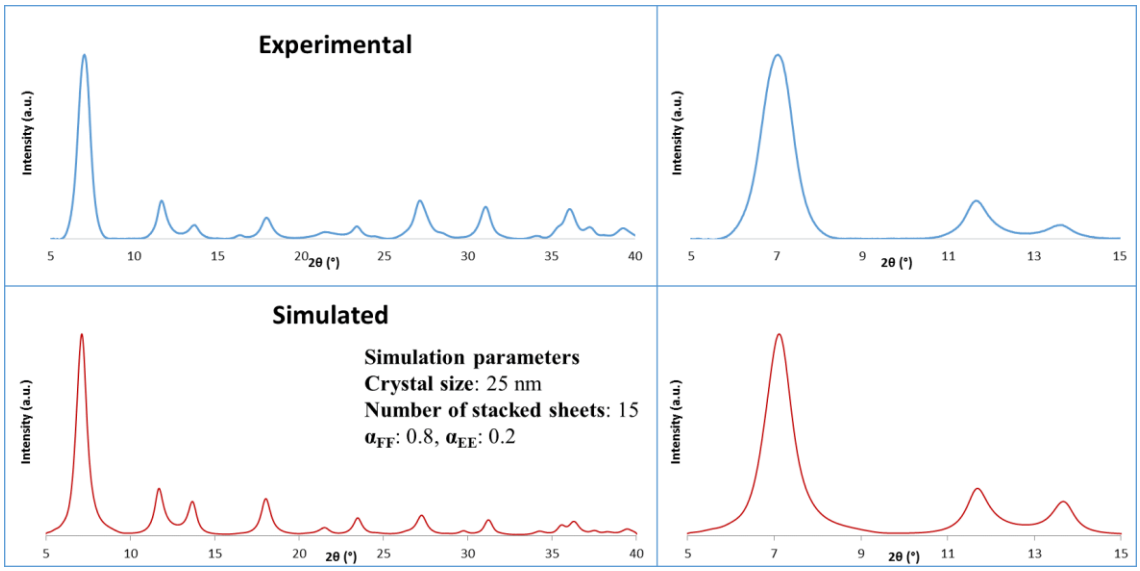

Figure 3-25: Simulated (DIFFaX) and experimental XRD patterns for sample synthesized following path 1 of Fig. 3-13. Simulation parameters described in the inset.

3.3.4 Elemental Analysis and Argon Physisorption

Inductively Coupled Plasma - Optical Emission Spectrometry (ICP-OES) was used to obtain Si/Al of select samples. Results show that samples have high Al content and are classified as zeolite X[91] (Si/Al of the starting synthesis sols compared to the dried powders after synthesis are shown in Table 3-2).

Table 3-2: Si/Al ratios of the starting synthesis sols compared to the dried powders after synthesis for select nano-Faujasite samples in Fig. 3-1a, Fig. 3-2a and Fig. 3-13 obtained using ICP-OES.

Sample code (Fig. where it is presented)	Crystalline dried powder Si/Al	Synthesis sol Si/Al
Q (Fig. 3-1a)	1.5	7.0
N (Fig. 3-1a)	1.4	5.0
O (Fig. 3-1a)	1.4	3.3
L (Fig. 3-1a)	1.4	7.0
A (Fig. 3-1a)	1.3	1.8
I (Fig. 3-1a)	1.2	5.0
E (Fig. 3-1a)	1.2	1.8
F (Fig. 3-1a)	1.1	1.8
S (Fig. 3-2a)	1.1	1.8
U (Fig. 3-2a)	1.5	5.0
Path 1 (Fig. 3-13)	1.3	4.6

Argon physisorption was used to study the textural properties of different samples in Fig. 3-1a. Argon adsorption/desorption isotherms (plotted on linear {Fig. 3-26a,c} and logarithmic {Fig. 3-26b,d} scales) show that the micropore volume of the Faujasite samples drop as the crystal size decreases. This is indicated by a decrease in the adsorbed argon volume at low relative pressures for all samples compared to micron sized FAU of sample A. This might be due to an increase in the defects in the crystals and amorphous domains in the samples and due to the reduction of micropore volume per unit mass for small crystal sizes. Sample A shows negligible mesoporosity. All the remaining samples presented in Fig. 3-26 develop significant mesoporosity as indicated by the increased Ar adsorption at high relative pressures and appearance of hysteresis in the adsorption/desorption isotherms. For samples in which particles grow as interpenetrating sheets, the volume between the sheets likely contributes to the overall mesopore volume (samples E, O and N).

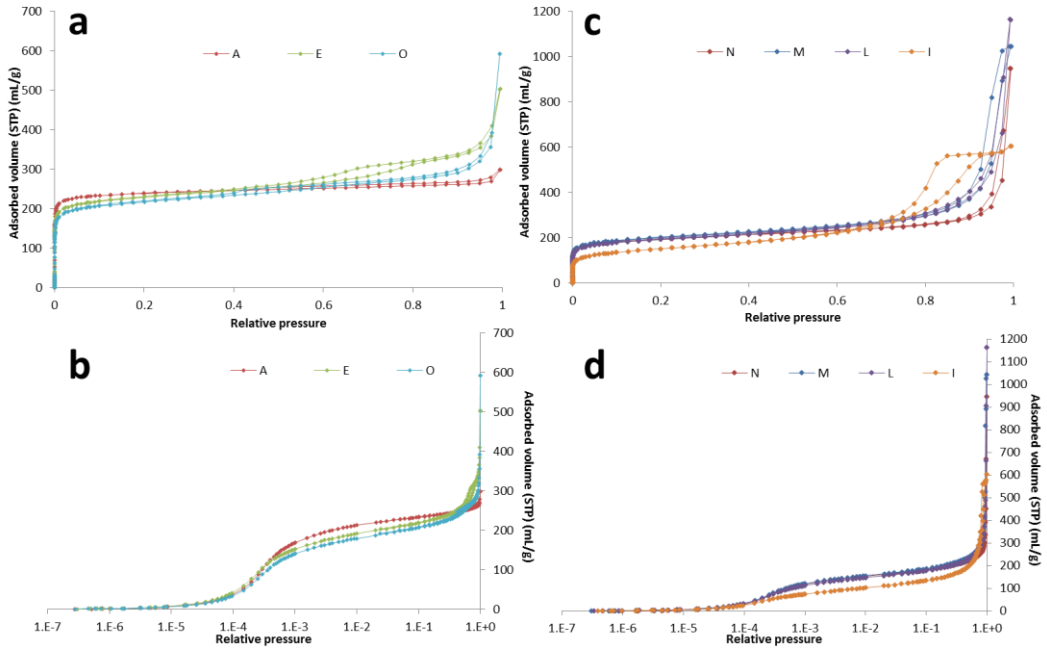

Figure 3-26: Argon adsorption/desorption isotherms plotted on a, c) linear and b, d) logarithmic scales. Legends correspond to sample label in Fig. 3-1a.

3.4 Conclusions

The effects of synthesis conditions on the FAU/EMT content and the size of nanocrystals, formed from inorganic aluminosilicate sols, were investigated. All the materials made contain intergrowths of FAU and EMT, as evidenced by high resolution TEM imaging and XRD simulations using DIFFaX. Certain synthesis compositions with low water content increase the FAU fraction up to 0.8 but the crystal size exceeds 100 nm. Findings demonstrated that it is possible to combine the effects of pre- and post-nucleation sol composition to steer crystal size and crystal structure, respectively. This allowed the extension of high FAU purity to nanocrystals by first mixing the sol at high water content compositions that favor nanocrystal formation and then - after a certain time - lowering by freeze-drying the water to levels favoring the formation of FAU.

Chapter 4

Room Temperature Evolution of Precursor Sol to Faujasite Nano-crystals

4.1 Introduction

4.1.1 Background

Although the events in the early stages of zeolite nucleation are important in determining the course of the subsequent crystallization, possibly allowing structural and morphological control of zeolite crystals, very little is understood about this complex process due to the challenges involved in available sample preparation and characterization techniques. Optically clear and colloidally stable nano-zeolite systems can serve as model systems to develop understanding of zeolite nucleation and growth.[136]

Proposed crystallization mechanisms for different zeolite systems range from solution-mediated transport to hydrogel transformation processes.[171] Studies on optically clear sols of silicalite, LTL and LTA demonstrate the presence of nanoscale, amorphous gel agglomerates that are associated with nucleation and growth of the crystals.[136,172–176] Different mechanisms have been discussed regarding this process, including assembly of the lattice through (i) soluble small species from solution, [171,177–179] (ii) aggregation and realignment of preassembled building blocks containing template molecule/aluminosilicate clusters,[180,181] and (iii) transformation of the gel phase.[171,176,181] In the next section an overview is given on the structure of colloidal silica and aluminosilicate sols along with nucleation and growth studies on the MFI zeolite system which has attracted a lot of interest.

4.1.2 Silica and Aluminosilicate Nanoparticles in Basic Aqueous Solutions

Precursor sols for the synthesis of Faujasite nano-crystals are made from silica source, alumina source, sodium hydroxide and water. The structure and stability of such sols was investigated by Fedeyko et al.[182] Silica in basic aqueous solutions of small organic cations (tetramethylammonium (TMA), tetrapropylammonium (TPA), and many

others), and monovalent inorganic cations (such as Na^+ and Cs^+) forms nanoparticles[183–190] as can be described by the following reactions:[191]

1- Dissociation of silicic acid,

$$Si(OH)_4 \overset{K_1}{\Leftrightarrow} Si(OH)_3O^- + H^+$$

2- Condensation of silica to form nanoparticles of size n,

$$Si(OH)_4 \overset{K_2}{\Leftrightarrow} \frac{1}{n}\left(SiO_{3/2}OH\right)_n + \frac{3}{2}H_2O$$

3- Dissociation of silanol groups in the nanoparticles,

$$SiO_{3/2}OH \overset{K_3}{\Leftrightarrow} SiO_{3/2}O^- + H^+$$

Nanoparticles that are uniform in size (3-10 nm) and shape are formed at a well-defined silica concentration exceeding the silica solubility limit (depending on pH, ~1:1 SiO_2/OH^- ratio). Below this concentration, the solution contains deprotonated form of $Si(OH)_4$ with small fractions of oligomeric species and neutral $Si(OH)_4$.[192] The minimum in the free energy of condensation explains why particles of small size form in solution, whereas the relatively high surface potentials predicted from the Poisson Boltzmann equation account for the nanoparticle stability in solution.[191] At high SiO_2/OH^- ratio, the system gels.

The addition of alumina substantially decreases the silica concentration at which nanoparticles are formed, particularly at low Si:Al ratios.[182] ΔG_{rxn} for the condensation of silicic acid with aluminum tetrahydroxide anion is more favorable than the dimerization of silicic acid.[193]

$$Si(OH)_4 + Al(OH)_4^- \overset{K}{\Leftrightarrow} (HO)_3SiOAl(OH)_3^- + H_2O$$

^{27}Al and ^{29}Si NMR spectroscopy was used to study the species present in aluminosilicate solutions at relevant zeolite-synthesis compositions.[194–198] The cation type can have a marked effect on the species observed in solution.[192]

At Si/Al concentrations above 4:1, the aluminosilicate system behavior approaches that of the pure silica system. For Na^+ cations, the nano-particle size decreases as the Si:Al ratio is increased and approaches that of pure silica system. SAXS patterns can be fitted as oblate ellipsoids.[182] In the case of sodium cations, they get incorporated within the inorganic silica/alumina core of the nanoparticles, in contrast to organic cations that appear to be excluded from such clusters.[187] Parameters that affect the nano-particle size include pH (smaller particles form at higher pH),[187] the type of cation (larger nano-particles were observed in the case of sodium cations compared to TPA cations) and temperature (higher temperatures lead to particle growth by Ostwald ripening).[191] Nano-particle size is independent of the silica concentration where the latter increases the number concentration of nano-particles.[191]

Such nano-particle sols yield crystalline zeolite crystals on aging. Lots of studies focused on understanding the role, or lack thereof, of the nano-particles in the nucleation and growth of MFI crystals in TPA-silica sols. The nature of these nano-particles and their role in early stages of MFI growth is still under debate.[188,199–203] A variety of characterization techniques including Small Angle X-ray Scattering (SAXS),[183,184,202,204,205] Ultra-Small-Angle X-ray Scattering (USAXS),[204] Dynamic Light Scattering (DLS),[188,190,206] Nuclear Magnetic Resonance (NMR) Spectroscopy,[179,194] and Transmission Electron Microscopy (TEM)[190,202,206] have been employed to examine MFI nucleation and crystallization. According to ref. 202, rectangular, nanometer-sized slabs with MFI structure result from the self-assembly of TPA-containing precursors that act as building blocks and directly attach to form MFI crystals. In another report, it was suggested that colloidal amorphous aggregates, formed in the solution prior to the onset of MFI crystallization, act as source of nutrients by dissolving to sub-colloidal particles and/or silicate ions which are consumed in the crystallization process.[204] Growth by the addition of low molecular weight species, most likely monomers, to the growing crystals was also suggested in ref. 173 and 188. The sub-colloidal particles might also act as building units that participate in an aggregation/densification process.[188] According to ref. 186, 10-15 nm aggregates of 2.8 nm primary precursor nano-particles are essential for the

nucleation of the zeolite and crystal growth occurs via the addition of the primary units to the growing crystal. The importance of aggregates of precursor nanoparticles following an oriented-aggregation mechanism in zeolite nucleation was also highlighted in other reports.[136,207] Authors in ref. 206 proposed that sub-colloidal particles contribute to the zeolite crystal growth and their addition to the growing crystal is the rate limiting step.

Considerably less studies focused on elucidating the events involved in the nucleation and growth of nan-Faujasite crystals. Mintova et al. studied the nucleation of zeolite Y at 100 °C by TEM from a system containing TMAOH.[208] They proposed that FAU crystals are nucleated in nanoscale amorphous gel aggregates existing in the colloidal aqueous solution. It was proposed that each amorphous aggregate nucleates only one single zeolite crystal, with nucleation always beginning at the gel - solution interface. Recently, Awala et al. reported the synthesis of high FAU content 10 nm zeolite Y from an inorganic sodium aluminosilicate system.[138] It was proposed that the synthesis procedure results in uniform (with respect to composition and size) discrete amorphous precursor nano-particles that evolve to nano-sized crystals, retaining their original size.[138]

In this work, we choose representative optically clear and colloidally stable nano-Faujasite precursor sols (from chapter 3), aged and crystallized at room temperature, to follow zeolite nucleation by *in situ* cryogenic Transmission Electron Microscopy (cryo-TEM) and Small Angle X-ray Scattering (SAXS) and study how the precursor nano-particles evolve to crystals. Specifically, we investigated whether discrete precursor nano-particles evolve to crystals or if the precursor nano-particles aggregate before the onset of crystallization (similar to the aggregative mechanism proposed for MFI by Davis et al.[136] and Kumar et al.[207]). Using cryo-TEM with crystal structure resolution we also determine if FAU and/or EMT nucleate in the system.

4.1.3 Cryogenic Transmission Electron Microscopy and Small Angle X-ray Scattering: Overview and Experimental Methods

The combination of two techniques, SAXS and cryo-TEM, was employed to follow the evolution of precursor sol to Faujasite nano-crystals. SAXS enabled the early detection of larger particles/aggregates and cryo-TEM enabled *in-situ* visual observation of the nano-particle and aggregate structures and the detection of crystallinity at the early stages of nucleation.

Cryo-TEM is a useful technique for obtaining structural information regarding objects in solutions in a near *in situ* state. It is usually employed to study water/surfactant[209,210] and biological systems.[211–213] These delicate structures are usually only stable in their native solution conditions and complete solvent removal in the high-vacuum of the TEM often results in the deformation or complete destruction of the structure.[214] In cryo-TEM, physical fixation of structures in solution is achieved by rapidly plunging the liquid dispersion into a suitable cryogen (usually liquid ethane) to convert the solvent into a solid-like, glassy state. By embedding the structures in a thin layer of vitrified solvent, they can be examined in their native state. Amorphous precursors in the early stages of zeolite ZSM-5 synthesis were also imaged by cryo-TEM,[136,188,207,215] and in a few reports zeolite structural resolution was obtained.[207,216] Cryo-TEM was also employed for *in situ* studies of mesoporous silica.[217]

Challenges associated with cryo-TEM include frost formation, film thickness control and transformation of vitreous ice into crystalline ice.[213,218] Frost formation (from moisture in the air) during sample preparation and transfer is unavoidable but can be minimized by careful sample handling. The sample droplet pipetted onto TEM grid is thinned into a film by gently blotting with filter paper before vitrification. Usually, vitrified films are less than ~300 nm in thickness. This can be tricky to achieve if the sample is viscous and sticky (as is the case for nano-Faujasite sol at the early stages). Parameters on commercial automated sample preparation stations, including blot time, number of blots and drain time can be optimized to control the film-thickness and its uniformity. Film-

thickness is particularly critical at the early stages of crystal growth, when the smallest crystalline domains are to be detected and this could be limited by the vitreous film thickness.[219] Crystalline ice is not desired because it could cause optical artifacts or redistribution of the structure organization. Hexagonal or cubic ice crystals can be formed if vitrification was not successful, or during imaging due to electron-beam irradiation.[213,220] Vitreous ice is kinetically trapped amorphous phase which can transform first to cubic crystalline ice (metastable) and then to hexagonal crystalline ice (thermodynamically stable phase) if the temperature is not kept low or if the electron-beam exposure is not kept minimum.[221]

Another issue associated with imaging zeolite precursors and crystals by cryo-TEM is the low contrast of precursor nano-particles and crystals in the unaltered sol. In this work, this is mainly a consequence of the high concentration of sols employed in the synthesis of Faujasite nano-crystals, but is also contributed to by the vitrous film thickness. Significant phase contrast can be gained by under-focusing the objective lens such that objects with inner electron potentials different from the vitreous solvent become visible. However, it should be noted that a large under-focus may be accompanied by loss of resolution and the appearance of optical artifacts such as reversed contrast and Fresnel fringes. Consequently, images obtained may not present the true physical size, and it is possible some details are obscured.[218]

In this work, cryo-TEM samples were prepared according to the method described by Talmon.[210] Grids for examination were prepared using the FEI Vitrobot System. Specimens were prepared by transferring a small drop of the sample to a copper grid coated with ultrathin Carbon (<3nm) on Carbon Holey support film (Ted Pella Inc.). All samples studied were unaltered with the exception of those taken from sols after freeze-drying and lowering the water content (mixture becomes a sticky solid). Parameters including blot time, number of blots, drain time and sample volume were optimized to control the film-thickness and its uniformity. Specimens were vitrified in liquid ethane and transferred under liquid nitrogen to a Gatan 613 cooling holder. Imaging was performed at <-170 °C using an FEI Tecnai G2 F30 TEM operated at 300 kV. The

microscope has a twin pole piece with a point-to-point resolution of 0.24 nm and enabled us to obtain images with structural resolution. Since zeolites are beam sensitive materials, the electron dosage to the specimen was kept to a minimum (~20 e/Å^2) by using low-dose imaging mode.[222–224] The grid was scanned at low magnification to search for areas of interest. Focusing and astigmatism correction were then performed at the working magnification on an area approximately 2 μm from the area of interest to reduce the beam damage to the specimen.

SAXS was used as a complementary technique to cryo-TEM to detect the onset of precursor nano-particle aggregation due to the fact that scattering intensity is proportional to particle size to the sixth power. SAXS is sensitive to the electron density contrast (between 1-50 nm particles and the medium they are suspended in) and can capture the very early stages of aggregation without uncertainties due to dust and contamination (as opposed to Dynamic Light Scattering).[225] Moreover, it can monitor the nano-particle and aggregate populations simultaneously.

A SAXSess Small- Angle X-ray Scattering (SAXS) instrument (Anton-Parr) was employed to follow the evolution of the precursor nanoparticles and crystals in clear sols. The instrument is equipped with a Cu Kα slit-collimated radiation source (wavelength of 1.54 Å). Slit collimation is beneficial in that a larger volume of sample is illuminated at once and therefore data collection time may be significantly reduced without a reduction in measured intensity. Samples were placed in a vacuum-tight 1-mm quartz capillary and scattering was measured at room temperature. Scattering from sodium hydroxide solution in water (12.5 M) was subtracted as background.

4.2 Results and Discussion

A sol with composition 14 SiO_2:1 Al_2O_3:12 Na_2O:214 H_2O (from chapter 3) was followed at ambient temperature by *in situ* cryo-TEM and SAXS to detect the early stages of precursor nano-particle evolution and Faujasite nucleation. These experiments were done using Al foil and LUDOX® HS-30 as sources of aluminum and silicon,

respectively. This composition was chosen because the system is clear on mixing aluminate and silicate solutions, nucleates FAU/EMT nano-crystals with negligible interpenetration, and is colloidally stable (i.e. particles do not settle down for over 6 months). The rapid evolution of the system made it practical to study it at room temperature while allowing us to capture the initial stages of amorphous precursor nanoparticle evolution before crystallization without introducing complications that might arise from quenching before characterization.

Fig. 4-1 shows cryo-TEM images and SAXS profiles of intensity versus $q = (4\pi/\lambda)\sin\theta$ (where θ is half the scattering angle and λ=1.54 Å is the wavelength of the incident beam) for unaltered samples taken at different periods during aging at room temperature. Upon adding the aluminate solution (solution B) dropwise to the silicate solution (solution A) in ice bath while stirring (refer to section 3.2), the sol remains clear (Fig. 4-1a). The first sample is taken after 1h mixing in ice bath (sample 0). In-situ Cryo-TEM from the unperturbed sample shows the presence of polydisperse amorphous nano-particles up to 2.5 nm in size (Fig. 4-1b), in agreement with SAXS (Fig. 4-1g, 0 days trace). Under-focused conditions were needed to image the nano-particles due to their low contrast with the sol liquid. The role of these nanoparticles (spectators versus participants in nucleation and growth) is important to establish.

After 1 day at room temperature, sample 1 shows the appearance of large entities evident by the rise in the low-q SAXS scattering intensity (Fig. 4-1g, 1 day trace). Cryo-TEM shows that these large entities are aggregates of the ~2.5 nm amorphous precursor nano-particles (Fig. 4-1c). No crystallinity is detected in the aggregates by taking a series of images at different focus levels showing that the precursor nano-particles aggregate before the emergence of detectable crystallinity. The aggregates become bigger with time (Fig. 4-1g, 2 days trace) and develop a non-compact aggregate appearance but remain amorphous (Fig. 4-1d). The sol turns slightly cloudy at around 3 days at room temperature (Fig. 4-1a).

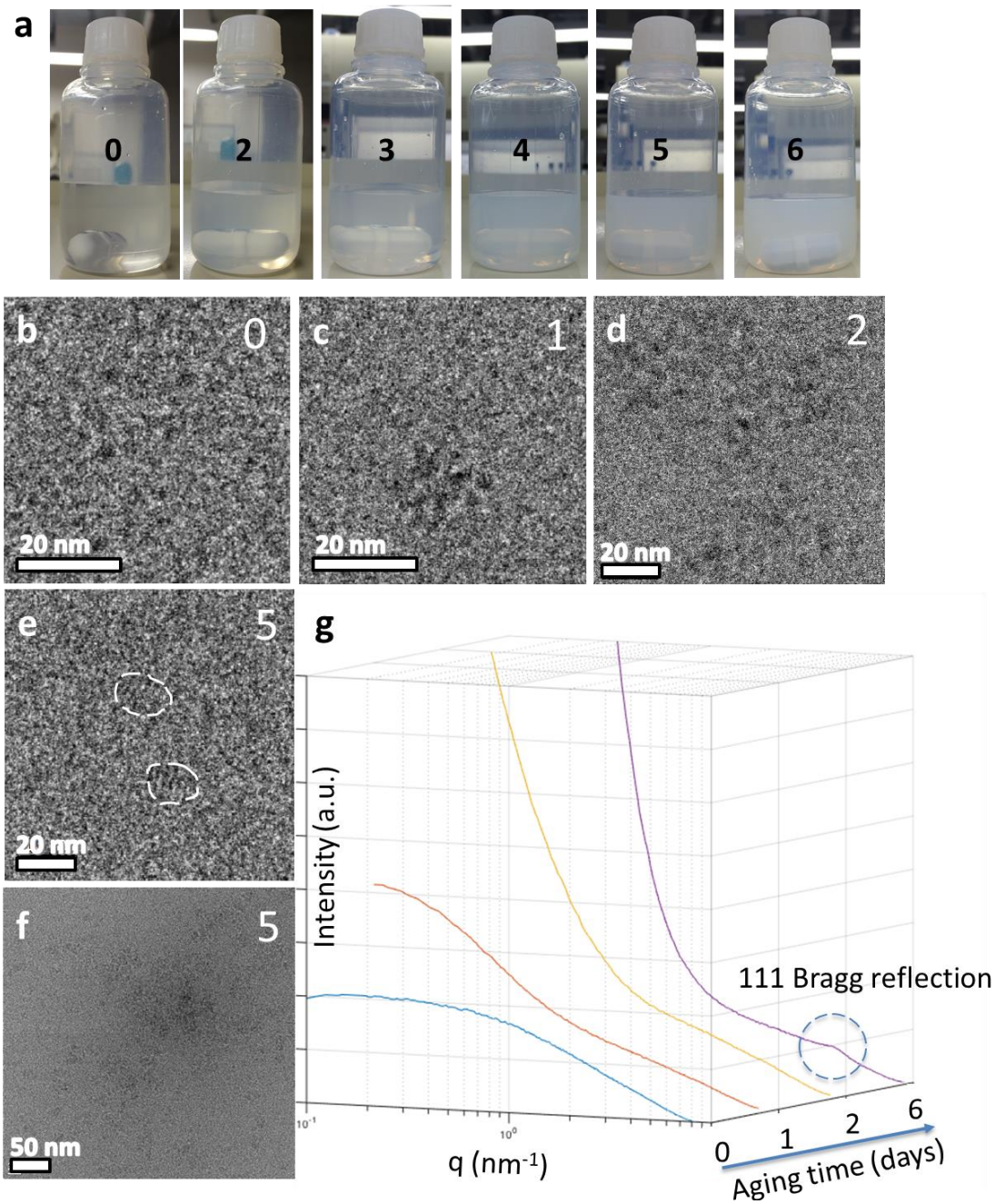

Figure 4-1: (a) Change in the appearance of mixture of composition 14 SiO_2:1 Al_2O_3:12 Na_2O:214 H_2O with increased aging time at ambient temperature. Inset numbers correspond to aging time in days. Cryo-TEM images for unperturbed samples taken after (b) 1h of mixing aluminate and silicate, (c) 1 day, (d) 2 days and (e,f) 5 days aging at room temperature. (e) High magnification showing crystals with white lines highlighting the crystal perimeter and indicating the absence of well-developed facets. (f) Low magnification showing non-compact aggregates of precursor nano-particles. (g) SAXS profiles of intensity versus $q = (4\pi/\lambda)\sin\theta$ (where θ is half the scattering angle and λ is the wavelength of the incident beam) for samples taken at different periods during aging at room temperature.

Crystals were detected by cryo-TEM after 5 days aging at room temperature (Fig. 4-1e) and they coexist with amorphous aggregates (Fig. 4-1f). The ~14Å lattice spacing is attributed to the (111) planes in the FAU structure or the (002) planes in the EMT structure. At this early stage of the synthesis, the ~15 nm crystalline domains do not have well developed facets. Eventually, the (111) Bragg reflection becomes evident in the SAXS profile after 6 days (Fig. 4-1g, 6 days trace).

The sizes of the crystalline domains extend over several ~2.5 nm precursor nano-particles showing that several precursor nano-particles contribute to the nucleation. Due to the low contrast of the precursor nano-particles at focus, under-focused images were needed to show their aggregate morphology at early stages of growth (Fig. 4-2).

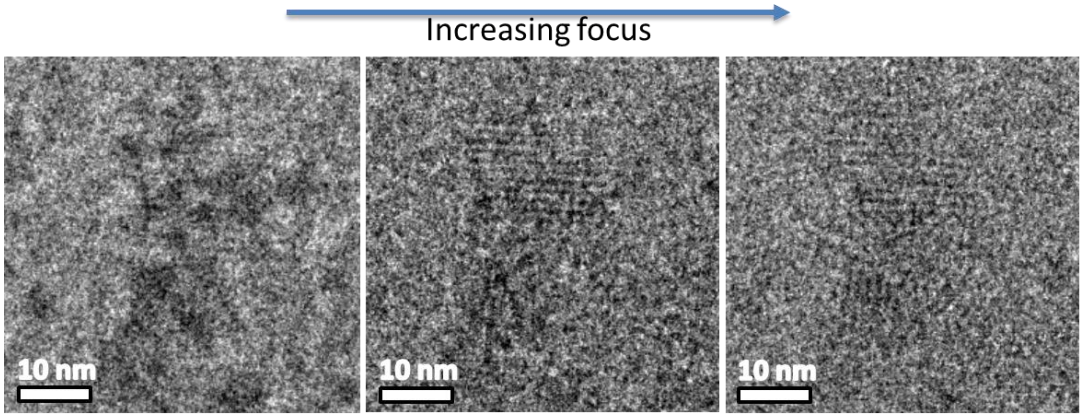

Figure 4-2: Aggregate-like crystalline nano-Faujasite evident from a focus series of cryo-TEM images. This image is taken from sample after 7 days at room temperature.

Evidence that EMT nucleates at various stages of synthesis is provided from cryo-TEM images of crystals imaged at different aging periods (Fig. 4-3). Fig. 4-3a shows a crystal imaged after 6 days at room temperature, viewed along $[1\bar{1}0]_{cubic}$, with only 4 Faujasite sheets. With the resolution in hand, this crystal could correspond to either 1.5 unit cells of EMT (Fig. 4-3b) or 2 FAU sheets with 1 EMT sheet in the center (Fig. 4-3c). Certainly, it cannot be interpreted as a pure FAU crystal suggesting that even at very small sizes FAU/EMT can coexist. Pure EMT crystals (Fig. 4-3d) are also detected after 15 days at room temperature (less faulted crystals are also detected- Fig. 4-4). These results exclude the possibility that FAU nucleates first and EMT domains form only on growing crystals.

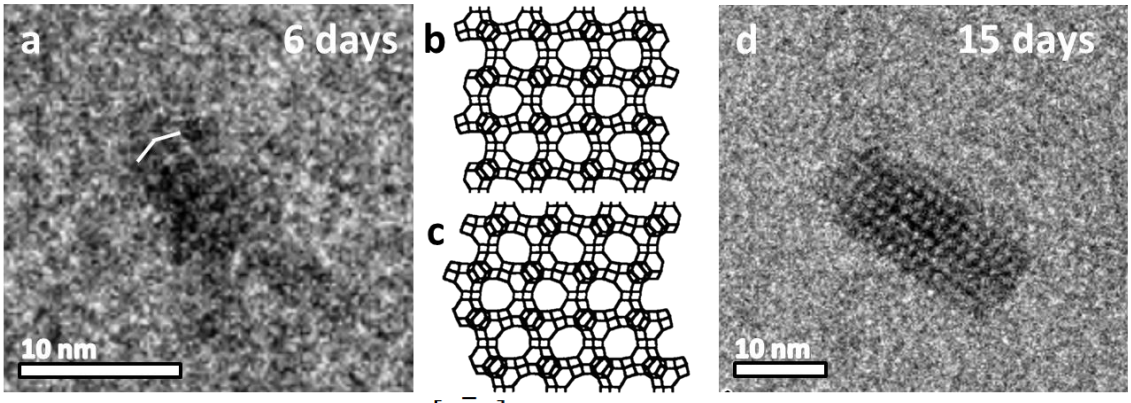

Figure 4-3: Cryo-TEM images showing $[1\bar{1}0]_{cubic}$ views of (a) crystal with only 4 Faujasite sheets and (d) pure EMT crystal. Inset indicates the aging period at ambient temperature. Possible representations of the Faujasite sheet stacking for the crystal in 'a', (b) 1.5 unit cells of EMT and (c) 2 FAU sheets with 1 EMT sheet in the center.

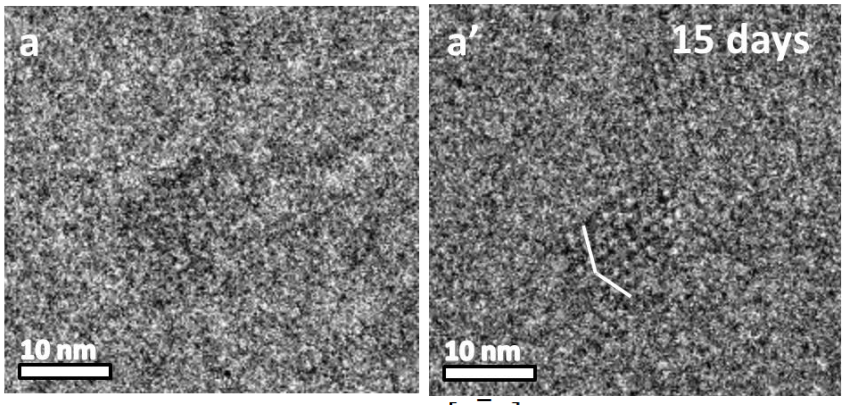

Figure 4-4: Focus series of cryo-TEM images showing $[1\bar{1}0]_{cubic}$ view of crystal with single fault at the center. Inset indicates the aging period at room temperature.

We propose that nano-Faujasite studied in this work follows a similar aggregative nucleation mechanism as the MFI studied by Davis et al.[136] and Kumar et al.[207] In earlier work on the aggregative crystal growth of the zeolite MFI from precursor nanoparticles, it was proposed that the precursor nanoparticles, despite having similar sizes, have different structure, stability to dissolution and colloidal stability. They can be differentiated into fresh (A) and mature (B) nanoparticles with respect to their stability and ability to contribute to aggregation. Fresh particles, A, are colloidally stable particles (possibly with a short life time) that do not aggregate, while particles B are particles that have evolved in structure, have longer lifetime, and are able to contribute to

aggregation.[226] In more detailed models, particles B could be further differentiated among them based on their stage of evolution (B_1 to B_m) but here for simplicity we do not consider this differentiation.[136] Another class of particles is that of growing aggregates, called C_i, which can aggregate with particles B and grow in size. A simple aggregation model describing this sequence was analyzed in ref. 226 and is as follows:

$$A \xrightarrow{k_1} B$$

$$B \xrightarrow{k_2} C_1$$

$$B + C_i \xrightarrow{K_i} C_{i+1}$$

Assuming that K_i is a constant independent of the size of the aggregate, $K_i = K$, for all i, the model (called model I in ref. 226) has two parameters $a = {k_1}/{k_2}$ and $b = \frac{n_{A_0} K}{k_2}$, the ratio of which determines the size distribution of the aggregates C_i; small aggregates with a narrow distribution are favored at higher $\frac{a}{b}$ ratios. Particles C_i could be further considered to aggregate ($C_i + C_j = C_{i+j}$) by introducing more parameters in the model but the conclusion regarding the effect of the $\frac{a}{b}$ ratio on the distribution of aggregates remains the same and for the purpose of this discussion $C_i + C_j$ aggregation will be neglected. In ref. 136 and 226, particles C_i were considered to be zeolite crystals but this early assignment was revised by the findings of ref. 207 where it was shown that, similar to the current findings, aggregation takes place before the formation of zeolite crystals and that early aggregates (called C_x in ref. 207) do not have a zeolite structure detectable by cryo-TEM. However, nucleation kinetics and final crystal size distribution are still correlated to the same $\frac{a}{b}$ parameter since larger aggregates are expected to yield larger zeolite particles.

A schematic representation of the proposed sol evolution before zeolite nucleation is shown in Fig. 4-5.

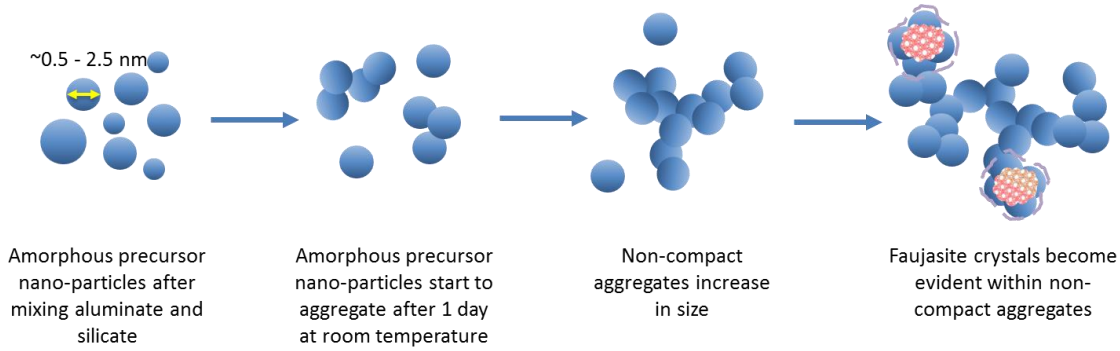

Figure 4-5: Schematic representation of the proposed sol evolution before Faujasite nucleation.

In ref. 136, 207 and 226, there was only one zeolite structure formed, MFI. Here, there is competition for the formation of two structures, FAU and EMT. This complexity allows us to acquire new insight regarding the role of the particles and the solution phase of the sols in the crystal growth process. It appears that the water content of the sol affects the particle size determining parameter, $\frac{a}{b}$, and the kinetics of growth of FAU over EMT in opposite ways. Higher water content favors fast evolution of the precursor nanoparticles, and therefore, formation of small aggregates that yield nanocrystals; but lower water content is required to increase FAU growth. It then ensues that aging at high water content followed by freeze-drying to low water content (as introduced in ref. 138) enables the combination of these two crystallization trajectories to obtain higher purity FAU, by first evolving the precursor nanoparticles and amorphous aggregates under high water content (high $\frac{a}{b}$ parameter) to minimize the aggregate size, and then creating the sol composition (low water content), which favors the growth of FAU.

This combination of trajectories is applicable to different compositions (14 SiO_2: 1 Al_2O_3: 12 Na_2O: 214 H_2O reduced to 100 H_2O after aging (Fig. 3-12 - path 1), 9 SiO_2: 1 Al_2O_3: 8 Na_2O: 115 H_2O reduced to 41 H_2O after aging (Fig. 3-13 -path 1) and 10 SiO_2: 1 Al_2O_3: 10 Na_2O: 150 H_2O reduced to 60 and 80 H_2O after aging (Fig. 3-14 - paths 1 and 2). For all cases, enrichment to high FAU content in nanosized crystals was achieved and cryo-TEM observations reveal a consistent evolution. Specifically, a sol mixed and aged

with composition 9 SiO_2:1 Al_2O_3:8 Na_2O:115 H_2O and then adjusted to 9 SiO_2:1 Al_2O_3:8 Na_2O:41 H_2O (Fig. 3-13 -path 1) was also followed at room temperature by *in situ* cryo-TEM (Fig. 4-6). Similar to the sol with composition 14 SiO_2:1 Al_2O_3:12 Na_2O:214 H_2O, discrete precursor nanoparticles are detected after mixing silicate and aluminate solutions (Fig. 4-6a) that form large open aggregates at 24h aging (Fig. 4-6b,c). The nanoparticles do not show crystallinity detectable by cryo-TEM upon aggregation. Crystallinity is detected (Fig. 4-6d) in sols aged 3 days after freeze-drying and composition adjustment (5 days from the point of mixing the aluminate and silicate solutions). Crystals comprising aggregates of precursor nano-particles were imaged at under-focused conditions (Fig. 4-6dII and 4-6e''). As expected, crystals that are predominantly FAU were detected in this sample.

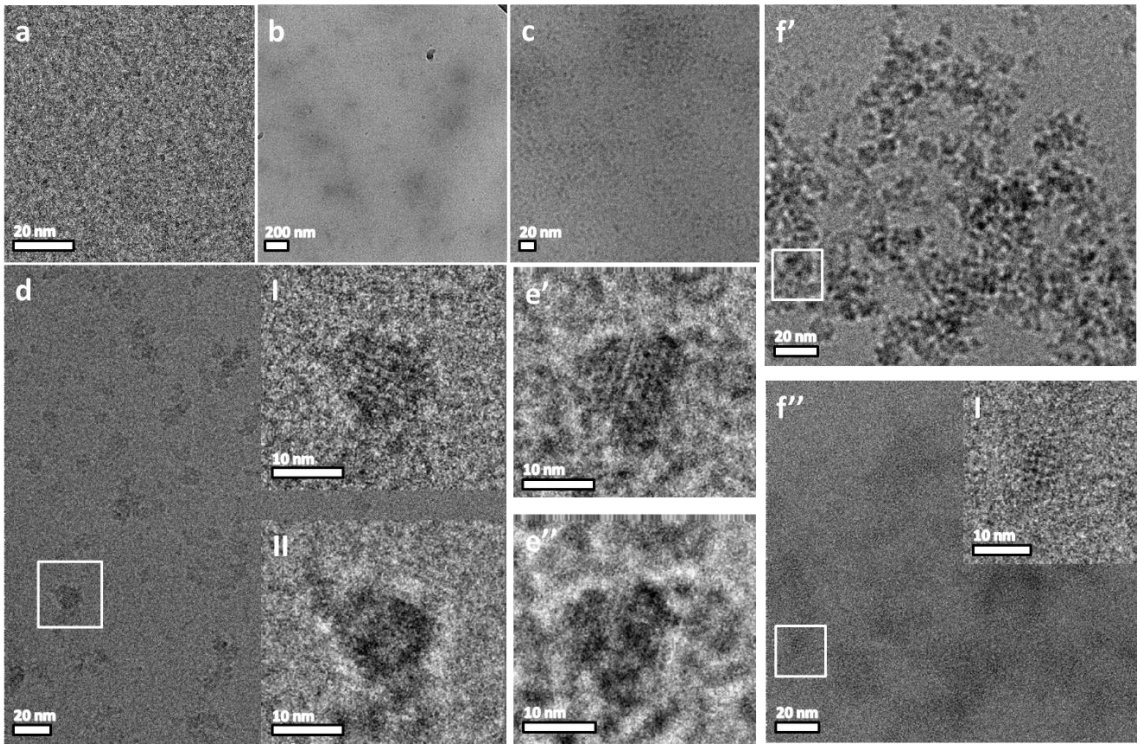

Figure 4-6: Cryo-TEM images of unperturbed samples taken from sol synthesized following path 1 in Fig. 3-13 after (a) 2h of mixing aluminate and silicate and (b,c) 1 day aging (right before freeze drying). Cryo-TEM images for diluted samples taken from sol after composition adjustment using freeze drying, (d) 3 days after freeze drying (inset images show aggregate-like crystalline nano-Faujasite evident at different focus levels), (e',e'') $[1\bar{1}0]_{cubic}$ views of FAU crystal with single fault imaged at different focus levels (8 days after freeze drying) and (f') underfocused and (f'') in-focus images of loose aggregate (3 days after freeze drying) within which FAU crystal was detected (inset in f'').

It appears that within the range of concentrations investigated here, the precursor nanoparticle evolution and aggregative model introduced in ref. 136, 207 and 226 holds for explaining the sequence of events leading to FAU/EMT nanoparticles. It accounts for evolution and aggregation of precursor nanoparticles to form amorphous aggregates that serve as scaffolds on which nucleation of the zeolite takes place followed by their gradual transformation to nanocrystalline zeolite aggregates. The formation of amorphous aggregates before Faujasite nucleation shows the importance of intra-aggregate rearrangements in nucleation and growth.[175,176] Because the FAU vs. EMT content is not yet decided at the aging stage, the current study emphasizes the importance of the overall sol composition (and hence the composition of the solution surrounding the sol particles and aggregates) in the crystal nucleation and growth kinetics favoring FAU over EMT. It excludes the possibility of a precursor nanoparticle transforming only through internal rearrangement to a zeolite nanocrystal.

4.3 Conclusions

In situ cryo-TEM and SAXS from representative optically clear and colloidally stable precursor sols (aged and crystallized at room temperature) reveal a common sequence of aggregation and nucleation events for compositions yielding FAU/EMT and predominantly FAU crystals. Starting with initial solutions containing monomeric and/or low molecular weight silica and alumina species and mixing them in ice bath decreases the kinetics of silicate and aluminate polymerization and results in small isolated precursor particles. A fraction of the amorphous nano-particles becomes colloidally unstable with time and aggregate. Amorphous aggregates form before the detection of crystals, which coincides with the state of sol that preserves the original trajectory towards nano-crystals after the pronounced reduction of water content by freeze-drying (chapter 3). Despite this *memory* effect, the sol at this stage is still agnostic towards FAU or EMT formation, the relative content of which is dominantly determined by the final water content. Nucleation takes place in such non-compact aggregates of precursor nano-particles, where each zeolite crystal is generated from one single nucleus resulting in single crystal domains spanning length scales corresponding to several precursor nano-

particles. Results confirmed precursor nanoparticle evolution, and emphasized the importance of pre-nucleation aggregation and the solution phase composition at both pre- and post-nucleation stages of aggregative crystal growth. To date, no technique has been able to elucidate directly how the nano-particles structurally evolve as a function of time though indirect indications of change were provided.[136,227]

Chapter 5

Concluding Remarks

The work presented in this dissertation aims at providing a better understanding of the growth of hierarchical Faujasite zeolite morphologies, the intergrowth of FAU/EMT zeolites, and the nucleation and growth of Faujasite nano-crystals from clear sols. With this understanding, it may be possible to utilize the intrinsic growth of Faujasite to create hierarchical morphologies or nano-crystals from inorganic routes thus eliminating expensive and unsafe organics that are employed in current synthesis procedures and have prevented the commercialization of these techniques.

The results presented in chapter 2, and the earlier work on MFI/MEL,[43] demonstrate that there is a direct link between the zeolite polytypes involved and the repetitive branching mechanism leading to the hierarchical structures (Fig. 5-1a). Being able to control the branching will set the stage of what is achievable in terms of characteristic diffusion length, mesopore size, and other characteristics. Similar investigations on other documented intergrowths (e.g. CHA/SOD[124] and ETS-10/ETS-4[125]) are desirable to establish possible branching mechanisms leading to hierarchical materials. Confirming the conclusions from this work, recently Inayat et al. reported similar house-of-card Faujasite from inorganic syntheses by adding simple inorganic salts, such as zinc nitrate and lithium carbonate.[76] For some of their materials, EMT was present in amounts significant enough to show up in XRD. However, the results presented in chapter 3 of this dissertation show that no additives are required for nucleating EMT, hence, the development of house-of-card assembly of Faujasite sheets from sodium aluminosilicate mixtures is likely possible. This material reduces the diffusion path length perpendicular to the sheets and also provides extra meso/macro-porosity between the sheets enhancing diffusion.

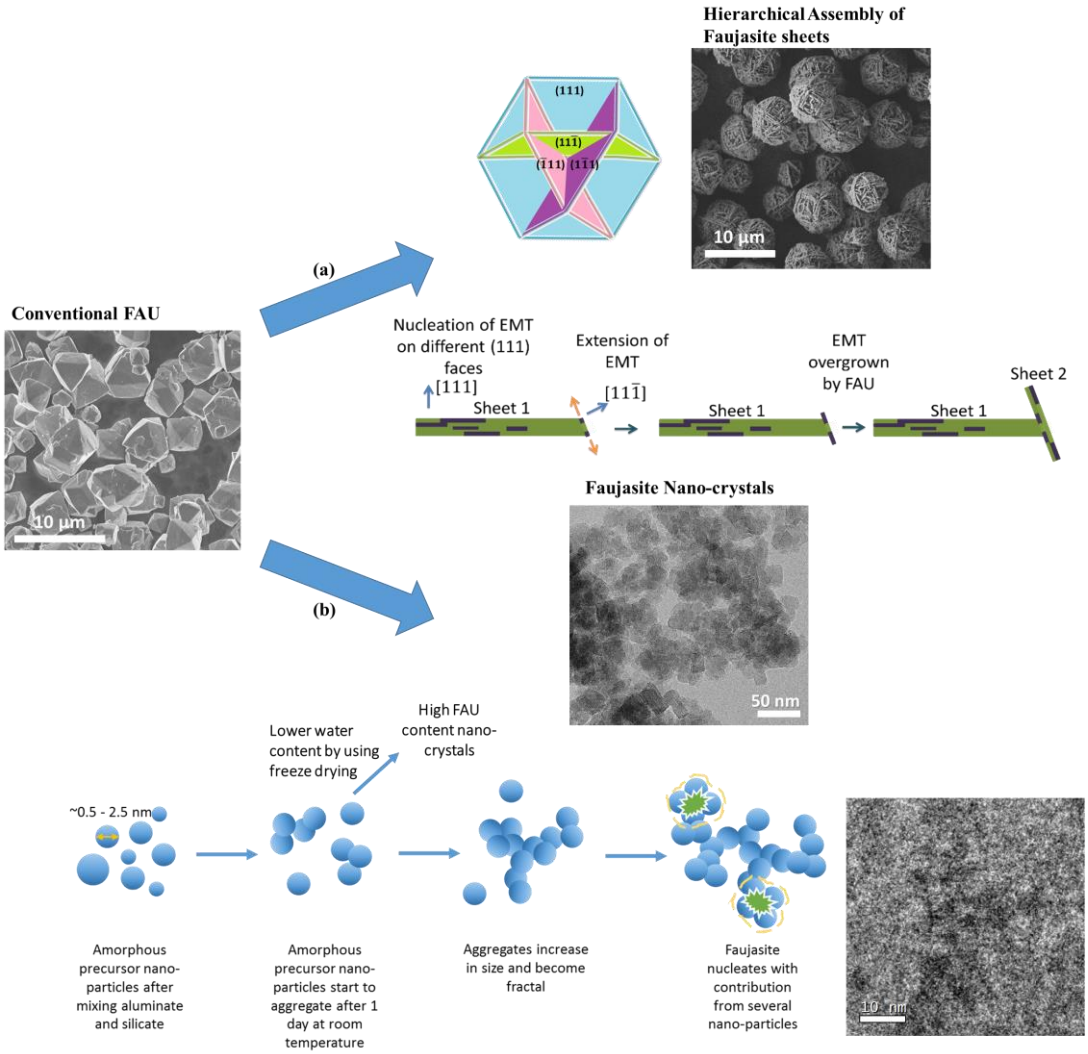

Figure 5-1: An overview of the conclusions from this dissertation showing (a) repetitive branching due to polytypism leading to house-of-card assembly of Faujasite sheets and (b) synthesis of Faujasite nano-crystals from inorganic aluminosilicate sols and the study of sol evolution in these mixtures.

In chapter 3, Faujasite nano-crystals with FAU contents between 0.6-0.8 were synthesized from inorganic aluminosilicate sols (Fig. 5-1b). The intergrowths of FAU and EMT in samples was studied by high resolution TEM imaging and XRD simulations using DIFFaX. It was found that reducing the crystal size prevents high FAU purity. This was overcome by combining pre- and post-nucleation trajectories by using freeze-drying after an initial aging step that allowed the extension of higher FAU purity (80 % FAU) to nano-crystals. The views presented here do not agree with those reported by Mintova's group on the better dispersion, and hence FAU purity, achieved by freeze drying.[138,169]

With a better understanding of zeolite crystallization, it may be possible to control particle size and shape, and the intergrowth of zeolites. Faujasite has not been typically utilized as a model system for studying zeolite nucleation and so there are very limited studies on this zeolite.[144,208] In chapter 4 Faujasite nucleation and growth was studied by *in situ* cryo-TEM and SAXS. Starting with initial solutions containing monomeric and/or low molecular weight silica and alumina species and mixing them in ice bath decreases the kinetics of silicate and aluminate polymerization and results in small isolated precursor particles. The results provide vital insights into the evolution of clear sols before Faujasite nucleation and show that they follow an aggregative mechanism similar to the one proposed for MFI by Davis et al.[136] and Kumar et al.[207] The aggregation of amorphous aluminosilicate nano-particles precedes Faujasite nucleation that takes place in the aggregates showing the importance of intra-aggregate rearrangements in zeolite nucleation. Zeolite crystals become more compact with aging time. It is at this stage, after the aggregation of precursor nano-particles, that freeze drying and lowering the water content of the synthesis mixture would result in higher FAU purity nano-crystals (chapter 3). Results confirmed precursor nanoparticle evolution, and emphasized the importance of the solution phase composition at both pre- and post-nucleation stages of aggregative crystal growth.

An important aspect of the hierarchical materials presented in this dissertation is their high aluminum content, giving them possible applications as basic catalysts,[98,99] ion exchangers,[148] or as selective adsorbents,[149] but they will not likely excel in applications requiring strong acidic catalysis because of the instability of the proton form of zeolite X at high temperatures. The large amount of work that has already been put into trying to synthesize high silica content Faujasite shows that this might not be possible.[101,150,153–155] However, future studies focusing on the correlation of performance with structural disorder and intergrowth in nano-crystals would be interesting. In conclusion, the results show that template free synthesis of hierarchical zeolites by utilizing their intrinsic

growth patterns appears to be a feasible route and that this should be the goal researchers seek for commercialization.

Bibliography

(1) Davis, M. E. *Nature* **2002**, *417* (6891), 813–821.
(2) Cejka, J.; van Bekkum, H.; Corma, A.; Schueth, F. *Introduction to Zeolite Molecular Sieves*; Elsevier, 2007.
(3) Pastore, H. O.; Coluccia, S.; Marchese, L. *Annu. Rev. Mater. Res.* **2005**, *35* (1), 351–395.
(4) Zhou, H.-C. J.; Kitagawa, S. *Chem. Soc. Rev.* **2014**, *43* (16), 5415–5418.
(5) First, E. L.; Gounaris, C. E.; Wei, J.; Floudas, C. A. *Phys. Chem. Chem. Phys.* **2011**, *13* (38), 17339–17358.
(6) Baerlocher, C.; McCusker, L. B.; Olson, D. H. *Atlas of Zeolite Framework Types*; Elsevier, 2007.
(7) Derouane, E. G.; Védrine, J. C.; Pinto, R. R.; Borges, P. M.; Costa, L.; Lemos, M. A. N. D. A.; Lemos, F.; Ribeiro, F. R. *Catal. Rev.* **2013**, *55* (4), 454–515.
(8) Caro, J.; Noack, M. *Microporous Mesoporous Mater.* **2008**, *115* (3), 215–233.
(9) Tsapatsis, M. *Science* **2011**, *334* (6057), 767–768.
(10) Snyder, M. A.; Tsapatsis, M. *Angew. Chem. Int. Ed. Engl.* **2007**, *46* (40), 7560–7573.
(11) García, E. J.; Pérez-Pellitero, J.; Pirngruber, G. D.; Jallut, C.; Palomino, M.; Rey, F.; Valencia, S. *Ind. Eng. Chem. Res.* **2014**, *53* (23), 9860–9874.
(12) Helfferich, F. G. *Ion Exchange*; Courier Corporation, 1962.
(13) Kesraoui-Ouki, S.; Cheeseman, C. R.; Perry, R. *J. Chem. Technol. Biotechnol.* **1994**, *59* (2), 121–126.
(14) Corma, A. *J. Catal.* **2003**, *216* (1-2), 298–312.
(15) Degnan, T. *J. Catal.* **2003**, *216* (1-2), 32–46.
(16) Chen, N. Y. *Shape Selective Catalysis in Industrial Applications, Second Edition,*; CRC Press, 1996.
(17) Thomas, S.; Bazin, P.; Lakiss, L.; de Waele, V.; Mintova, S. *Langmuir* **2011**, *27* (23), 14689–14695.
(18) Xu, X.; Wang, J.; Long, Y. *Sensors* **2006**, *6* (12), 1751–1764.
(19) Sahner, K.; Hagen, G.; Schonauer, D.; Reis, S.; Moos, R. *Solid State Ionics* **2008**, *179* (40), 2416–2423.
(20) Vohra, V.; Calzaferri, G.; Destri, S.; Pasini, M.; Porzio, W.; Botta, C. *ACS Nano* **2010**, *4* (3), 1409–1416.
(21) Thomassen, L. C. J.; Napierska, D.; Dinsdale, D.; Lievens, N.; Jammaer, J.; Lison, D.; Kirschhock, C. E. A.; Hoet, P. H.; Martens, J. A. *Nanotoxicology* **2012**, *6* (5), 472–485.
(22) Kihara, T.; Zhang, Y.; Hu, Y.; Mao, Q.; Tang, Y.; Miyake, J. *J. Biosci. Bioeng.* **2011**, *111* (6), 725–730.
(23) Petushkov, A.; Intra, J.; Graham, J. B.; Larsen, S. C.; Salem, A. K. *Chem. Res. Toxicol.* **2009**, *22* (7), 1359–1368.
(24) Yu, T.; Zhang, Y.; You, C.; Zhuang, J.; Wang, B.; Liu, B.; Kang, Y.; Tang, Y. *Chem. Eur. J.* **2006**, *12* (4), 1137–1143.
(25) Kang, Y.; Shan, W.; Wu, J.; Zhang, Y.; Wang, X.; Yang, W.; Tang, Y. *Chem. Mater.* **2006**, *18* (7), 1861–1866.
(26) Baerlocher, C.; McCusker, L. B. Database of Zeolite Structures http://www.iza-structure.org/databases/.
(27) Karger, J.; Freude, D. *Chem. Eng. Technol.* **2002**, *25* (8), 769–778.
(28) Kim, J.-H.; Kunieda, T.; Niwa, M. *J. Catal.* **1998**, *173* (2), 433–439.
(29) Tao, Y.; Kanoh, H.; Abrams, L.; Kaneko, K. *Chem. Rev.* **2006**, *106* (3), 896–910.
(30) Pérez-Ramírez, J.; Christensen, C. H.; Egeblad, K.; Christensen, C. H.; Groen, J. C. *Chem.*

Soc. Rev. **2008**, *37* (11), 2530–2542.
(31) Baur, R.; Krishna, R. *Catal. Today* **2005**, *105* (1), 173–179.
(32) Smit, B.; Maesen, T. L. M. *Nature* **2008**, *451* (7179), 671–678.
(33) Wei, Y.; Parmentier, T. E.; de Jong, K. P.; Zečević, J. *Chem. Soc. Rev.* **2015**, *44* (20), 7234–7261.
(34) Beck, J. S.; Vartuli, J. C.; Roth, W. J.; Leonowicz, M. E.; Kresge, C. T.; Schmitt, K. D.; Chu, C. T. W.; Olson, D. H.; Sheppard, E. W. *J. Am. Chem. Soc.* **1992**, *114* (27), 10834–10843.
(35) Kresge, C. T.; Leonowicz, M. E.; Roth, W. J.; Vartuli, J. C.; Beck, J. S. *Nature* **1992**, *359* (6397), 710–712.
(36) Zhao, D.; Feng, J.; Huo, Q.; Melosh, N.; Fredrickson, G. H.; Chmelka, B. F.; Stucky, G. D. *Science* **1998**, *279* (5350), 548–552.
(37) Jiang, J.; Yu, J.; Corma, A. *Angew. Chem. Int. Ed. Engl.* **2010**, *49* (18), 3120–3145.
(38) van Donk, S.; Janssen, A. H.; Bitter, J. H.; de Jong, K. P. *Catal. Rev.* **2003**, *45* (2), 297–319.
(39) Corma, A. *Chem. Rev.* **1997**, *97* (6), 2373–2420.
(40) Chal, R.; Gérardin, C.; Bulut, M.; van Donk, S. *ChemCatChem* **2011**, *3* (1), 67–81.
(41) Schmidt, W. *ChemCatChem* **2009**, *1* (1), 53–67.
(42) van Donk, S.; Broersma, A.; Gijzeman, O. L.; van Bokhoven, J. A.; Bitter, J. H.; de Jong, K. P. *J. Catal.* **2001**, *204* (2), 272–280.
(43) Zhang, X.; Liu, D.; Xu, D.; Asahina, S.; Cychosz, K. A.; Agrawal, K. V.; Al Wahedi, Y.; Bhan, A.; Al Hashimi, S.; Terasaki, O.; Thommes, M.; Tsapatsis, M. *Science* **2012**, *336* (6089), 1684–1687.
(44) Christensen, C. H.; Johannsen, K.; Schmidt, I.; Christensen, C. H. *J. Am. Chem. Soc.* **2003**, *125* (44), 13370–13371.
(45) Tromp, M.; van Bokhoven, J. A.; Garriga Oostenbrink, M. T.; Bitter, J. H.; de Jong, K. P.; Koningsberger, D. C. *J. Catal.* **2000**, *190* (2), 209–214.
(46) García-Martínez, J.; Johnson, M.; Valla, J.; Li, K.; Ying, J. Y. *Catal. Sci. Technol.* **2012**, *2* (5), 987–994.
(47) García-Martínez, J.; Li, K.; Krishnaiah, G. *Chem. Commun.* **2012**, *48* (97), 11841–11843.
(48) Srivastava, R.; Choi, M.; Ryoo, R. *Chem. Commun.* **2006**, No. 43, 4489–4491.
(49) Choi, M.; Na, K.; Kim, J.; Sakamoto, Y.; Terasaki, O.; Ryoo, R. *Nature* **2009**, *461* (7261), 246–249.
(50) Xu, D.; Swindlehurst, G. R.; Wu, H.; Olson, D. H.; Zhang, X.; Tsapatsis, M. *Adv. Funct. Mater.* **2014**, *24* (2), 201–208.
(51) Tosheva, L.; Valtchev, V. P. *Chem. Mater.* **2005**, *17* (10), 2494–2513.
(52) Verboekend, D.; Nuttens, N.; Locus, R.; Van Aelst, J.; Verolme, P.; Groen, J. C.; Pérez-Ramírez, J.; Sels, B. F. *Chem. Soc. Rev.* **2015**.
(53) Jacobsen, C. J. H.; Madsen, C.; Houzvicka, J.; Schmidt, I.; Carlsson, A. *J. Am. Chem. Soc.* **2000**, *122* (29), 7116–7117.
(54) Schmidt, I.; Krogh, A.; Wienberg, K.; Carlsson, A.; Brorson, M.; Jacobsen, C. J. H. *Chem. Commun.* **2000**, No. 21, 2157–2158.
(55) Schmidt, I.; Boisen, A.; Gustavsson, E.; Ståhl, K.; Pehrson, S.; Dahl, S.; Carlsson, A.; Jacobsen, C. J. H. *Chem. Mater.* **2001**, *13* (12), 4416–4418.
(56) Janssen, A. H.; Schmidt, I.; Jacobsen, C. J. H.; Koster, A. J.; de Jong, K. P. *Microporous Mesoporous Mater.* **2003**, *65* (1), 59–75.
(57) Tao, Y.; Kanoh, H.; Kaneko, K. *J. Phys. Chem. B* **2003**, *107* (40), 10974–10976.
(58) White, R. J.; Fischer, A.; Goebel, C.; Thomas, A. *J. Am. Chem. Soc.* **2014**, *136* (7), 2715–2718.

(59) Fan, W.; Snyder, M. A.; Kumar, S.; Lee, P.-S.; Yoo, W. C.; McCormick, A. V; Lee Penn, R.; Stein, A.; Tsapatsis, M. *Nat. Mater.* **2008**, *7* (12), 984–991.
(60) Chen, H.; Wydra, J.; Zhang, X.; Lee, P.-S.; Wang, Z.; Fan, W.; Tsapatsis, M. *J. Am. Chem. Soc.* **2011**, *133* (32), 12390–12393.
(61) Huang, L.; Guo, W.; Deng, P.; Xue, Z.; Li, Q. *J. Phys. Chem. B* **2000**, *104* (13), 2817–2823.
(62) Xiao, F.-S.; Wang, L.; Yin, C.; Lin, K.; Di, Y.; Li, J.; Xu, R.; Su, D. S.; Schlögl, R.; Yokoi, T.; Tatsumi, T. *Angew. Chem. Int. Ed. Engl.* **2006**, *45* (19), 3090–3093.
(63) Liu, B.; Duan, Q.; Li, C.; Zhu, Z.; Xi, H.; Qian, Y. *New J. Chem.* **2014**, *38* (9), 4380–4387.
(64) Na, K.; Jo, C.; Kim, J.; Cho, K.; Jung, J.; Seo, Y.; Messinger, R. J.; Chmelka, B. F.; Ryoo, R. *Science* **2011**, *333* (6040), 328–332.
(65) Xu, D.; Ma, Y.; Jing, Z.; Han, L.; Singh, B.; Feng, J.; Shen, X.; Cao, F.; Oleynikov, P.; Sun, H.; Terasaki, O.; Che, S. *Nat. Commun.* **2014**, *5*, 4262.
(66) Zhu, J.; Zhu, Y.; Zhu, L.; Rigutto, M.; van der Made, A.; Yang, C.; Pan, S.; Wang, L.; Zhu, L.; Jin, Y.; Sun, Q.; Wu, Q.; Meng, X.; Zhang, D.; Han, Y.; Li, J.; Chu, Y.; Zheng, A.; Qiu, S.; Zheng, X.; Xiao, F.-S. *J. Am. Chem. Soc.* **2014**, *136* (6), 2503–2510.
(67) Choi, M.; Cho, H. S.; Srivastava, R.; Venkatesan, C.; Choi, D.-H.; Ryoo, R. *Nat. Mater.* **2006**, *5* (9), 718–723.
(68) Cho, K.; Cho, H. S.; de Ménorval, L.-C.; Ryoo, R. *Chem. Mater.* **2009**, *21* (23), 5664–5673.
(69) Shanbhag, G. V.; Choi, M.; Kim, J.; Ryoo, R. *J. Catal.* **2009**, *264* (1), 88–92.
(70) Inayat, A.; Knoke, I.; Spiecker, E.; Schwieger, W. *Angew. Chem. Int. Ed. Engl.* **2012**, *51* (8), 1962–1965.
(71) Möller, K.; Yilmaz, B.; Jacubinas, R. M.; Müller, U.; Bein, T. *J. Am. Chem. Soc.* **2011**, *133* (14), 5284–5295.
(72) Chen , L.-H.; Li, X.-Y.; Tian, G.; Li, Y.; Rooke, J. C.; Zhu, G.-S.; Qiu, S.-L.; Yang , X.-Y.; Su , B.-L. *Angew. Chemie Int. Ed.* **2011**, *50* (47), 11156–11161.
(73) Möller, K.; Yilmaz, B.; Müller, U.; Bein, T. *Chemistry* **2012**, *18* (25), 7671–7674.
(74) Khaleel, M.; Wagner, A. J.; Mkhoyan, K. A.; Tsapatsis, M. *Angew. Chem. Int. Ed. Engl.* **2014**, *53* (36), 9456–9461.
(75) Chaikittisilp, W.; Suzuki, Y.; Mukti, R. R.; Suzuki, T.; Sugita, K.; Itabashi, K.; Shimojima, A.; Okubo, T. *Angew. Chemie Int. Ed.* **2013**, *52* (12), 3355–3359.
(76) Inayat, A.; Schneider, C.; Schwieger, W. *Chem. Commun.* **2015**, *51* (2), 279–281.
(77) Cartlidge, S.; Nissen, H.-U.; Wessicken, R. *Zeolites* **1989**, *9* (4), 346–349.
(78) Scherzer, J. *J. Catal.* **1978**, *54* (2), 285–288.
(79) Lynch, J.; Raatz, F.; Dufresne, P. *Zeolites* **1987**, *7* (4), 333–340.
(80) de Jong, K. P.; Zečević, J.; Friedrich, H.; de Jongh, P. E.; Bulut, M.; van Donk, S.; Kenmogne, R.; Finiels, A.; Hulea, V.; Fajula, F. *Angew. Chem. Int. Ed. Engl.* **2010**, *49* (52), 10074–10078.
(81) Verboekend, D.; Vilé, G.; Pérez-Ramírez, J. *Adv. Funct. Mater.* **2012**, *22* (5), 916–928.
(82) Verboekend, D.; Keller, T. C.; Mitchell, S.; Pérez-Ramírez, J. *Adv. Funct. Mater.* **2013**, *23* (15), 1923–1934.
(83) Groen, J. C.; Moulijn, J. A.; Pérez-Ramírez, J. *J. Mater. Chem.* **2006**, *16* (22), 2121–2131.
(84) van Laak, A. N. C.; Sagala, S. L.; Zečević, J.; Friedrich, H.; de Jongh, P. E.; de Jong, K. P. *J. Catal.* **2010**, *276* (1), 170–180.
(85) Verboekend, D.; Vilé, G.; Pérez-Ramírez, J. *Cryst. Growth Des.* **2012**, *12* (6), 3123–3132.
(86) Verboekend, D.; Pérez-Ramírez, J. *Chemistry* **2011**, *17* (4), 1137–1147.
(87) Pérez-Ramírez, J.; Abelló, S.; Bonilla, A.; Groen, J. C. *Adv. Funct. Mater.* **2009**, *19* (1),

164–172.
(88) Kortunov, P.; Vasenkov, S.; Kärger, J.; Valiullin, R.; Gottschalk, P.; Elía, M. F.; Perez, M.; Stöcker, M.; Drescher, B.; McElhiney, G.; Berger, C.; Gläser, R.; Weitkamp, J. *J. Am. Chem. Soc.* **2005**, *127* (37), 13055–13059.
(89) Janssen, A. H.; Koster, A. J.; de Jong, K. P. *J. Phys. Chem. B* **2002**, *106* (46), 11905–11909.
(90) Ivanova, I. I.; Kasyanov, I. A.; Maerle, A. A.; Zaikovskii, V. I. *Microporous Mesoporous Mater.* **2014**, *189*, 163–172.
(91) Thomas, J. M.; Audier, M.; Klinowski, J. *J. Chem. Soc. Chem. Commun.* **1981**, No. 23, 1221–1222.
(92) Gao, D.; Duan, A.; Zhang, X.; Zhao, Z.; E, H.; Qin, Y.; Xu, C. *Chem. Eng. J.* **2015**, *270*, 176–186.
(93) Hattori, H. *Chem. Rev.* **1995**, *95* (3), 537–558.
(94) Weitkamp, J.; Hunger, M.; Rymsa, U. *Microporous Mesoporous Mater.* **2001**, *48* (1-3), 255–270.
(95) Martens, L. R. M.; Grobet, P. J.; Jacobs, P. A. *Nature* **1985**, *315* (6020), 568–570.
(96) Hathaway, P.; Davis, M. E. *J. Catal.* **1989**, *116* (1), 263–278.
(97) Ernst, S.; Hartmann, M.; Sauerbeck, S.; Bongers, T. *Appl. Catal. A Gen.* **2000**, *200* (1-2), 117–123.
(98) Davis, R. *J. Catal.* **2003**, *216* (1-2), 396–405.
(99) Luz Martínez, S.; Romero, R.; López, J. C.; Romero, A.; Sánchez Mendieta, V.; Natividad, R. *Ind. Eng. Chem. Res.* **2011**, *50* (5), 2665–2670.
(100) Treacy, M. M. J.; Vaughan, D. E. W.; Strohmaier, K. G.; Newsam, J. M. *Proc. R. Soc. A* **1996**, *452* (1947), 813–840.
(101) Delprato, F.; Delmotte, L.; Guth, J. L.; Huve, L. *Zeolites* **1990**, *10* (6), 546–552.
(102) Vaughan, D.; Treacy, M.; Newsam, J.; Strohmaier, K.; Mortier, W. In *ACS Symposium Series Vol 398: In Zeolite synthesis*; Occelli, M., Robson, H., Eds.; American Chemical Society: Washington, 1989; pp 544–559.
(103) Terasaki, O.; Ohsuna, T.; Alfredsson, V.; Bovin, J. O.; Watanabe, D.; Carr, S. W.; Anderson, M. W. *Chem. Mater.* **1993**, *5* (4), 452–458.
(104) Anderson, M. W.; Agger, J. R.; Thornton, J. T.; Forsyth, N. *Angew. Chem. Int. Ed. Engl.* **1996**, *35* (11), 1210–1213.
(105) González, G.; González, C. S.; Stracke, W.; Reichelt, R.; García, L. *Microporous Mesoporous Mater.* **2007**, *101* (1-2), 30–42.
(106) Davis, M. In *Synthesis of Microporous Materials, Molecular Sieves Vol 1*; Occelli, M., Robson, H., Eds.; Springer, 1992; pp 60–69.
(107) Ravikovitch, P. I.; Neimark, A. V. *Colloids Surfaces A Physicochem. Eng. Asp.* **2001**, *187-188*, 11–21.
(108) Nagahara, L. A.; Hashimoto, K.; Fujishima, A.; Snowden-Ifft, D.; Price, P. B. *J. Vac. Sci. Technol. B* **1994**, *12* (3), 1694–1697.
(109) Cowley, J. M.; Moodie, A. F. *Acta Crystallogr.* **1957**, *10* (10), 609–619.
(110) Lynch, D. F.; O'Keefe, M. A. *Acta Crystallogr. Sect. A* **1972**, *28* (6), 536–548.
(111) Kirkland, E. J. *Advanced Computing in Electron Microscopy*; Springer US: Boston, MA, 2010.
(112) Makinson, J. D.; Lee, J. S.; Magner, S. H.; Angelis, R. J. De; Weins, W. N.; Hieronymus, A. S. *Adv. X-ray Anal.* **1998**, *42*, 407–411.
(113) Berliner, R.; Werner, S. A. *Phys. Rev. B* **1986**, *34* (6), 3586–3603.
(114) Welberry, T. R. *Reports Prog. Phys.* **1985**, *48* (11), 1543–1594.
(115) Melchior, M. T.; Vaughan, D. E. W.; Pictroski, C. F. *J. Phys. Chem.* **1995**, *99* (16), 6128–

6144.
(116) Serrano, D. P.; Aguado, J.; Escola, J. M.; Rodriguez, J. M.; Peral, A. *J. Mater. Chem.* **2008**, *18* (35), 4210–4218.
(117) Su, B. L.; Roussel, M.; Vause, K.; Yang, X. Y.; Gilles, F.; Shi, L.; Leonova, E.; Edén, M.; Zou, X. *Microporous Mesoporous Mater.* **2007**, *105* (1-2), 49–57.
(118) Azaïs, T.; Hartmeyer, G.; Quignard, S.; Laurent, G.; Tourné-Péteilh, C.; Devoisselle, J.-M.; Babonneau, F. *Pure Appl. Chem.* **2009**, *81* (8), 1345–1355.
(119) Ray, G. J.; Meyers, B. L.; Marshall, C. L. *Zeolites* **1987**, *7* (4), 307–310.
(120) Millward, G.; Thomas, J.; Ramdas, S.; Barlow, M. Olson, D., Bisio, A., Eds.; Butterworths: Guildford, Surrey, 1984; pp 793–802.
(121) Hartman, P.; Perdok, W. G. *Acta Crystallogr.* **1955**, *8* (9), 525–529.
(122) Libbrecht, K. G. *Reports Prog. Phys.* **2005**, *68* (4), 855–895.
(123) Libbrecht, K. *Ken Libbrecht's Field Guide to Snowflakes*; Voyageur Press: Minnesota, 2006.
(124) Wakihara, T.; Yamakita, S.; Iezumi, K.; Okubo, T. *J. Am. Chem. Soc.* **2003**, *125* (41), 12388–12389.
(125) Jeong, H.-K.; Krohn, J.; Sujaoti, K.; Tsapatsis, M. *J. Am. Chem. Soc.* **2002**, *124* (44), 12966–12968.
(126) Mintova, S.; Gilson, J.-P.; Valtchev, V. *Nanoscale* **2013**, *5* (15), 6693–6703.
(127) Mitchell, S.; Pinar, A. B.; Kenvin, J.; Crivelli, P.; Kärger, J.; Pérez-Ramírez, J. *Nat. Commun.* **2015**, *6*, 8633.
(128) McLeary, E. E.; Jansen, J. C.; Kapteijn, F. *Microporous Mesoporous Mater.* **2006**, *90* (1-3), 198–220.
(129) Vandezande, P.; Gevers, L. E. M.; Vermant, J.; Martens, J. A.; Jacobs, P. A.; Vankelecom, I. F. J. *Chem. Mater.* **2008**, *20* (10), 3457–3465.
(130) Severance, M.; Wang, B.; Ramasubramanian, K.; Zhao, L.; Ho, W. S. W.; Dutta, P. K. *Langmuir* **2014**, *30* (23), 6929–6937.
(131) Lovallo, M. C.; Tsapatsis, M. *AIChE J.* **1996**, *42* (11), 3020–3029.
(132) Lee, P.-S.; Zhang, X.; Stoeger, J. A.; Malek, A.; Fan, W.; Kumar, S.; Yoo, W. C.; Al Hashimi, S.; Penn, R. L.; Stein, A.; Tsapatsis, M. *J. Am. Chem. Soc.* **2011**, *133* (3), 493–502.
(133) Rangnekar, N.; Mittal, N.; Elyassi, B.; Caro, J.; Tsapatsis, M. *Chem. Soc. Rev.* **2015**, *44* (20), 7128–7154.
(134) Lew, C. M.; Cai, R.; Yan, Y. *Acc. Chem. Res.* **2010**, *43* (2), 210–219.
(135) Li, Z.; Johnson, M. C.; Sun, M.; Ryan, E. T.; Earl, D. J.; Maichen, W.; Martin, J. I.; Li, S.; Lew, C. M.; Wang, J.; Deem, M. W.; Davis, M. E.; Yan, Y. *Angew. Chem. Int. Ed. Engl.* **2006**, *45* (38), 6329–6332.
(136) Davis, T. M.; Drews, T. O.; Ramanan, H.; He, C.; Dong, J.; Schnablegger, H.; Katsoulakis, M. A.; Kokkoli, E.; McCormick, A. V; Penn, R. L.; Tsapatsis, M. *Nat. Mater.* **2006**, *5* (5), 400–408.
(137) Wang, H.; Wang, Z.; Yan, Y. *Chem. Commun.* **2000**, No. 23, 2333–2334.
(138) Awala, H.; Gilson, J.-P.; Retoux, R.; Boullay, P.; Goupil, J.-M.; Valtchev, V.; Mintova, S. *Nat. Mater.* **2015**, *14* (4), 447–451.
(139) Serrano, D. P.; Aguado, J.; Escola, J. M.; Rodríguez, J. M.; Peral, Á. *Chem. Mater.* **2006**, *18* (10), 2462–2464.
(140) Aguado, J.; Serrano, D. P.; Escola, J. M.; Peral, A. *J. Anal. Appl. Pyrolysis* **2009**, *85* (1-2), 352–358.
(141) Oleksiak, M. D.; Rimer, J. D. *Rev. Chem. Eng.* **2014**, *30* (1), 1–49.
(142) Rajagopalan, K.; Peters, A. W.; Edwards, G. C. *Appl. Catal.* **1986**, *23* (1), 69–80.

(143) Chaves, T. F.; Pastore, H. O.; Cardoso, D. *Microporous Mesoporous Mater.* **2012**, *161*, 67–75.
(144) Valtchev, V. P.; Bozhilov, K. N. *J. Phys. Chem. B* **2004**, *108* (40), 15587–15598.
(145) Zhan, B.-Z.; White, M. A.; Lumsden, M.; Mueller-Neuhaus, J.; Robertson, K. N.; Cameron, T. S.; Gharghouri, M. *Chem. Mater.* **2002**, *14* (9), 3636–3642.
(146) McDaniel, C.; Maher, P.; Pilato, J. US3808326 A: Preparation of zeolites, April 30, 1974.
(147) Mastropietro, T. F.; Drioli, E.; Poerio, T. *RSC Adv.* **2014**, *4* (42), 21951–21957.
(148) Sherry, H. S. *J. Phys. Chem.* **1966**, *70* (4), 1158–1168.
(149) Walton, K. S.; Abney, M. B.; Douglas LeVan, M. *Microporous Mesoporous Mater.* **2006**, *91* (1-3), 78–84.
(150) Breck, D. W. US3130007A: Crystalline zeolite Y, 1964.
(151) Rabo, J. A.; Poutsma, M. L. Flanigen, E. M., Sand, L. B., Eds.; Advances in Chemistry; American Chemical Society: Washington, D. C., 1971; Vol. 102, pp 284–314.
(152) Wright, A.; Rupert, J. P.; Granquist, W. T. *Am. Mineral.* **1968**, *53*, 1293–1303.
(153) Vaughan, D.; Barrett, M. High silica faujasite polymorph - CSZ-3 and method of synthesizing. US 4333859 A, 1982.
(154) Vaughan, D. Process for preparing a high silica faujasite aluminosilicate, ECR-4. US 4714601A, 1987.
(155) Elliott Jr, C.; Mcdaniel, C. Preparation of high-silica faujasite. US 3639099 A, 1972.
(156) Eberly Jr, P.; Laurent, S.; Robson, H. High silica crystalline zeolites and process for their preparation. US 3506400 A, 1970.
(157) Beyer, H. K.; Belenykaja, I. M.; Hange, F.; Tielen, M.; Grobet, P. J.; Jacobs, P. A. *J. Chem. Soc. Faraday Trans. 1* **1985**, *81* (11), 2889–2901.
(158) Kerr, G. T.; Chester, A. W. Ultra high silicon-content zeolites and preparation thereof. US 4093560 A, 1978.
(159) Ng, E.-P.; Chateigner, D.; Bein, T.; Valtchev, V.; Mintova, S. *Science* **2012**, *335* (6064), 70–73.
(160) Treacy, M. M. J.; Newsam, J. M.; Deem, M. W. *Proc. R. Soc. A* **1991**, *433* (1889), 499–520.
(161) Milton, R. M. US2882244A: Molecular sieve adsorbents, 1959.
(162) Zhang, X. Directed synthesis and characterization of zeolite nanoparticles, University of Minnesota, 2013.
(163) Treacy, M. M. J.; Newsam, J. M.; Beyerlein, R. A.; Leonowicz, M. E.; Vaughan, D. E. W. *J. Chem. Soc. Chem. Commun.* **1986**, No. 15, 1211–1213.
(164) Villaescusa, L. A.; Zhou, W.; Morris, R. E.; Barrett, P. A. *J. Mater. Chem.* **2004**, *14* (13), 1982–1987.
(165) Taborda, F.; Willhammar, T.; Wang, Z.; Montes, C.; Zou, X. *Microporous Mesoporous Mater.* **2011**, *143* (1), 196–205.
(166) Maldonado, M.; Oleksiak, M. D.; Chinta, S.; Rimer, J. D. *J. Am. Chem. Soc.* **2013**, *135* (7), 2641–2652.
(167) Tompsett, G. A.; Conner, W. C.; Yngvesson, K. S. *Chemphyschem* **2006**, *7* (2), 296–319.
(168) Antonić Jelić, T.; Bronić, J.; Hadžija, M.; Subotić, B.; Marić, I. *Microporous Mesoporous Mater.* **2007**, *105* (1-2), 65–74.
(169) Mintova, S.; Awala, H.; Gilson, J.-P.; Valtchev, V. Method for the preparation of a synthetic faujasite material comprising monodisperse nanoparticles composed of single nanocrystals. WO2015101800 A1, 2015.
(170) Mintova, S. Personal Communication.
(171) Davis, M. E.; Lobo, R. F. *Chem. Mater.* **1992**, *4* (4), 756–768.
(172) Persson, A. E.; Schoeman, B. J.; Sterte, J.; Otterstedt, J.-E. *Zeolites* **1994**, *14* (7), 557–567.

(173) Schoeman, B. J. *Microporous Mesoporous Mater.* **1998**, *22* (1-3), 9–22.
(174) Dougherty, J.; Iton, L. E.; White, J. W. *Zeolites* **1995**, *15* (7), 640–649.
(175) Mintova, S.; Olson, N.; Valtchev, V.; Bein, T. *Science* **1999**, *283* (5404), 958–960.
(176) Tsapatsis, M.; Lovallo, M.; Davis, M. E. *Microporous Mater.* **1996**, *5* (6), 381–388.
(177) Cundy, C. S.; Lowe, B. M.; Sinclair, D. M. *J. Cryst. Growth* **1990**, *100* (1-2), 189–202.
(178) Cundy, C. S.; Henty, M. S.; Plaisted, R. J. *Zeolites* **1995**, *15* (4), 342–352.
(179) Burkett, S. L.; Davis, M. E. *J. Phys. Chem.* **1994**, *98* (17), 4647–4653.
(180) Corkery, R. W.; Ninham, B. W. *Zeolites* **1997**, *18* (5-6), 379–386.
(181) Dokter, W. H.; van Garderen, H. F.; Beelen, T. P. M.; van Santen, R. A.; Bras, W. *Angew. Chem. Int. Ed. Engl.* **1995**, *34* (1), 73–75.
(182) Fedeyko, J. M.; Egolf-Fox, H.; Fickel, D. W.; Vlachos, D. G.; Lobo, R. F. *Langmuir* **2007**, *23* (8), 4532–4540.
(183) Cheng, C.-H.; Shantz, D. F. *J. Phys. Chem. B* **2005**, *109* (41), 19116–19125.
(184) Cheng, C.-H.; Shantz, D. F. *J. Phys. Chem. B* **2005**, *109* (29), 13912–13920.
(185) Fedeyko, J. M.; Rimer, J. D.; Lobo, R. F.; Vlachos, D. G. *J. Phys. Chem. B* **2004**, *108* (33), 12271–12275.
(186) de Moor, P.-P. E. A.; Beelen, T. P. M.; van Santen, R. A.; Beck, L. W.; Davis, M. E. *J. Phys. Chem. B* **2000**, *104* (32), 7600–7611.
(187) Fedeyko, J. M.; Vlachos, D. G.; Lobo, R. F. *Langmuir* **2005**, *21* (11), 5197–5206.
(188) Schoeman, B. J.; Regev, O. *Zeolites* **1996**, *17* (5-6), 447–456.
(189) Schoeman, B. J. *Microporous Mater.* **1997**, *9* (5-6), 267–271.
(190) Mintova, S.; Olson, N.; Senker, J.; Bein, T. *Angew. Chem. Int. Ed.* **2002**, *41* (14), 2558–2561.
(191) Rimer, J. D.; Lobo, R. F.; Vlachos, D. G. *Langmuir* **2005**, *21* (19), 8960–8971.
(192) Kinrade, S. D.; Knight, C. T. G.; Pole, D. L.; Syvitski, R. T. *Inorg. Chem.* **1998**, *37* (17), 4272–4277.
(193) Šefčík, J.; McCormick, A. V. *AIChE J.* **1997**, *43* (S11), 2773–2784.
(194) Kinrade, S. D.; Swaddle, T. W. *Inorg. Chem.* **1989**, *28* (10), 1952–1954.
(195) Mortlock, R. F.; Bell, A. T.; Radke, C. J. *J. Phys. Chem.* **1991**, *95* (20), 7847–7851.
(196) Mortlock, R. F.; Bell, A. T.; Chakraborty, A. K.; Radke, C. J. *J. Phys. Chem.* **1991**, *95* (11), 4501–4506.
(197) McCormick, A. V.; Bell, A. T.; Radke, C. J. *J. Phys. Chem.* **1989**, *93* (5), 1741–1744.
(198) Yokoyama, T.; Kinoshita, S.; Wakita, H.; Tarutani, T. *Bull. Chem. Soc. Jpn.* **1988**, *61* (3), 1002–1004.
(199) Ramanan, H.; Kokkoli, E.; Tsapatsis, M. *Angew. Chem. Int. Ed. Engl.* **2004**, *43* (35), 4558–4561.
(200) Kragten, D. D.; Fedeyko, J. M.; Sawant, K. R.; Rimer, J. D.; Vlachos, D. G.; Lobo, R. F.; Tsapatsis, M. *J. Phys. Chem. B* **2003**, *107* (37), 10006–10016.
(201) Knight, C. T. G.; Kinrade, S. D. *J. Phys. Chem. B* **2002**, *106* (12), 3329–3332.
(202) Kirschhock, C.; Buschmann, V.; Kremer, S.; Ravishankar, R.; Houssin, C.; Mojet, B.; van Santen, R.; Grobet, P.; Jacobs, P.; Martens, J. *Angew. Chem. Int. Ed.* **2001**, *40* (14), 2637–2640.
(203) Liang, D.; Follens, L. R. A.; Aerts, A.; Martens, J. A.; Van Tendeloo, G.; Kirschhock, C. E. A. *J. Phys. Chem. C* **2007**, *111* (39), 14283–14285.
(204) de Moor, P.-P. E. A.; Beelen, T. P. M.; Komanschek, B. U.; Diat, O.; van Santen, R. A. *J. Phys. Chem. B* **1997**, *101* (51), 11077–11086.
(205) de Moor, P.-P. E. A.; Beelen, T. P. M.; Komanschek, B. U.; van Santen, R. A. *Microporous Mesoporous Mater.* **1998**, *21* (4-6), 263–269.
(206) Nikolakis, V.; Kokkoli, E.; Tirrell, M.; Tsapatsis, M.; Vlachos, D. G. *Chem. Mater.* **2000**,

12 (3), 845–853.
(207) Kumar, S.; Wang, Z.; Penn, R. L.; Tsapatsis, M. *J. Am. Chem. Soc.* **2008**, *130* (51), 17284–17286.
(208) Mintova, S.; Olson, N.; Bein, T. *Angew. Chem. Int. Ed.* **1999**, *38* (21), 3201–3204.
(209) Burns, J. L.; Cohen, Y.; Talmon, Y. *J. Phys. Chem.* **1990**, *94* (13), 5308–5312.
(210) Talmon, Y. *Colloids and Surfaces* **1986**, *19* (2-3), 237–248.
(211) Talmon, Y. *Berichte der Bunsengesellschaft für Phys. Chemie* **1996**, *100* (3), 364–372.
(212) Costello, M. J. *Ultrastruct. Pathol.* **2005**, *30* (5), 361–371.
(213) Dubochet, J.; Adrian, M.; Chang, J.-J.; Homo, J.-C.; Lepault, J.; McDowall, A. W.; Schultz, P. *Q. Rev. Biophys.* **1988**, *21* (2), 129–228.
(214) Danino, D.; Moon, K.-H.; Hinshaw, J. E. *J. Struct. Biol.* **2004**, *147* (3), 259–267.
(215) Regev, O.; Cohen, Y.; Kehat, E.; Talmon, Y. *Zeolites* **1994**, *14* (5), 314–319.
(216) Klint, D.; Karlsson, G.; Bovin, J. *Angew. Chem. Int. Ed. Engl.* **1999**, *38* (17), 2560–2562.
(217) Regev, O. *Langmuir* **1996**, *12* (20), 4940–4944.
(218) Cui, H.; Hodgdon, T. K.; Kaler, E. W.; Abezgauz, L.; Danino, D.; Lubovsky, M.; Talmon, Y.; Pochan, D. J. *Soft Matter* **2007**, *3* (8), 945–955.
(219) Qin, L. C.; Hobbs, L. W. In *Materials Research Society Symposium Proceedings*; Cambridge University Press: Boston, MA, 1994; Vol. 373, p 329.
(220) Falls, A. H.; Wellinghoff, S. T.; Talmon, Y.; Thomas, E. L. *J. Mater. Sci.* **1983**, *18* (9), 2752–2764.
(221) *Modern Characterization Methods of Surfactant Systems*; Binks, B., Furlong, D., Eds.; CRC Press, 1999.
(222) Pan, M. *Micron* **1996**, *27* (3-4), 219–238.
(223) Thomas, J. M.; Terasaki, O.; Gai, P. L.; Zhou, W.; Gonzalez-Calbet, J. *Acc. Chem. Res.* **2001**, *34* (7), 583–594.
(224) Treacy, M. M. J.; Newsam, J. M. *Ultramicroscopy* **1987**, *23* (3-4), 411–419.
(225) Glatter, O.; Kratky, O. *Small Angle X-ray Scattering*; Academic Press, 1982.
(226) Drews, T. O.; Katsoulakis, M. A.; Tsapatsis, M. *J. Phys. Chem. B* **2005**, *109* (50), 23879–23887.
(227) Rimer, J. D.; Trofymluk, O.; Navrotsky, A.; Lobo, R. F.; Vlachos, D. G. *Chem. Mater.* **2007**, *19* (17), 4189–4197.